

Compositional study of trans-Neptunian objects at $\lambda > 2.2 \mu\text{m}$ *

E. FERNÁNDEZ-VALENZUELA,¹ N. PINILLA-ALONSO,¹ J. STANSBERRY,² J. P. EMERY,³ W. PERKINS,⁴ C. VAN LAERHOVEN,⁵
B. J. GLADMAN,⁵ W. FRASER,⁶ D. CRUIKSHANK,⁷ E. LELLOUCH,⁸ T. G. MÜLLER,⁹ W. M. GRUNDY,¹⁰ D. TRILLING,³
Y. FERNANDEZ,¹¹ AND C. DALLE-ORE¹²

¹Florida Space Institute, University of Central Florida, 12354 Research Parkway, Partnership 1, Orlando, FL, USA

²Space Telescope Science Institute, Baltimore, MD, USA

³Department of Astronomy and Planetary Sciences, Northern Arizona University, Flagstaff, AZ, USA

⁴Department of Earth and Planetary Sciences, University of Tennessee, Knoxville, TN, USA

⁵University of British Columbia, Department of Physics and Astronomy, 6224 Agricultural Road, Vancouver, BC, Canada

⁶NRC Herzberg Astrophysics, BC, Canada

⁷NASA Ames Research Center, Moffett Field, CA, USA

⁸LESIA, Observatoire de Paris, Meudon, France

⁹Max-Planck-Institut für Extraterrestrische Physik, Center for Astrochemical Studies, Garching, Germany

¹⁰Lowell Observatory, Flagstaff, Arizona, USA

¹¹Department of Physics, University of Central Florida, Orlando, Florida, USA

¹²SETI Institute, Mountain View, CA, USA ; NASA Ames Research Center, Moffett Field, CA, USA

Submitted to PSJ

ABSTRACT

Using data from the Infrared Array Camera on the Spitzer Space Telescope, we present photometric observations of a sample of 100 trans-Neptunian objects (TNOs) beyond $2.2 \mu\text{m}$. These observations, collected with two broad-band filters centered at 3.6 and $4.5 \mu\text{m}$, were done in order to study the surface composition of TNOs, which are too faint to obtain spectroscopic measurements. With this aim, we have developed a method for the identification of different materials that are found on the surfaces of TNOs. In our sample, we detected objects with colors that are consistent with the presence of small amounts of water and were able to distinguish between surfaces that are predominately composed of complex organics and amorphous silicates. We found that 86% of our sample have characteristics that are consistent with a certain amount of water ice, and the most common composition (73% of the objects) is a mixture of water ice, amorphous silicates, and complex organics. 23% of our sample may include other ices such as carbon monoxide, carbon dioxide, methane or methanol. Additionally, only small objects seem to have surfaces dominated by silicates. This method is a unique tool for the identification of complex organics and to obtain the surface composition of extremely faint objects. Also, this method will be beneficial when using the *James Webb Space Telescope* for differentiating groups within the trans-Neptunian population.

Keywords: Trans-Neptunian objects (TNOs) – TNOs: composition – TNOs: surface – Spectrophotometric techniques – Origin: solar system

1. INTRODUCTION

Trans-Neptunian objects (TNOs) are solar system objects whose heliocentric orbits have semi-major axes

a greater than that of Neptune and less than where the Oort clouds begin, i.e., $30.07 < a < 2000 \text{ au}$ (Gladman et al. 2008). Centaurs, with semi-major axes a between those of Jupiter and Neptune, are a significant population of objects in the region between the giant planets; from a compositional point of view they are of great interest because these nearby objects are easier to study and believed to be derived from TNOs

Corresponding author: E. Fernández-Valenzuela
estela@ucf.edu

* Accepted for publication on October 13, 2020.

via perturbations by Neptune and the other giant planets (Fernandez 1980; Levison & Duncan 1997). Therefore, both populations are studied together, understanding that there is a greater chance of recent modification of Centaur surfaces as they approach the Sun from the trans-neptunian region.

Due to their large heliocentric distances, all TNOs have surface temperatures that are low enough to retain water ice. Non-Centaur TNOs can also harbor highly volatile ices such as CO_2 , CH_4 , CO and N_2 in stable form, although the last three are likely only present on the TNO dwarf planets, which have enough mass to trap them gravitationally (Schaller & Brown 2007a; Pinilla-Alonso et al. 2020; Young et al. 2020). In addition to these molecular ices, TNO surfaces are thought to be composed of refractory macromolecular complexes (termed tholins), derived via photolysis and radiolysis of ices (Khare et al. 1993; Materese et al. 2014, 2015), and silicates incorporated as grains during accretion from the solar nebula. The slightly- to extremely-red colors of some TNOs likely reflect the presence of these organic “tholins”, although some silicates can also be slightly reddish in the visible spectral region.

Determining the relationships between the physical properties of TNOs to their dynamical classifications and orbital histories may help us understand the composition and thermal state of the solar nebula as a function of heliocentric radius (e.g., Fernández 2020). The cold-classical objects in the main belt (see section 3.1) are the only ones thought to still reside in their primordial orbits (e.g., Brown 2001; Van Laerhoven et al. 2019); TNOs in all other classes were likely perturbed greatly from their original orbits by interactions with the migrating giant planets (e.g., Gladman et al. 2008; Petit et al. 2011; Morbidelli & Nesvorný 2020). However, establishing the composition-dynamics relationship is difficult because TNOs are so faint (typical $m_V \gtrsim 20$). Relatively few have near-IR colors, which could be diagnostic of composition, let alone near-IR spectra. The alteration of surface composition may also play a role in camouflaging links between dynamical class and composition (Gil-Hutton 2002). This is more likely on Centaurs, which experience much higher temperatures and fluxes of solar UV and charged particles than the more distant TNOs.

Multi-filter photometry has been used to study the composition of relatively large samples of TNOs, and has revealed some correlation between optical colors and size (e.g., Fraser & Brown 2012; Peixinho et al. 2015), and between color and orbital inclination in the classical population (e.g., Trujillo & Brown 2002; Doressoundiram et al. 2002; Marsset et al. 2020). Ther-

mal data also revealed that the cold-classical objects also generally have higher albedos than the hot-classical objects (Brucker et al. 2009; Lacerda et al. 2014; Vilenius et al. 2014). Near-IR colors potentially offer better discrimination of composition, but only $\sim 25\%$ of all ground-based data for TNOs are at these wavelengths (i.e., from $\lambda \sim 1$ to $\sim 2.5 \mu\text{m}$; e.g., Hainaut et al. 2012). Fraser & Brown (2012) and Fraser et al. (2015) reported on the visible and NIR observations of 100 small TNOs and Centaurs using the *Hubble* WFC3, finding two clusters in visible vs. near-IR color, and evidence of ubiquitous H_2O ice. To date, spectra of various quality have been collected for only about 75 TNOs and Centaurs total (e.g., Barkume et al. 2008; Brown 2008; Barucci et al. 2011; Barucci & Merlin 2020, and references therein). Based on those data, it appears that H_2O is the most common ice detected on TNOs’ surfaces.

These past studies have achieved limited success in part because they are limited by the sensitivity of ground-based facilities, and in part because only the relatively weak near-IR bands of the components of interest could be studied. The ices and complex organics (sometimes we also refer to the latest as only organics) that we expect to find on TNOs and Centaurs have their fundamental absorption bands beyond $2.2 \mu\text{m}$, necessitating space-based observations due to the atmospheric interference and low brightness presented by this populations. Here we summarize a collection of 3.6 and $4.5 \mu\text{m}$ observations of TNOs made with the Infrared Array Camera, IRAC (Fazio et al. 2004), on the *Spitzer Space Observatory* (hereafter, *Spitzer*). These data are consistent with absorption bands due to H_2O , organic tholins, and volatile ices, and the presence of silicates. They also reveal the range of geometric albedos of TNOs at $3 - 5 \mu\text{m}$, which will be important for planning observations at those wavelengths using the *James Webb Space Telescope* (*JWST*). *JWST* can in principle provide high-quality spectra for hundreds of TNOs from $1 - 5 \mu\text{m}$.

2. SPITZER/IRAC OBSERVATIONS AND DATA REDUCTION

Spitzer, with an aperture of 85 cm, was launched in August 2003 into an Earth-trailing, heliocentric orbit (Werner et al. 2004). Its Infrared Array Camera (IRAC), a broad-band imager with four channels, has a field of view (FoV) of $5.2' \times 5.2'$ and an image scale of $\sim 1.2 \text{ arcsec pixel}^{-1}$ (Fazio et al. 2004). The four broad-band channels are centered at 3.6, 4.5, 5.8, and $8.0 \mu\text{m}$ with full width at half maximum of 0.68, 0.87, 1.25, and $2.52 \mu\text{m}$, respectively. *Spitzer*’s instruments

were originally cooled by liquid helium, but this cryogen was exhausted in May 2009. Thereafter, Spitzer entered its so-called “warm mission” during which only the 3.6 and 4.5 μm channels of IRAC are operational.

From 2005 to 2016, we observed TNOs and Centaurs during different Spitzer observational cycles¹, and included all dynamical classes. In this work we present the results from a sub-sample that includes detached, classical and resonant types (see section 3.1). Data are available for download from the Spitzer Heritage Archive². Even though some objects were observed in 5.8 and 8.0 μm , only the 3.6 and 4.5 μm data are reported and analyzed here. Note that for these cold (~ 40 K) and distant objects (beyond 30 au) objects the flux at these wavelengths is only reflected light, with no thermal emission from their surfaces. A summary of observations is provided in table 5, which includes: object designation, date of observation, Spitzer-object distance (Δ), heliocentric distance (r_H), phase angle (α), flux at 3.6 and 4.5 μm ($F_{3.6}$, and $F_{4.5}$, respectively), and geometric albedo at 3.6 and 4.5 μm ($p_{3.6}$, and $p_{4.5}$, respectively).

Each object was observed twice with time intervals between several hours to several days, with the aim of having two different measurements at different locations relative to the background star fields, while keeping the object within the same FoV (movement of the object was around $30''$). This provides several benefits: identification of the object by its motion against background stars, straightforward and accurate background subtraction, and increased probability of at least one good measurement in the case of a field star obscuring the object (Emery et al. 2007). Each observation consists of nine or more dithered frames, which allows image correction for effects such as bad pixels, latent images from previous observations, and stray light from bright objects in or just off the frame.

IRAC data frames were pre-processed by the Spitzer Science Center (SSC) automated pipeline for dark, bias, and flat field corrections, and flux calibrations. Corrections for IRAC specific artifacts such as column and array pulldown, muxbleeding and stray light contamination, are done for individual frames, if necessary. The two observations per object were used as background frames for each other in order to remove diffuse flux and most of the contribution from stars in the field. Corrections (available from the SSC) for pixel solid angle vari-

Table 1. Parameters used to perform the synthetic aperture photometry.

Aperture (pix)	Annul radius (pix)	Annul width (pix)
2	2	4
2	10	10
3	3	4
3	10	10

ations and array location dependent photometric variations were applied to the frames.

We performed synthetic aperture photometry in order to calculate the flux from the object, as outlined in the IRAC Instrument Handbook³. We used four combinations of aperture radius and background annulus as shown in table 1 (Emery et al. 2007). Aperture corrections for each combination are given in the IRAC Instrument Handbook. Color corrections are calculated for each broad-band channel assuming a solar spectral slope through each passband (Smith & Gottlieb 1974). All aperture/annulus combinations and all frames in an observation are averaged together for each channel and recorded as final fluxes. Uncertainties of 1σ are reported. The uncertainties account for photon counting statistics, deviation among the dithered frames, and deviation among the aperture/annulus combinations. The absolute calibration of all IRAC channels is accurate to $\sim 3\%$ (Reach et al. 2005).

A visual inspection of each frame, the average frame, and the background subtracted frame for each observation was conducted to assess success of the observation. If objects were not discernible by eye in the observation, an upper limit calculated from the background flux is presented. The background flux is the mean of the repeated aperture photometry process for 50 random center points, removing outliers outside $\pm 2\sigma$, within a radius of 50 pixels of the location of the object predicted by its ephemeris.

With the aim of ensuring that our measurements are reliable, the objects had to satisfy the following criteria in order to be selected for the final analysis:

1. Not contaminated by a background star or image artifact.
2. Clearly visible in the average frames.
3. Greater than 3σ detection.

For any objects selected for final analysis that have $< 3\sigma$ detection, we used a 3σ upper limit calculated

¹ Specifically GO2, GO4, GO6, GO7, GO8 and GO12 cycles, with program ID 20769, 40389, 60155, 70115, 80116, and 12012, respectively.

² <http://sha.ipac.caltech.edu/applications/Spitzer/SHA/>

³ <http://irsa.ipac.caltech.edu/data/SPITZER/docs/spitzermission/>

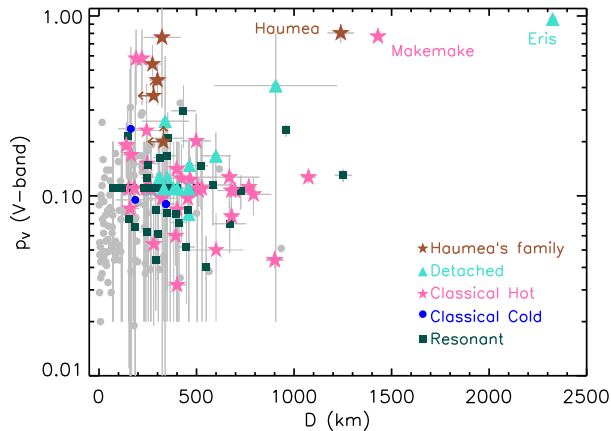


Figure 1. Diameter vs. geometric albedo in V-band from the “TNOs are Cool” sample (grey circles). Colored symbols denote objects of our sample (note that some of them have diameters assuming the median albedo calculated from Müller et al. 2020). Green squares show resonant objects, turquoise triangles show detached objects, pink stars and blue circles represent hot and cold classical objects, respectively. Brown stars represent Haumea’s family members (the brown arrows indicate lower limits Brown et al. 2007b; Snodgrass et al. 2010). Only dwarf planets and Haumea’s family members have albedos over 40%, which belong to detached and hot classical groups. The remaining objects have albedos under 40%.

from the background flux. From the total sample, 100 objects satisfied these criteria and were analyzed in this work. All measured fluxes with errors are provided in table 5.

3. SUPPORTING DATA

3.1. Dynamical classification

The dynamical classes of the objects in the sample, which are included in table 6, were determined using the numerical procedure detailed in Gladman et al. (2008).

These classifications are categorized as either secure or insecure. Given the observed on-sky location of each TNO over time, we find the best fit orbit as well as the highest- and lowest- semi-major axis orbits that are consistent with the observations⁴. These three orbits are used as starting points for 100 Myr numerical simulations. If all three “clones” show the same orbital

behaviour in these simulations, the classification is considered secure. If not, it is insecure and additional future observations are still required to establish the classification; in this case we give the best-fit classification.

Each of the dynamical classifications are designed to capture orbital behavioral characteristics, particularly to describe the manner in which each TNO is (or is not) interacting with Neptune. TNOs which are experiencing active gravitational scattering by Neptune are classified as *scattering* objects; we consider a TNO to be scattering if the semi-major axis changes by > 1.5 au over the 100 Myr simulation. *Resonant* objects are TNOs in mean-motion resonance with Neptune (resonance with Uranus are searched for, but are only known for Centaurs). We diagnose resonance by determining if a resonant angle is librating as opposed to circulating (see Gladman et al. 2008; Khain et al. 2018, for more details). TNOs that are not strongly interacting with Neptune are classified as either *detached* or *classical* objects; if the TNO is not scattering or resonant and has an initial eccentricity above 0.24, then it is called “detached”; otherwise, it is considered “classical”. Classical objects are then subdivided, based on their position relative to two major TNO resonances, as *inner* ($a < 39.4$ au, where the 3 : 2 resonance is located), *main* ($39.4 < a < 47.0$ au), and *outer* ($a > 47.0$ au). Orbital inclination i is not part of the dynamical classification because the TNO i structure is complex (varying with a), and causes confusion if an overly simplistic i cut is used. In particular, modern understanding shows that the so-called ‘cold’ component (Brown 2001) appears to be present only in the main classical belt between $42.5 < a < 47.0$ au (Petit et al. 2011), and should be located by using free inclinations i_{free} corrected for secular effects and thus measured with respect to the local Laplace pole; Van Laerhoven et al. (2019) show that the cold component then has an impressively small “inclination width” of $< 2^\circ$, and that in the main belt choosing objects with $i_{\text{free}} < 4^\circ$ gives a reasonable separation, where the majority of the objects on either side of this boundary belong to only one of the two otherwise-overlapping hot and cold components. At other semi-major axes, the “cold classical” component appears not to exist and objects with low inclinations are simply the low- i tail of the hot component.

In this manuscript, we analyzed those that did not have or are not having planetary encounters. In other words, we excluded scattering objects, which will be analyzed separately with Centaurs in a future paper. In summary, from the 101 objects that satisfied the criteria from the above section: 40 are hot classical, 4 are cold classical, 41 are resonant, and 15 are detached.

⁴ For each candidate orbit, we consider the deviation between the predicted position from that orbit versus the observed astrometry. To be consistent with observations, the worst predicted versus observed astrometric position must be no more than 1.5 times the worst from the best fit orbit, and the root mean square of these deviations must be no more than 1.5 times that of the best fit. The selected extremal orbits are then those with the lowest and highest semi-major axis.

3.2. Albedos and diameters

Different physical properties were used for our albedo calculations (see section 5). Radii and visible geometric albedos were compiled from the database of the “TNOs are cool” project⁵ (Müller et al. 2009), which is, to date, the most complete and accurate database of these properties for TNOs (Müller et al. 2020). Figure 1 shows diameters and albedos for resonant objects (green squares), detached objects (turquoise triangles), and hot and cold classical objects (pink stars and blue circles, respectively). The “TNOs are cool” sample is shown in grey circles. To maintain consistency, we also adopted the corresponding absolute magnitudes used in the “TNOs are cool” project.

Not all our objects were observed by the “TNOs are cool” project; in those instances, we used $11 \pm 9\%$, the median albedo calculated from the “TNOs are cool” database. Coupled with the absolute magnitude specified by the Minor Planet Center (MPC), we calculate the radius (R) using the equation:

$$R = C p^{-1/2} 10^{-H/5}, \quad (1)$$

where C is a constant depending on the observed wavelength (i.e., 1329 km for V-band), p and H are the geometric albedo and the absolute magnitude of the object, in the same photometric band, respectively. The same procedure was also applied to three Haumea family members that only have upper limits in their V-band albedos (Vilenius et al. 2018), specifically, 1995 SM₅₅, 1996 TO₆₆, and 1999 CD₁₅₈. For these three objects, we calculated a median value using the albedos from Haumea family members ($p_{V, \text{Haumea}} = 0.58 \pm 0.26$), as the median value for the TNO population is not representative of the family. Table 6 shows a compilation of the physical properties used in this work.

3.3. Visible and near-infrared photometric data

Ground-based observations for VNIR photometric data were compiled from published literature using the following process:

- Visible colors were taken from Peixinho et al. (2015), and near infrared (NIR) colors from Fulchignoni et al. (2008), with some of the NIR colors completed using data from Belskaya et al. (2015), MBOSS, Tegler et al. (2016), among others (see table 7).
- For objects with no color available in the above references, we used the average colors published

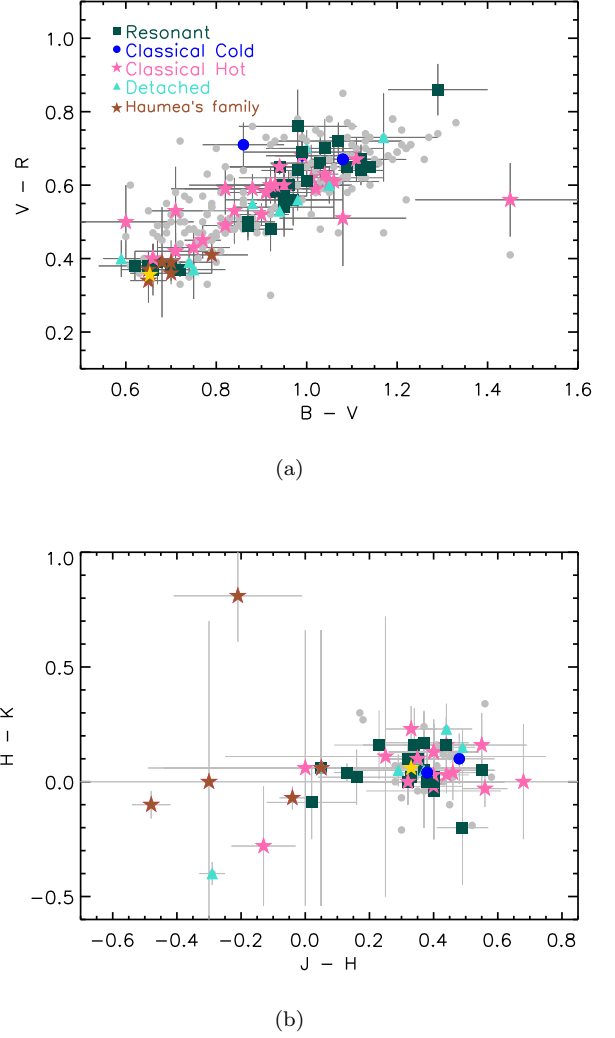


Figure 2. (a) $B - V$ versus $V - R$ color-color plot for our sample using colors and symbols to represent different populations. Grey circles represent data from Peixinho et al. (2015). (b) $J - H$ versus $H - K$ color-color plot for our sample using colors and symbols to represent different populations. Grey circles represent the sample from Fulchignoni et al. (2008). In both panels: the same scale as in Doressoundiram et al. (2008) was used in order to compare the diversity of our sample; green squares show resonant objects, triangles show detached objects, pink stars and blue circles represent hot and cold classical objects, respectively. Solar colors are indicated by a yellow star.

by Fulchignoni et al. (2008) as a function of their taxonomy (given in Belskaya et al. 2015).

- Some exceptions were made during the process: Because the NIR colors available in the literature for Makemake and Quaoar have very large errors, we decided to extract their colors using VNIR spectra published in the literature. We

⁵ <http://public-tnosarecool.lesia.obspm.fr>

also used the measured spectrum of 2002 TX₃₀₀ (Licandro et al. 2006a) and synthesized its NIR colors because they are unavailable in the literature.

As can be seen in figure 2, our sample exhibits the full diversity of colors reported by different surveys (e.g., Barucci et al. 1999; Delsanti et al. 2001, 2004, 2006; Boehnhardt et al. 2002; Doressoundiram et al. 2001, 2002, 2005, 2007; DeMeo et al. 2009; Perna et al. 2010). Table 7 provides a compilation of colors for our sample. The reference for each object and any exceptions to the process to select the reference are included in the table.

3.4. Spectroscopic data

Spectra were also compiled as a baseline to understand our sample and to assess whether our compilation of colors that are translated to spectrophotometric measurements (i.e., geometric albedo versus wavelength) are in agreement with the spectra. We followed the work performed by Barucci et al. (2011) regarding surface composition of TNOs using VNIR spectra. We used this work as a reference for water and other ices detection because it provides a homogeneous analysis of spectra for, at least, some of our targets. However, because this review was published eight years ago, we also searched into more recent papers in order to find spectra published for other objects.

Although we have not performed any calculation to measure bands, we followed the criteria of Barucci et al. (2011), in which three categories are defined: objects with clear detection of absorption bands reported by the authors are considered “sure detections”, objects with some indications of absorption bands reported by the authors are considered “tentative detections” and objects with no indications of absorption bands reported by the authors are considered “no detections”.

Literature regarding the spectra used in this work are cited in sections 5 and 7, where each object is independently analyzed. In general, there is good agreement for the whole sample, as demonstrated in appendix B. There exists only 5 exceptions in which the spectrum and the spectrophotometric measurements do not completely agree (discussed in section 6).

4. REFLECTANCE AND COLOR INDICES

4.1. Reflectance

Fluxes in the IRAC wavelengths are converted into geometric albedos in order to be combined with ground-based data and to plot as spectrophotometric measurements. The geometric albedo (p_λ) at wavelength λ , is

given as follows:

$$p_\lambda = \frac{F_\lambda r_H^2 \Delta^2}{F_{\odot, \lambda} \Phi R^2}, \quad (2)$$

where F_λ is the measured flux at wavelength λ ; $F_{\odot, \lambda}$ is the solar flux at 1 au at the same wavelength; r_H is the heliocentric distance in au; Δ is the Spitzer-centric distances in km; R is the radius of the object in km and Φ is the phase correction factor. We have calculated the phase correction factor by $\Phi = 10^{\frac{-\beta\alpha}{2.5}}$; where α is the phase angle with respect to Spitzer, and $\beta = 0.14^{+0.07}_{-0.03}$ mag deg⁻¹ is the median of phase coefficients tabulated by Alvarez-Candal et al. (2016), where we have excluded values that are negative or greater than 0.5 as these are likely due to uncharacterized rotational light-curve effects⁶.

Colors from the literature were also converted into geometric albedo by means of the equation:

$$p_R = p_V 10^{\frac{(V-R) - (V-R)_\odot}{2.5}}, \quad (3)$$

where p_R is the albedo in R -band, p_V is the albedo in V -band, $(V-R)$ is the color of the object and $(V-R)_\odot$ is the color of the Sun. Analogous relations are used for the other colors, in our particular case: $(B-V)$, $(V-I)$, $(V-J)$, $(V-H)$ and $(V-K)$. As a result, spectrophotometric measurements have been incorporated for each object (see appendix B), allowing us to analyze the surface composition using the widest possible wavelength range (see section 5).

Note that, from Eq. (2), the IRAC albedo depends on the radius R explicitly and, therefore, one may expect that the large relative uncertainties in the measurements of the radius of known objects would translate into large relative uncertainties in the IRAC albedos. However, Eq. (1) provides a workaround, as one can check explicitly that combining both Eqs. (2) and (1) results into an expression for the ratio of the ground-based V -band geometric albedo and IRAC albedo, p_V/p_λ that does not depend explicitly on the radius R nor p_V (in other words, in the resulting combined equation only the relative albedo plays a role). Hence, if one focuses on the relative albedos (i.e., on the absorption), the effect of large uncertainties in R is neutralized, provided, of course, that R and p_V are constrained to satisfy Eq. (1). Table 2 shows median and average values for the geometric albedos at 3.6 and 4.5 μm of our sample, while tables 5

⁶ The median value using the complete sample was $\beta = 0.1 \pm 0.1$ mag deg⁻¹, which produces an error of the same order of magnitude than the β value; for that reason, for that reasons, outliers were excluded first.

and 8 show the geometric albedos obtained for each object at IRAC and VNIR wavelengths, respectively. Note that measurements at 3.6 and 4.5 μm were taken consecutively one after the other. The total exposure times (including all sub-exposures) were no longer than 40 min at 3.6 μm . Considering that the faster rotation period for a TNO known to date is 4 hours (Haumea), with a median value of ~ 8 hours (Thirouin et al. 2012), large effects due to rotational variability between both filters are very unlikely.

4.2. Color indices

In order to combine our IRAC/Spitzer measurements with existing apparent magnitude measurements at shorter wavelengths, we define colors, expressed as magnitude differences, as:

$$\begin{aligned} m_1 - m_2 &= -2.5 \log \left(\frac{F_1/S_1}{F_2/S_2} \right) \\ &= -2.5 \log \left(\frac{F_1}{F_2} \right) + 2.5 \log \left(\frac{S_1}{S_2} \right), \end{aligned} \quad (4)$$

where F_n is the flux from the target in a given band, and S_n is the solar flux in that band (with $n = 1, 2$). In what follows we denote these colors as “V - 3.6 μm ”, “J - 3.6 μm ”, “K - 3.6 μm ”, and “3.6 μm - 4.5 μm ”. Because these colors are corrected for the intrinsic solar color, they can be related to the albedos in the bands, for example:

$$3.6 \mu\text{m} - 4.5 \mu\text{m} = -2.5 \log \frac{p_{3.6}}{p_{4.5}}, \quad (5)$$

where 3.6 μm - 4.5 μm is the color from IRAC/Spitzer measurements, $p_{3.6}$ is the geometric albedo at 3.6 μm and $p_{4.5}$ is the geometric albedo at 4.5 μm . Other colors using IRAC/Spitzer broad-band and ground-based measurements can be obtained using the same equation. A compilation of the different colors used in the analysis is shown in table 9.

5. RESULTS

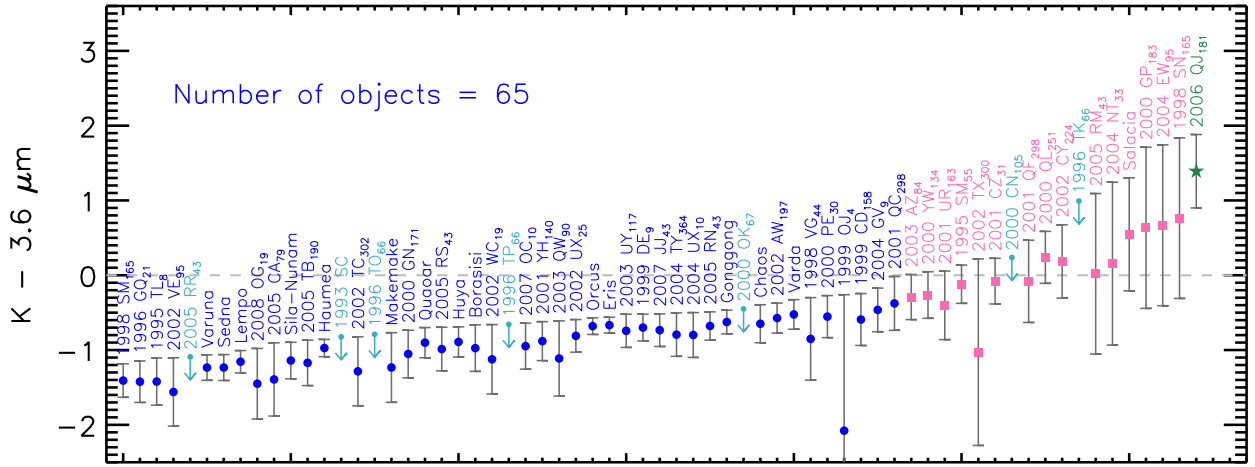
Below we present our results in two ways: (1) by comparing the color indices we have measured to synthetic color indices computed from synthetic reflectance models for pure substances and binary- and ternary mixtures of those substances, and (2) by presenting the measured reflectance spectra (i.e., spectrophotometric measurements) of all objects along with measured visible - near-IR spectra found in the literature, or spectral models if available (see appendix B).

5.1. Measured Colors, and synthetic spectra

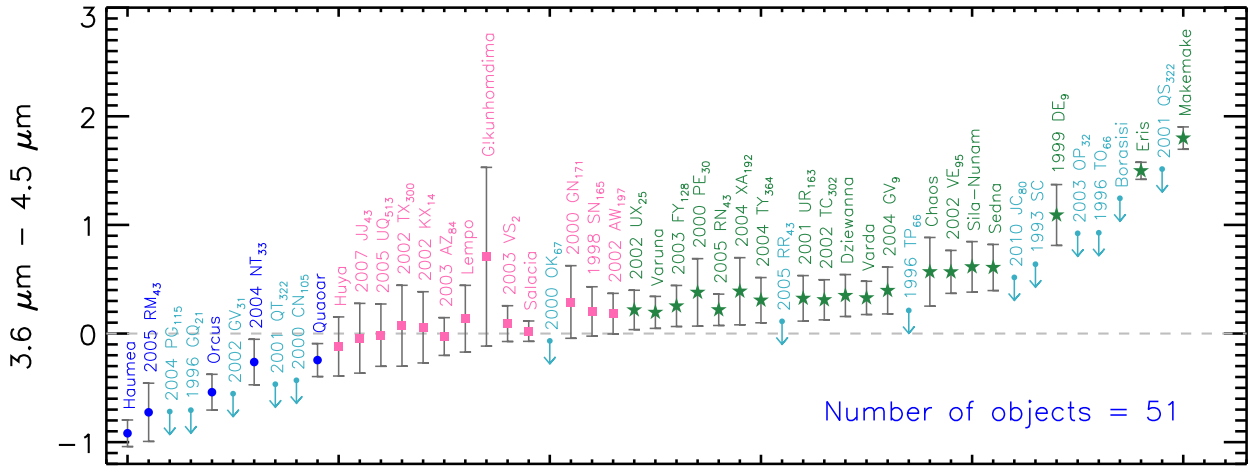
Figure 3 shows the measured K vs. IRAC color indices for all of our targets. Note that not all the objects of our sample presented measurements at 4.5 μm or published data in the K band, which drops the number of objects to 66 and 52 for $K - 3.6 \mu\text{m}$ and $3.6 \mu\text{m} - 4.5 \mu\text{m}$, respectively. From the upper panel in figure 3 we see that, from the 65 objects with $K - 3.6 \mu\text{m}$, 48 present 1σ independent probability of having an absorption at 3.6 μm (74% of the sample), with 44 objects representing the 1σ compound probability (i.e., 68%). Only one object present 1σ independent probability of not having absorption at 3.6 μm , with 2 objects representing the 1σ compound probability (i.e., 3%). Additionally, and as shown in the bottom panel, with a total of 51 objects, 11 objects present 1σ independent probability of having an absorption at 3.6 μm (22% of the sample), with the same number of objects representing the 1σ compound probability. From both panels we can appreciate that the range of colors is significantly larger than seen in the visible - near-IR wavelengths (e.g., Fulchignoni et al. 2008; Peixinho et al. 2015; Schwamb et al. 2019), suggesting the potential of using the IRAC colors to constrain TNO composition in ways that have previously been impossible. Figure 4 shows synthetic spectral models for some materials typically found, or expected to be present, on TNOs and Centaurs. The figure illustrates how much stronger the absorption bands of most of these materials are at the IRAC wavelengths than in the near-IR. This is because the longer-wavelength absorptions are associated with fundamental molecular vibration frequencies, while those shortward of 2.5 μm are weaker overtone bands, which explains the strong color diversity of TNOs seen in figure 3. Other colors are also important for constraining composition, and help establish continuum levels (particularly true for J , H and K -band). In addition to the colors discussed above, we also use V -3.6 μm and J -3.6 μm colors in the following analysis. Table 9 shows our compilation of all the colors for our targets (including the aforementioned and VNIR colors) used in this work.

5.2. Spectrophotometric measurements

Our compilation of visible-near-IR and IRAC spectrophotometric measurements for each object are plotted in terms of geometric albedo in appendix B. The measurements were converted to albedo as described in section 4. When a previously-published visible-near-IR spectrum of an object is available, it is also plotted to allow comparison to our IRAC results. The figures are ordered by provisional designation in ascending order, followed by the named objects in alphabetical order. The albedo spectra are shown for all objects, regardless



(a)

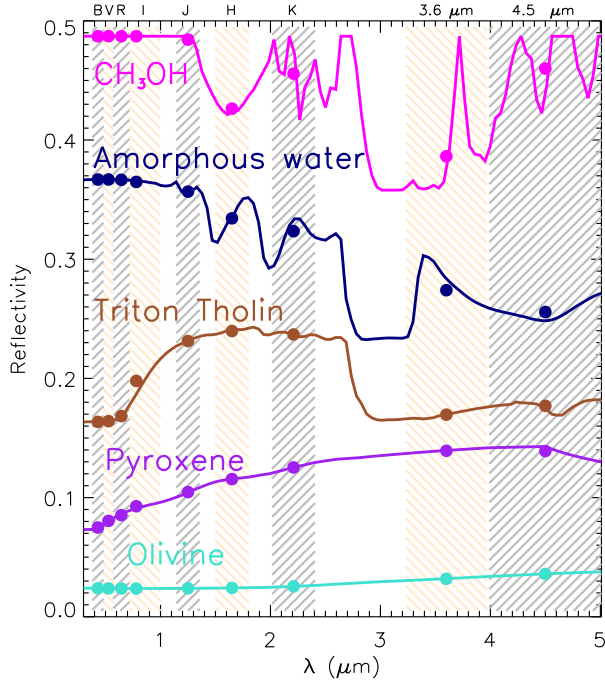


(b)

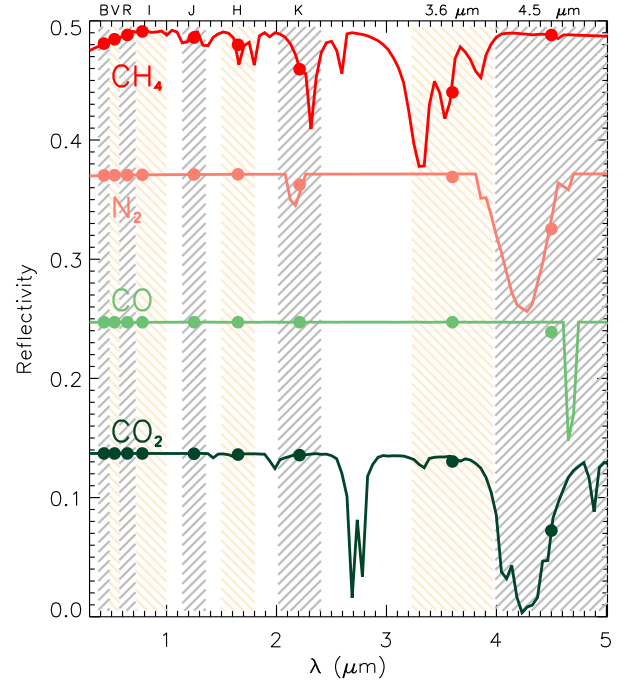
Figure 3. K -band vs. IRAC color indices for our entire sample, plotted in order of increasing color index. Negative (positive) values indicate absorption in the longer (shorter) wavelength; zero indicates neutral (*i.e.*, solar) colors (horizontal dashed line). Note that not all the objects of our sample presented measurements at $4.5\ \mu\text{m}$ or published data in the K band, which drops the number of objects to 65 and 51 for $K - 3.6\ \mu\text{m}$ (upper panel) and $3.6\ \mu\text{m} - 4.5\ \mu\text{m}$ (bottom panel), respectively. There are also a few objects that have only upper-limits in both IRAC bands, so those are also not plotted in the bottom panel. **Error bars give $1 - \sigma$ uncertainties while arrows give $3 - \sigma$ upper limits.** Objects with $1 - \sigma$ independent probability of presenting absorption at $3.6\ \mu\text{m}$ (upper panel) and $4.5\ \mu\text{m}$ (bottom panel) are represented by blue circles and are labeled in blue, objects with $1 - \sigma$ independent probability of **no** presenting absorption are plotted as green stars and labeled in green. Objects that error bars overlap both regions are represented by pink squares and labeled in pink. Object for which upper limits have been determine are represented by turquoise arrows and are labeled in turquoise. The range of TNO colors in these bands ($\gtrsim 2\text{mag}$) significantly exceeds that seen in the visible ($\lesssim 1\text{mag}$; see figure 2 and e.g., [Peixinho et al. 2015](#); [Schwamb et al. 2019](#)).

Table 2. Median and average values for the geometric albedos and colors obtained in this work. Abbreviations are defined as follows: geometric albedo at 3.6 and 4.5 μm ($p_{3.6}$, $p_{4.5}$, respectively).

	$p_{3.6}$	$p_{4.5}$	$3.6 - 4.5$ (mag)	$V - 3.6$ (mag)	$J - 3.6$ (mag)	$K - 3.6$ (mag)
Median	0.12 ± 0.01	0.15 ± 0.03	0.2 ± 0.1	0.0 ± 0.1	-0.9 ± 0.1	-0.9 ± 0.1
Average	0.16 ± 0.05	0.21 ± 0.05	0.3 ± 0.2	0.1 ± 1.0	-0.7 ± 0.3	-0.8 ± 0.6



(a)



(b)

Figure 4. Synthetic reflectance spectra of some pure materials expected or known to exist on the surfaces of small TNOs and Centaurs (left) and additional molecular ices found on TNO dwarf planets (right). The particle size was 10 μm for all materials except for N_2 , where the particle size is 10 cm. Vertical grey and brown shaded bars indicate VNIR and IRAC/Spitzer filter bands, as labeled along the top axis. The bandwidth is the full width of the band at 50% of the average in-band transmission. Dots represent the spectrophotometric measurements as given by the convolution of each synthetic spectrum with the filters. For clarity, reflectance have been shifted by an arbitrary offsets as follows: olivine (0.02), pyroxene (0.07), Triton tholin (0.16), amorphous H_2O (0.23), CH_3OH (0.35), CH_4 (0.355), N_2 (0.235), CO (0.11), and CO_2 (no offset).

Table 3. References of the optical constants for the synthetic models used in this work.

Model	Temperature (K)/Phase	Reference
CH ₃ OH	90	Robert Brown*
CH ₄	40	Grundy et al. (2002)
N ₂	21	Quirico & Schmitt (1997)
CO	21	Quirico & Schmitt (1997)
CO ₂	150	Hansen (1997)
H ₂ O	120 amorphous	Mastrapa et al. (2009)
H ₂ O	150 crystalline	Mastrapa et al. (2009)
Triton Tholin	Not available	Imanaka et al. (2012)
Titan Tholin	≈ 290	Khare et al. (1984)
Pyroxene 5: Mg _{0.7} Fe _{0.3} SiO ₃	amorphous	Dorschner et al. (1995)
Pyroxene 8: Mg _{0.4} Fe _{0.6} SiO ₃	amorphous	Dorschner et al. (1995)
Olivine 1	amorphous	Dorschner et al. (1995)
Olivine 2	amorphous	Dorschner et al. (1995)

*See Appendix in Cruikshank et al. (1998).

of whether we found *J*- and/or *K*-band photometry in the literature. The objects lacking those measurements are excluded from the color index analysis we present below.

Inspecting each albedo spectrum in appendix B, we found that seven of our objects do not show absorption at 3.6 and 4.5 μm with respect to the *K*-band. Referencing figure 4, it seems plausible that such objects have surfaces dominated by amorphous silicates. Those objects are: 1998 SN₁₆₅, 2000 GP₁₈₃, 2000 QL₂₅₁, 2002 CY₂₂₄, 2004 EW₉₅, 2006 QJ₁₈₁ and Salacia, which have positive *K* - 3.6 μm colors in figure 3. The remaining objects have absorption identification in at least one of the two IRAC/Spitzer bands. These absorption identifications are related to either ices (H₂O, CH₄, CH₃OH,...) or complex organics, as explained below.

6. ANALYSIS

6.1. Synthetic Color Indices

In order to interpret the colors of our objects in terms of composition, we computed synthetic spectral models for the substances shown in figure 4 and table 3, using a range of grain sizes for each component. We convolved the synthetic spectral models with the Johnson-Cousins-Bessell standard filter system (Johnson 1964; Bessell & Brett 1988; Bessell 2005), and the IRAC broadbands (Fazio et al. 2004), to derive synthetic photometry and colors for the synthetic spectra. Figure 5 illustrates the results for the *K* - 3.6 μm and 3.6 μm - 4.5 μm color indexes (circles) for the pure materials as a color-color diagram. There are distinct regions that can be attributed to most of the materials we consider, with the color vs. grain-size trends extending approximately radially in different directions from

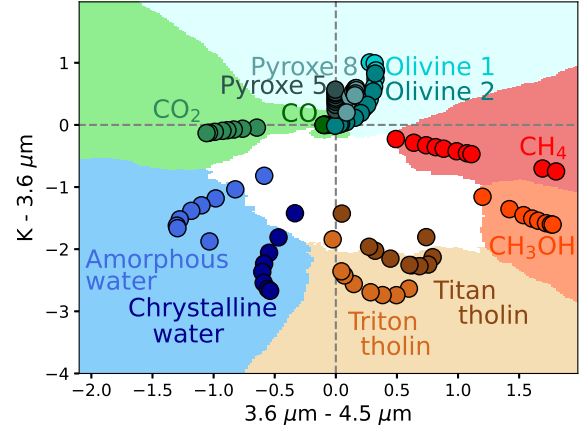


Figure 5. “Compositional-clock”: color-color diagram for *K* - 3.6 μm versus 3.6 - 4.5 μm synthetic colors for pure materials (each plotted with a different color and symbol, and labeled). Colors were synthesized from spectral models using grain sizes from 10 - 100 μm in 10 μm increments (CH₄ also included 400 and 500 μm). The larger the grain, the deeper the absorption band produced, and therefore grains of 10 μm are nearest to the origin of the plot.

the origin for each material. Because of this layout, we informally call this diagram the “compositional clock”. While most of the materials result in color trends at different ‘times’ on the clock, CO₂, CO and N₂, occupy nearly the same region (for clarity within the diagram, we did not represent the N₂ in figure 5), although for a given color the relevant grain size would be orders of magnitude larger for CO or N₂ than for CO₂. While the trends for these pure materials are simple, minor changes to the model assumptions, such as having a distribution of grain sizes or mixtures of different materials

complicate these trends. In order to plot the region of influence for each pure material, we have applied the K-Nearest neighbors (KNN) method (Hastie et al. 2001; James et al. 2013), as implemented in `scikit learn` (Pedregosa et al. 2011), with $K = 15$, and assigning weights proportional to the inverse of the distance from the query point. The method will classify each coordinate in the graphic considering the 15 nearest points provided by the models, filling the empty regions of the diagram. The selection of K was made by inspection of the results provided by different values. Small values of k will be too moldable leading to unstable decision boundaries, and large values of K will have smoother decision boundaries which mean lower variance but increased bias (also, computationally expensive). A good estimation is made from the square root of the total number of models (in our case, we have 207 points of synthetic materials, i.e., $K \sim 15$). We inspected values of K between 10 and 25, which produced similar results, and therefore we chose 15 as a good compromise. Each colored region is dominated by a different material (water, complex organics, methanol, methane, silicates, and supervolatiles-CO and CO_2), while the white region is dominated by different mixtures of those materials, as explained below.

Surfaces of TNOs are very unlikely to be dominated by pure materials, so we now explore synthetic colors for intimate combinations between spectral models for three of our representative components (i.e., olivine 1, Triton tholin and amorphous H_2O), with each component having a single grain size. The intimate mixtures have been carried out using Hapke scattering models (Hapke & Wells 1981; Hapke 1993). The results are shown in figure 6 for mixing between each pair of components (a) and between all three components (b). If additional combinations of grain sizes and/or mixtures between more than three components are considered, the region covered in the color-color diagram would expand, but still be bounded by the colors of the pure components. The figure shows that surfaces with significant fractions of multiple components can have colors that deviate from the trends seen for the pure materials in figure 5, but also illustrates that the colors for such surfaces are still confined to certain regions of the diagram, and therefore can constrain the composition in useful ways, and exclude the presence of some components.

6.2. Compositional interpretation of the TNO colors

In order to explore the utility of the synthetic colors and color-color diagram discussed above, we now plot the measured colors for our targets and include the com-

position regions and color trends shown in figure 5 and figure 6. To start, we focus on 12 objects with relatively well-understood spectral properties, shown in figure 7 (a). (Albedo spectra for these objects are given in appendix B.) Fortunately, the colors of these objects span much of the color-color diagram, providing a fairly complete sample for testing the predictions based on the compositional-clock approach. The colors of all 12 objects appear to be roughly consistent with the predictions based on synthetic colors for the pure substances and simple mixtures between those substances. To obtain the proportion of each material for each object, we have implemented a routine that interpolate using the KNN method (Hastie et al. 2001; James et al. 2013). For each object (or observational point), we calculate the euclidean distance to search for the K -nearest points given by the synthetic models. The selection of K was made following the same procedure explained in section 6.1, which lead to $K = 15$. Then, we average the different proportion of each material for each point to provide an interpolation for each object. To calculate the errors in the proportions, we obtained the uppermost and lowest value of each of the two colors considering their error bars, which provides four new points for each object (these are arranged in the form of a cross around the central value). We applied the K -nearest method to calculate the proportion of different materials for each of those four new points. We obtained the difference between the proportion of each material given for the object and the proportion of each material given the four new points. For a more conservative perspective, we chose as the error the biggest difference from those obtained from opposite points in the cross shape.

Haumea plots squarely in the H_2O -ice pure region, as expected based on previous studies (e.g., Trujillo et al. 2007; Merlin et al. 2007; Pinilla-Alonso et al. 2009). We obtain a composition of $80 \pm 5\%$ H_2O , $10 \pm 10\%$ silicates, $10 \pm 10\%$ organics.

Quaoar has been found to have large amounts of water ice in its surface according to absorption bands at 1.5, 1.65 and $2.0 \mu\text{m}$ (Jewitt & Luu 2004; Schaller & Brown 2007b; Guilbert et al. 2009; Dalle Ore et al. 2009). Another band was found at $2.2 \mu\text{m}$, which has produced some discussion among the different authors, suggesting that this band could be either due to ammonia hydrate ($\text{NH}_3 \cdot \text{H}_2\text{O}$) or CH_4 . The model by Dalle Ore et al. (2009) also included photometric data at wavelengths 3.6 and $4.5 \mu\text{m}$ from Spitzer. They claim a surface composition of $\sim 40\%$ H_2O , $\sim 10\%$ CH_4 , and $\sim 50\%$ complex organics. They also fit a different model with including up to 20% N_2 . Taking into account those percentages of water and complex

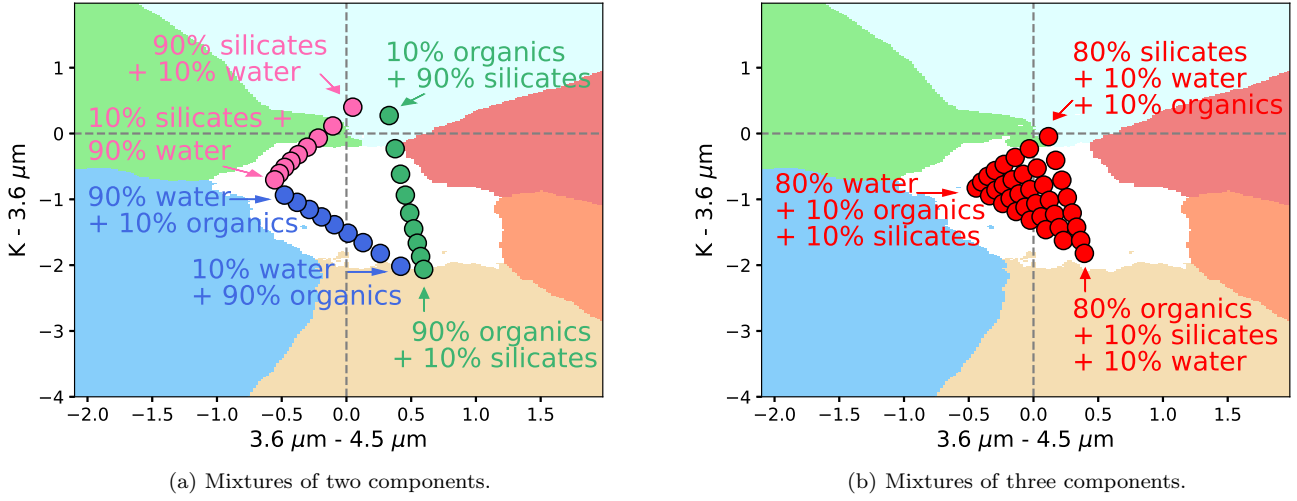


Figure 6. Same color-color space as in figure 5, but showing trends for intimate mixing between two (left, panel a) and three (right, panel b) components. Here we have chosen amorphous H_2O ice, Triton tholin, and olivine 1 as representative materials, and we show only the $10 \mu\text{m}$ grain size results. Models including crystalline and amorphous H_2O have similar relative positions in the diagram. For comparison, we plotted the same colored regions as in figure 5, to indicate those regions dominated by pure materials.

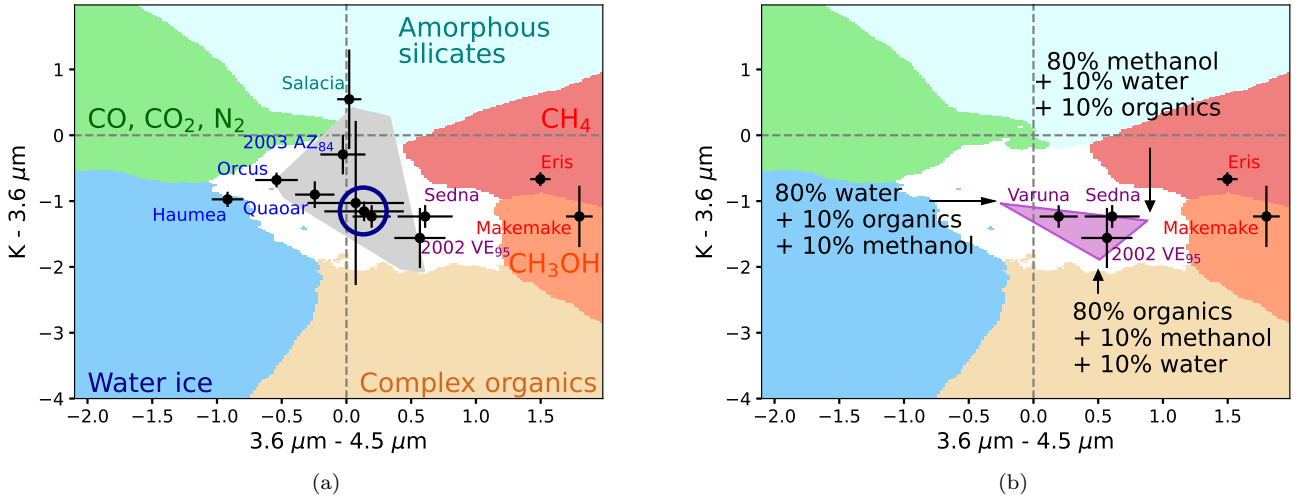


Figure 7. Color-color diagram, similar to figure 5, including the shaded regions for pure materials, and with measured colors of 12 TNOs with relatively well-characterized compositions from VNIR spectroscopic observations. Left: Target names are given in colors indicating whether the spectrum has previously been characterized as having H_2O (blue), CH_4 (red), or CH_3OH (purple). Silicates (turquoise) has not been detected in Salacia, however, its flat spectrum and low albedo is consistent with our results shown in this diagram of a surface composition dominated by silicates. Objects surrounded by a blue circle are 2002 TX₃₀₀, Lempo and Varuna (from left to right). The grey polygon is bounding the regions shown in figure 6 for binary and ternary models of H_2O , Olivine 1 and Triton tholin (i.e., H_2O , silicates, and organics). Right: the colors for Varuna, Sedna and 2002 VE₉₅ are compared to ternary mixing models of amorphous H_2O , Triton tholin and CH_3OH with grain sizes of $10 \mu\text{m}$.

organics, Quaoar should appear in a region in the color-color diagram slightly more downward and rightward than depicted. Considering our method, we obtain a composition of $60 \pm 10\%$ H₂O, $20 \pm 10\%$ silicates, and $20 \pm 10\%$ complex organics. Note that for simplicity we have not included mixtures with supervolatiles; nonetheless, if there exists N₂ on its surface, which overlaps the CO region in the $K - 3.6 \mu\text{m}$ vs. $3.6 \mu\text{m} - 4.5 \mu\text{m}$ diagram, the data point for Quaoar can be displaced up and to the left, towards its position shown in figure 7 (a). The water percentage is consistent with the models provided by [Dalle Ore et al. \(2009\)](#), and the variation in the other materials could be due to the inclusion of CH₄ and N₂ on their mixtures. Overall, its position is consistent with the models provided by [Dalle Ore et al. \(2009\)](#).

Orcus has been studied by several authors, and most of them agree in a composition with a low percentage of water ([Fornasier et al. 2004a](#); [de Bergh et al. 2005](#); [Delsanti et al. 2010](#)). Others have fit models with larger amounts of water, for instance, [Trujillo et al. \(2005\)](#) imposed an upper limit of 50% water ice and [Barucci et al. \(2008\)](#) modeled the spectrum with $\sim 40\%$ water ice. [DeMeo et al. \(2010\)](#) also modeled the spectrum of Orcus with a larger amount of water (up to 70%), claiming that models from earlier papers (i.e., [Fornasier et al. 2004a](#); [de Bergh et al. 2005](#)) and [Trujillo et al. \(2005\)](#) did not include the albedo of Orcus, which was published by [Stansberry et al. \(2008\)](#). [DeMeo et al. \(2010\)](#) also discussed that the difference between their model and the model in [Barucci et al. \(2008\)](#) may be due to a different blue component used to fit the data. Other ices, such as CH₄, NH₃ and, C₂H₆, have been proposed for Orcus ([Trujillo et al. 2005](#); [Delsanti et al. 2010](#)), and the presence of CO₂ is hypothesized to not exceed 5% ([DeMeo et al. 2010](#)). Our data, which include the *V*-band albedo, is consistent with a large amount of water on the surface of Orcus, as can be seen in figure 7 (a), our method produces a composition of $70 \pm 10\%$ H₂O, $20 \pm 10\%$ silicates, and $10 \pm 10\%$ complex organics. Smaller amounts of water would be also consistent with our measurements if we include other volatiles (e.g., CO₂, N₂) in the mixture.

Another object that has its surface distinctly dominated by water ice is **2002 TX₃₀₀**, which is part of Haumea’s family (see its spectrum in appendix B and [Licandro et al. 2006a](#); [Barkume et al. 2008](#)). We obtain a composition of $30 \pm 30\%$ H₂O, $30 \pm 50\%$ silicates, and $40 \pm 50\%$ complex organics, which is consistent with the spectroscopic measurements considering the error bars. However, we think that given the high proportion of water detected through its spectrum (see e.g.,

[Licandro et al. 2006a](#)), our method does not seem to be very accurate for this specific object. This could be due to the extremely wide absorption bands produced at $3.6 \mu\text{m}$ and $4.5 \mu\text{m}$ by the water, that could overlap one another, producing uncertainty on the photometric measurements when using wide pass-bands as those used in this work (see figure 4). Also, the presence of CH₃OH could move its position rightward as explain in section 8.3. (Note that NIR colors of this object were extracted from its spectrum, for which p_V is needed; therefore the large uncertainty on p_V translates into large uncertainty on the NIR colors).

Spectral models for **2003 AZ₈₄** have included 17 – 44% of water and small amounts of organic compounds ([Barkume et al. 2008](#); [Guilbert et al. 2009](#); [Barucci et al. 2011](#)). In the color-color diagram it plots in a region intermediate between H₂O-dominated and silicate-dominated colors, with a composition of $30 \pm 10\%$ H₂O, $60 \pm 20\%$ silicates, and $10 \pm 10\%$ complex organics. If organics are present, these will not be greater than 20%, which is consistent with its slightly steeped spectral slope.

The spectrum of **Lempo** has been modeled with different proportions of H₂O-ice, complex organics and silicates (5 – 35%, 10 – 65% and, 0 – 85%, respectively; [Dotto et al. 2003](#); [Merlin et al. 2005](#); [Barkume et al. 2008](#); [Guilbert et al. 2009](#); [Protopapa et al. 2009](#)). The position of this object in the color-color diagram corresponds to a composition of $30 \pm 20\%$ H₂O, $20 \pm 10\%$ silicates, and $50 \pm 10\%$ complex organics, in agreement with the proportions above mentioned. This is also supported by the $3.6 \mu\text{m} - 4.5 \mu\text{m}$ versus $3.6 \mu\text{m}$ and the $V - 3.6 \mu\text{m}$ versus $J - 3.6 \mu\text{m}$ diagrams (see section 7).

Eris and **Makemake** both have spectra dominated by CH₄ and spectral models suggest particle sizes as large as 20 mm for Eris ([Licandro et al. 2006b](#); [Merlin et al. 2009](#)), and 1 cm for Makemake ([Licandro et al. 2006c](#); [Brown et al. 2007a](#)), and both appear well inside the methane region. Note that Makemake is at the boundary between methane and methanol, where these classification methods do not provide accurate results. Also note that, comparing with figure 5, its position is closer to points corresponding to larger methane particles than to those corresponding to methanol particles. Since it is clear that they have a composition dominated by pure methane and that the grain size is playing an important role, given their position in the compositional clock, for these two objects we have applied the KNN method to obtain the grain size of this material. For this calculation, we took only methanol models and added 6 models with larger grain sizes (specifically, 0.4, 0.5, 1, 1.5, 2, 2.5, 5, 10 mm). We

did not include larger sizes because the position of the objects in the diagram clearly indicated sizes between 0.4 and 1 mm. In total we had 15 models from 0.01 to 10 mm to perform the KKN method, for which we chose $K = 5$ following the same explanation given in section 6.1. We obtain a particle size of 0.2 ± 0.1 and 1 ± 0.4 mm for Eris and Makemake, respectively. Even though our models result into particle sizes smaller than those obtained by the spectroscopic models, they manifest the necessity of using larger particle sizes. The difference between the measured grains sizes and those considered here can be explained due to the response of methane molecules at 3.6 and 4.5 μm , which is higher than in the visible, producing wider absorption bands.

Salacia is an object with a very flat spectrum (Pinilla-Alonso et al. 2008; Schaller & Brown 2008), for which no H_2O -ice or other absorption features have been documented. Pinilla-Alonso et al. (2020) suggest that this object has a highly processed surface cover by a mixture of carbon and amorphous silicates. Its position within the silicate region of the color-color diagram results in a proportion of $10 \pm 20\%$ H_2O , $90 \pm 20\%$ silicates and no organics, consistent with the lack of features that has been detected before.

Sedna and **2002 VE₉₅** are objects for which water ice has been detected in their spectra, yet both objects appear well away from the H_2O -ice region in the color-color diagram. However, their locations are clarified if we consider ternary mixtures of H_2O , complex organics, and CH_3OH , as shown panel b, figure 7. Because CH_4 and CH_3OH occupy a similar region in the compositional clock, a similar location for each object is displayed if we use CH_4 instead of CH_3OH , which makes it impossible to distinguish between them using this method. However, we can indicate the presence of CH_4 and/or CH_3OH on the surface of the objects, and confirm their existence using VNIR spectroscopy, as CH_4 and CH_3OH behave quite different at those wavelengths (see figure 4). Sedna’s spectrum has been modeled by Emery et al. (2007) using VNIR spectroscopy and Spitzer measurements at 3.6 and 4.5 μm . They found the best model was given by a mixture of 50% CH_4 , 25% complex organics, 15% H_2O and, 10% N_2 , which agrees with Sedna’s position in the color-color diagram, that corresponds to a composition of $25 \pm 10\%$ H_2O -ice, $50 \pm 10\%$ CH_4 , and $25 \pm 10\%$ complex organics. The spectrum of 2002 VE₉₅ has been modeled using 12–13% H_2O , 10–12% CH_3OH , 64–78% complex organics, and 0–11% silicates (Barucci et al. 2006; Barkume et al. 2008). This is consistent with 2002 VE₉₅’s position in the color-color diagram, which corresponds to $20 \pm 10\%$ H_2O , $40 \pm 10\%$ CH_3OH , and $40 \pm 20\%$ organics.

Varuna has been found to have absorption bands related to water ice (Licandro et al. 2001; Barkume et al. 2008). Also, Lorenzi et al. (2014) fit its spectrum using two different mixtures: one composed of 25% water, 25% silicates, 35% complex organics, and 15% carbon; and a second one composed of 20% water, 25% silicates, 35% complex organics, 10% carbon and 10% of CH_4 . The position of this object in the compositional clock results in different proportion of water depending on whether the mixture is a combination of water-silicates-organics or water-methanol-organics. For the former the resulting composition is $30 \pm 10\%$ H_2O -ice, $20 \pm 10\%$ silicates, and $50 \pm 10\%$ organics, while for the latter the resulting composition is $50 \pm 10\%$ H_2O -ice, $20 \pm 10\%$ methane, and $30 \pm 10\%$ organics. A combination between both mixtures is in agreement with the spectroscopic models.

Based on the test cases presented, we find that overall the color-color diagram provides compositional information that is consistent with that derived from visible to near-IR spectral fits for well-characterized TNOs. Appendix A presents an individually exploration to understand the composition, based on IRAC data, for the large numbers of objects in our sample, that lack detailed characterization in the visible and near-IR wavelengths.

7. OTHER COLOR-COLOR DIAGRAMS

We have built other color-color diagrams in order to verify and/or identify the different components that dominate the surface of our sample (see figure 8). The result of these diagrams are explained similarly to the compositional clock.

Of special interest is the diagram 3.6 – 4.5 μm versus $V - 3.6 \mu\text{m}$. Synthetic models of the components plotted in the compositional clock can be seen in figure 8, left panels, where pure materials, mixtures of two components, and mixtures of three components are plotted. The region of influence of each material has been plotted using the KNN method as explained in section 6.1. The inconvenience of this diagram is that the organic materials occupied a very similar region to the silicates, so we can not distinguish between them. Also, comparing the three panels it can be seen that the mixtures with high percentages of silicates and/or organics overlap the regions occupied by models of pure materials, which makes that region unuseful for our purpose. This is noticeable, for instance, when using the K-nearest neighbor method, which produces blurred results in that region. However, there are two advantages. The first one is that, because there are more objects observed with visible colors than near infrared colors, we can analyze a larger sample than using the compositional clock. The second is that some

organic materials change their position with respect to the compositional clock, therefore we are able to distinguish between complex organics and CH_4 , and CH_3OH compounds more easily.

In figure 8, right panels depict models by the colors $V - 3.6 \mu\text{m}$ and $J - 3.6 \mu\text{m}$. As in the other cases, this figure shows models of pure materials, mixtures of two components, and mixtures of three components (panels b, d and f, respectively). In this diagram, models with higher proportions of silicates are in the upper right quadrant and organic materials appear in a completely different region than the other materials. Meanwhile, super volatiles are nearly indistinguishable and H_2O , CH_4 , and CH_3OH share the same region in the lower left quadrant. For that reason, we have applied the KNN considering one region for H_2O , CH_4 , and CH_3OH models (pink shaded region), while the rest of the colors are equivalent to the other diagrams. This diagram is specially suitable for the identification of complex organics.

At VNIR wavelengths (up to $2.2 \mu\text{m}$) complex organics and amorphous silicates present a very similar behaviour, with no absorption bands (Cruikshank et al. 2005). Therefore, we can only claim indications of objects with higher proportions of complex organics than silicates and vice-versa depending on the slope of the spectrum, i.e., objects with abrupt slope will be model using complex organics, while for objects with less abrupt slopes, the spectrum will be model by a combination of silicates and complex organics (Emery & Brown 2004). However, the different behavior of silicates and complex organics at IRAC wavelengths (figure 4) enables separation of these two materials in the compositional clock and the $J - 3.6 \mu\text{m}$ vs $V - 3.6 \mu\text{m}$ diagram (panels b, d, and f in figure 8), allowing the identification of complex organics (due to absorption bands beyond $2.2 \mu\text{m}$), and demonstrating that the wide band-pass of IRAC at 3.6 and $4.5 \mu\text{m}$ are a powerful tool to identify, for the first time, what the coloring agent that produces redness on TNOs is.

8. THE SURFACE COMPOSITION OF OUR SAMPLE

We have demonstrated the consistency of our photometric measurements with the presence of H_2O -ice and other materials such as CH_4 , CH_3OH , complex organics and amorphous silicates for objects that present clear signature of those materials in their VNIR spectra (up to $2.0 \mu\text{m}$). Our idea within the following subsections is to focus on the different materials that can be detected using the IRAC colors.

8.1. Water ice

In figure 9 we plotted our sample as a function of the detection of water ice in the VNIR spectra published in the literature (up to $2.0 \mu\text{m}$; e.g., Barucci et al. 2011; Licandro et al. 2001; Lorenzi et al. 2014). Blue stars represent objects for which water detection is already known from the spectra, and were used to test our method (see section 6.2). This includes Sedna and 2002 VE₉₅, for which H_2O has been detected using spectroscopic studies and, as we explained at the end of section 6.2, the presence of CH_3OH move them rightward within the diagram. One object we have not yet discussed is 1996 GQ₂₁ because we only obtained an upper limit at $4.5 \mu\text{m}$ (a more detailed discussion can be found in appendix A). However, this limit constrains the region in which the object is localized within the diagram, eliminating the possibility of having other ices but water.

Objects with tentative detection of water in the VNIR spectra are represented by green triangles. As can be seen, with the exception of 2005 RM₄₃ and 1999 DE₉, all of them fall within regions where H_2O has to be part of the composition. The position of 2005 RM₄₃ in figure 9 is quite interesting, as this region is the one dominated by CO_2 . However, since the errorbars are quite large, we have considered a mixture of organics-silicates-water to obtain a composition, resulting in $50 \pm 40\%$ H_2O -ice, $50 \pm 40\%$ silicates, and no organics. Large amounts of H_2O should be detected by VNIR spectroscopy, which is not the case. The presence of CO_2 in the mixture could be placing the object in that region of the diagram while decreasing the amount of water. Additionally, as we point out in section 8.3, other color-color diagrams support the possibility of this object having CO_2 . On the other hand, the presence of H_2O for 1999 DE₉ has been discussed by several authors with no clear agreement. We conclude that the position of this object within the diagram is not consistent with the presence of H_2O but CH_3OH on its surface (see also Jewitt & Luu 2001). Considering a mixture of H_2O - CH_3OH -organics, the resulting proportion for this object is $20 \pm 10\%$ H_2O , $60 \pm 10\%$ CH_3OH , and $20 \pm 10\%$ organics. These two objects are deeply discussed in section 8.3.

Black circles in figure 9 represent objects for which no H_2O has been reported before. Our results show that 2004 NT₃₃ and the groups formed by 2000 GN₁₇₁, 2002 AW₁₉₇, 2002 UX₂₅, 2004 TY₃₆₄, 2005 RN₄₃, Varda, 2001 UR₁₆₃, and 2004 GV₉ marked by a black rectangle and a pink circle, are consistent with $\sim 20\%$ H_2O -ice within its composition. The resulting proportions for each object are given in table A.

For those objects that have published spectra in the literature, we are able to say that our results are in agreement with the spectra (see appendix A for an indi-

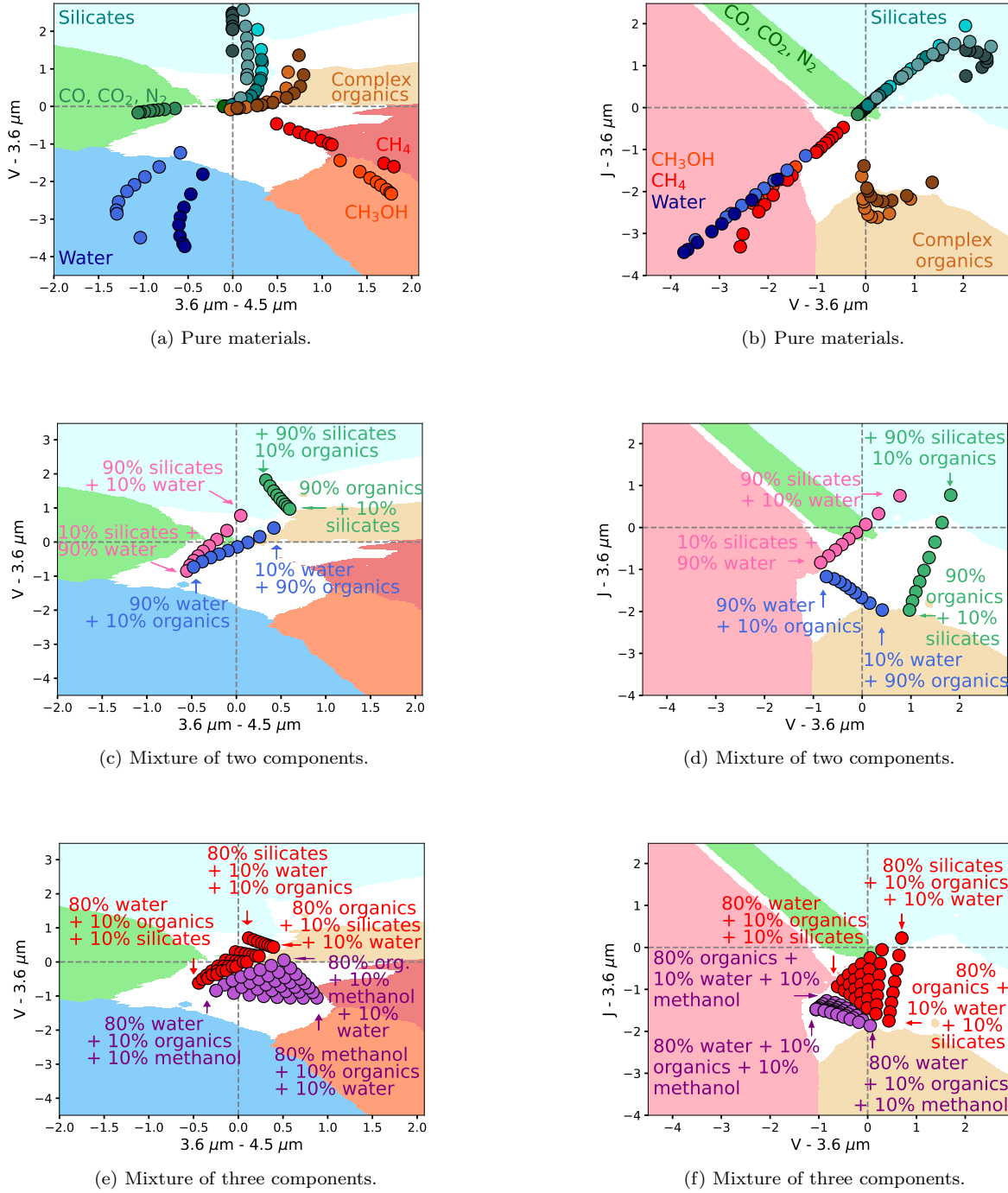


Figure 8. Left panels: $3.6 \mu\text{m} - 4.5 \mu\text{m}$ versus $V - 3.6 \mu\text{m}$ diagrams for pure, mixtures of two components and mixtures of three components (panels a, c, and e, respectively). shaded regions corresponds to a different material as indicated in panel (a) and equivalent to the compositional clock (figure 5). Right panels: $V - 3.6 \mu\text{m}$ versus $J - 3.6 \mu\text{m}$ diagrams for pure, mixtures of two components and mixtures of three components (panels b, d, and f, respectively). In this case, since water, CH_4 , and CH_3OH occupy the same region, the pink shaded region correspond to those three material as indicated in panel (b).

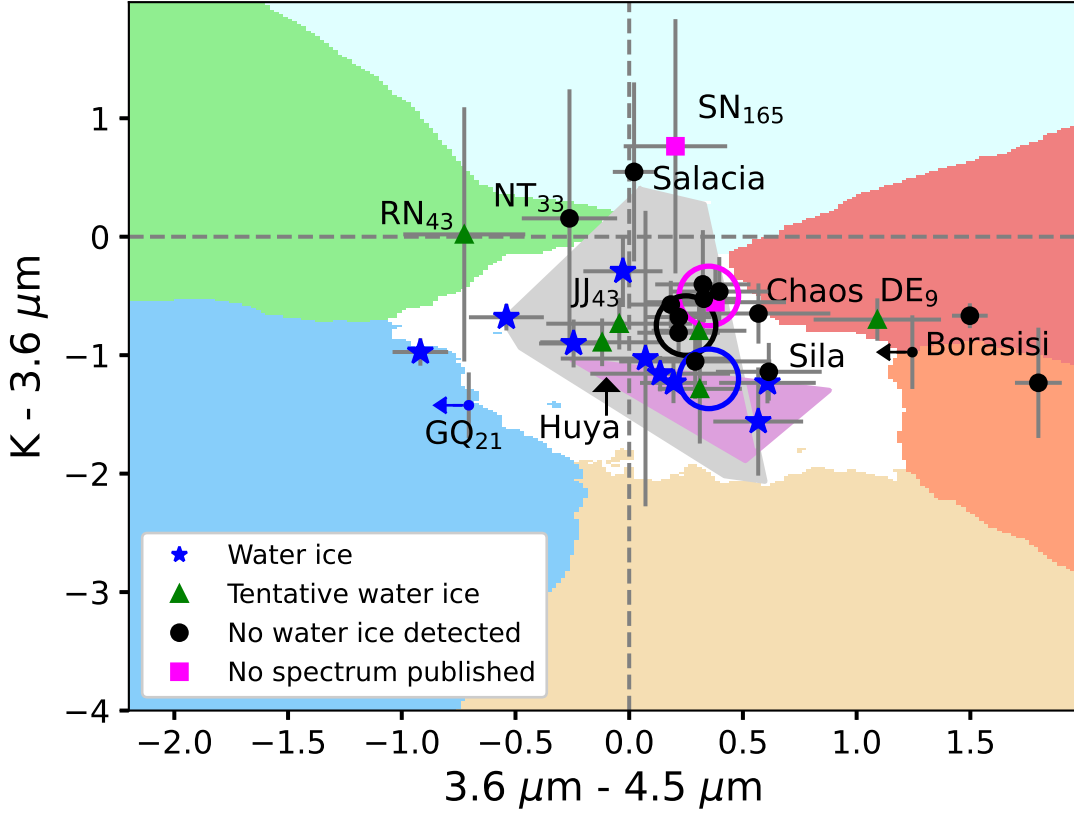


Figure 9. Compositional clock plotting observational data. For comparison between spectroscopic measurements and our results, symbols and colors represent the presence or lack of water detected in spectroscopic data as found in the literature: Blue stars show objects for which water have been identified before using published spectra up to $2\mu\text{m}$. Green triangles represent objects with tentative detection of water ice using published spectra up to $2\mu\text{m}$. Black circles represent objects with no identification of water ice in their published spectra. Pink squares show objects for which no spectra have been published. Pure materials are represented by shaded colored ovals that correspond to figure 5. The shaded regions correspond to pure materials as labeled in figure 7 (a). The white region then is dominated by the combination of all mixture of different proportions, as explained in figures 6 and 7 (b). The grey shaded polygon is representing the binary and ternary models of different proportions of H_2O -silicates-organics plotted in figure 6. The purple triangle is representing models of different proportions of H_2O - CH_3OH -organics. Objects within the black circle are the following: 2002 AW_{197} , 2005 RN_{43} , 2002 UX_{25} , and 2004 TY_{364} (from top to bottom). Objects within the blue circle are: 2000 GN_{171} and 2002 TC_{302} (from top to bottom). Objects within the pink circle are the following: Varda, 2000 PE_{30} , 2001 UR_{163} , and 2004 GV_9 .

vidual explanation on each object). In summary, IRAC colors are highly sensitive to the presence of H_2O , thus using the $3.6\mu\text{m} - 4.5\mu\text{m}$ diagram, with a total of 30 objects (32 if counting the upper limits), 26 objects (86%) present errors bars within 1σ independent probability consistent with the presence of H_2O on their surface, with 22 (73%) representing the 1σ compound probability.

This conclusion is also consistent with the other two color-color diagrams (figure 8). In figure 10, we have plotted the shaded regions corresponding to each pure material (as described in figure 8), with the white region representing binary and trinary mixtures, and the sam-

ple of objects represented by black circles. From panel (a), we obtain that 30 of a total of 37 objects (81%) present errors bars within 1σ independent probability consistent with the presence of H_2O on their surface, with 26 (70%) representing the 1σ compound probability. From panel (b), we obtain that 50 of a total of 59 objects (85%) present errors bars within 1σ independent probability consistent with the presence of H_2O on their surface, with 36 (61%) representing the 1σ compound probability.

8.2. Complex organics

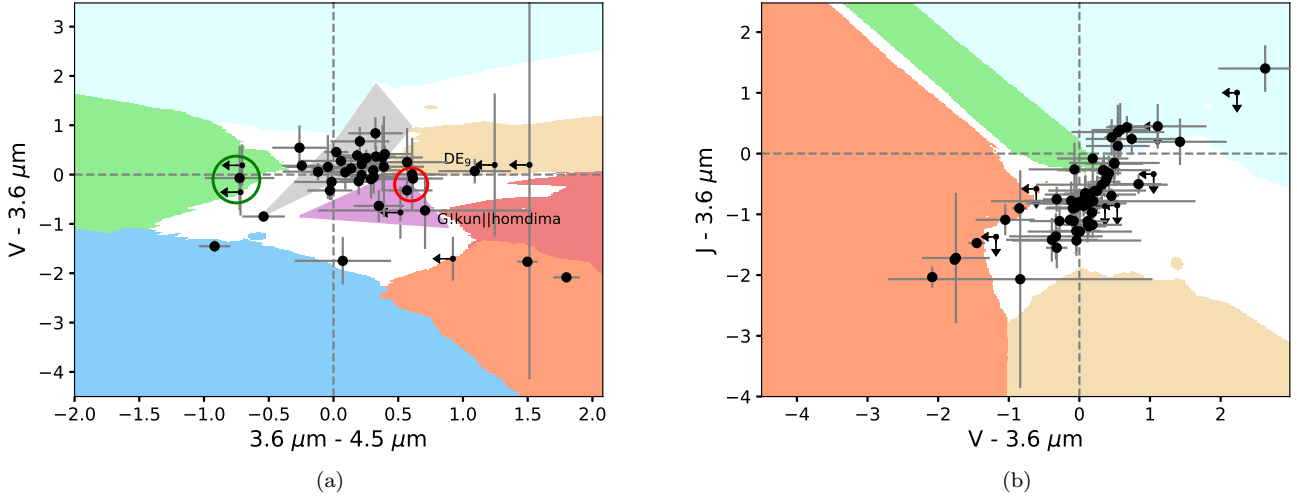


Figure 10. (a) Diagram $3.6 - 4.5 \mu\text{m}$ versus $V - 3.6 \mu\text{m}$, with black points representing our sample. Objects within the red circle are Sedna, Sila-Nunam, and 2002 VE₉₅ (from top to bottom). Objects within the green circle are 1996 GQ₂₁, 2005 RM₄₃, and 2004 PG₁₁₅ (from top to bottom). Shaded regions correspond to different materials as indicated in figure 8 (a) and equivalent to the compositional clock (figure 5). (b) Diagram $V - 3.6 \mu\text{m}$ versus $J - 3.6 \mu\text{m}$. In both diagrams, the shaded regions are the same explained in figure 8. The grey shaded polygon is representing the binary and ternary models of different proportions of H₂O-silicates-organics plotted in figure 6. The purple triangle is representing models of different proportions of H₂O-CH₃OH-organics.

As we have been discussing, one of the potential of IRAC using the compositional clock diagram is that, in order to obtain colors that occupied the center of the diagram, it is required to include complex organics (e.g., tholins) within our models. Tholins have been used for modeling the spectra of different objects but have not been detected before, as they do not produce absorption band at the VNIR spectra. Our method provides a high level of confidence that the surface of most objects within our sample is composed by mixture that include complex organic materials such as tholins (e.g., Khare et al. 1993; Materese et al. 2014, 2015). For instance, in figure 9, we obtain that 80% of the sample present error bars within 1σ independent probability consistent with the presence of organics material on their surface composition with the same percentage (80%) representing the compound probability. From figure 10 (b), we obtain that 90% of the sample present error bars within 1σ independent probability consistent with the presence of organics material on their surface with 63% representing the compound probability. We do not include statistics from figure 10 (a), since both organics and silicates occupy similar regions, and does not provide a clear separation between them. Our preferred statistics are the ones provided by the compositional clock ($K - 3.6 \mu\text{m}$ versus $3.6 \mu\text{m} - 4.5 \mu\text{m}$ diagram), since it is the one that maximize the range difference on colors depending on the material.

Specifically in figure 9, the groups marked by a black rectangle and a pink circle require a percentage between 10 – 60% of complex organics. All of them present an absorption identification at $3.6 \mu\text{m}$ with respect to $4.5 \mu\text{m}$ and an abrupt spectral slope in the visible (see figure 3 and appendix B, with the exception of 200 PE₃₀, which has no spectrum published). Huya, Quaoar, and 2007 JJ₄₃ require between 10 – 40% of complex organics; however, this amount of complex organics might be hidden in their spectra due to the large amount of H₂O-ice, which flattens the spectral slope.

8.3. Supervolatiles, CH₄, and/or CH₃OH

This section is dedicated to the identification of compositions consistent with the presence of supervolatiles, CH₄, and/or CH₃OH. Figure 11 shows our sample highlighting the regions dominated by CH₄, CH₃OH, CO₂, CO and N₂, and mixtures that contain these components. Turquoise stars show objects with detection of both, CH₄ and N₂, as found in the literature from VNIR spectra. The two objects, Sedna and Eris, with this composition were discussed in section 6.2 where we explained the good agreement between the results from spectra and ours. Red triangles represent those objects for which CH₄ has been detected from their spectra. As discussed in section 6.2, Makemake and Eris, both have detection of methane with grain sizes over 0.4 mm in their spectra and appear in a region not only dominated

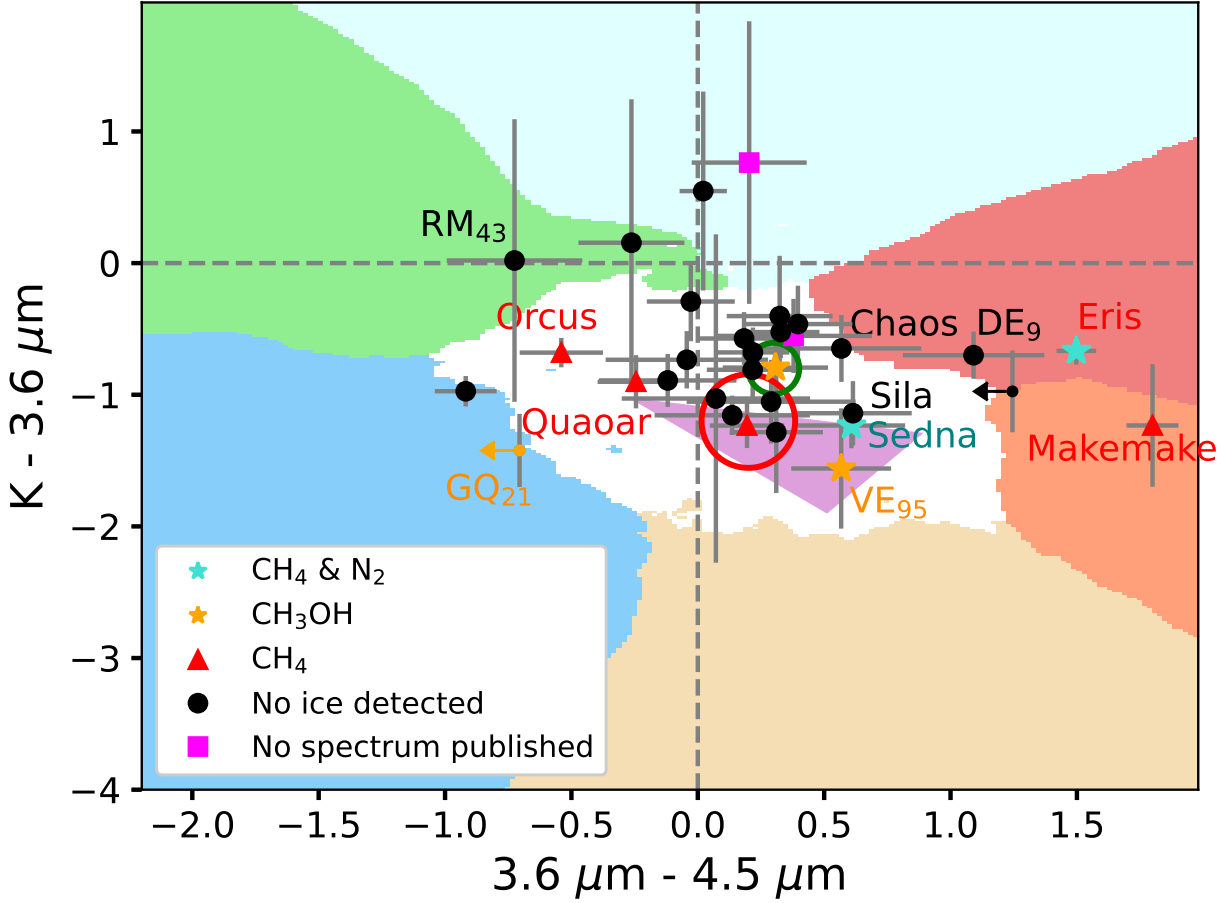


Figure 11. Compositional clock with the sample highlighting objects for which bands related to ices have been identified in spectroscopic measurements up to $2.3 \mu\text{m}$. Turquoise stars depict objects that have CH_4 and, N_2 in their spectra. Orange stars represent objects with possible detection of CH_3OH . Red triangles represent objects with CH_4 detections. Black circles represent objects with no identification of any ice in their spectra. Pink squares show objects for which no spectroscopic data have been published. The orange star surrounded by the green circle is representing 2004 TY_{364} . Objects within the red circle are as follows: 2002 TX_{300} , Lempo, Varuna, 2000 GN_{171} and 2002 TC_{302} (from left to right). The red, orange, and green shaded regions represent the regions of influence of synthetic models of different grain sizes of pure methane, methanol, and supervolatiles (N_2 , CO ,...), respectively. The white region represents the region of influence of synthetic models with different proportions of mixtures of H_2O - CH_4 -organics, and H_2O -silicates-organics. The purple triangle is bounding the theoretical points of different proportions of H_2O - CH_3OH -organics.

by this component but also in which a larger particle size is necessary. The other two objects, Quaoar and Orcus, with CH_4 detection in their spectra are located in a region that seems to contradict this detection. In these specific cases, the large amount of H_2O -ice is hiding the detection of CH_4 using this method, and therefore we do not exclude CH_4 as part of their composition. Additionally for Orcus, its position also suggest the presence of CO_2 which has been suggested by [DeMeo et al. \(2010\)](#).

Objects represented by an orange star are those for which CH_3OH has been tentatively suggested. For 2002 VE_{95} the detection of CH_3OH is in clear agreement

with its position in figure 11. As explained in section 6.2, we obtained a composition that include $40 \pm 20\%$ of complex organics considering a mixture of H_2O - CH_3OH -organics. The position of 2004 TY_{364} is not as clear. Considering models with a mixture of H_2O - CH_3OH -organics, we obtain a proportion of $50 \pm 10\%$, $30 \pm 10\%$, and $20 \pm 10\%$, respectively. However, such amount of water should be noticeable in its spectrum, and that is not the case. On the other hand, considering a mixture of H_2O -silicates-organics, we obtain a proportion of $20 \pm 10\%$, $50 \pm 10\%$, and $35 \pm 10\%$, respectively. The later is more in agreement with its spectra, although

a combination between both mixture would be a very luckily situation. The other two interesting objects in this figure are Sila-Nunam, and 1999 DE₉, whose position is consistent with the presence of CH₄ or CH₃OH. Due to the small size of the binary system (around 300 km; Vilenius et al. 2012; Lellouch et al. 2013), it is unlikely that these objects, Sila and Nunam, possess CH₄ on its surface, being more realistic to think that their position in figure 11 is due to CH₃OH. We obtain a composition of $30 \pm 10\%$ H₂O, $50 \pm 10\%$ CH₃OH, and $20 \pm 10\%$ organics for Sila-Nunam and $20 \pm 10\%$ H₂O, $60 \pm 10\%$ CH₃OH, and $20 \pm 10\%$ organics for 1999 DE₉. A more detailed explanation is given in appendix A.

A composition including CH₄ and CH₃OH on the surfaces of Sedna and 2002 VE₉₅, respectively, is consistent also with their position in figure 10 (a), as explained in section 6.2.

There are three objects (Lempo, 2000 GN₁₇₁, and 2002 TC₃₀₂) depicted by black points within the red circle that are very close or within the purple triangle, for which their position could indicate the presence of CH₃OH. However, for them to have CH₃OH and be located on that region, they would also require a high percentage of H₂O which should have been detected on their spectra. Specific proportions for each of them are given in appendix A. On the contrary, the object 2002 TX₃₀₀, which is right next to the red circle, is known for having large amounts of water on its surface (Licandro et al. 2006a). Considering a mixture of H₂O-CH₃OH-organics, we obtain a composition of $60 \pm 30\%$ H₂O, $20 \pm 10\%$ CH₃OH, and $30 \pm 30\%$ organics. Therefore, the existence of CH₃OH on the surface of 2002 TX₃₀₀ could be displacing this object to the right of the diagram.

Finally, as we mentioned in section 8.1, in figure 11, 2005 RM₄₃ shares the region occupied by CO₂. Although the error bars are large and could place this object out of this region, the diagram $V - 3.6 \mu\text{m}$ versus $J - 3.6 \mu\text{m}$ also support this interpretation (see panel a in figure 10), where there are four objects that share the region occupied by CO₂: 1996 GQ₂₁, 2002 GV₃₁, 2004 PG₁₁₅ and 2005 RM₄₃. Although three of these objects have measurements with only upper limits in the $3.6 \mu\text{m} - 4.5 \mu\text{m}$ color, these limits constrain the objects to regions dominated by supervolatiles (CO₂, CO, N₂) and/or water. On the other hand, the error bars for the $V - 3.6 \mu\text{m}$ color constrain the region to one dominated by the supervolatiles. Our measurements suggest the possibility of these objects containing CO₂ and H₂O. A more detailed explanation and specific proportions considering a mixture of H₂O, silicates and organics are given in appendix A.

Summarizing, seven of 30 objects within the compositional clock (Eris, Makemake, Sila-Nunam, Sedna, 2002 VE₉₅, 2004 TY₃₆₄, and 2002 TX₃₀₀), 32 including those with upper limits, are consistent with a composition that includes CH₃OH and/or CH₄ on their surfaces. Considering other color-color diagrams (figure 10) a total of four objects are consistent with a composition that includes CO₂.

8.4. Silicates

In the compositional clock, the region dominated by the amorphous silicates (see figure 9) is occupied by two objects: Salacia and 1998 SN₁₅₈. Salacia was discussed in section 6.2, for which we conclude a surface clearly dominated by silicates. 1998 SN₁₆₅'s measurements are also consistent with a surface dominated by amorphous silicates. We obtain a proportion of $90 \pm 20\%$ silicates, and $10 \pm 10\%$ H₂O, and no organics.

In this regard, we also found interesting information representing the $V - 3.6 \mu\text{m}$ versus $J - 3.6 \mu\text{m}$ diagram when dividing the sample between small objects (those with diameters, D , smaller than 400 km) and large objects (those with $D > 400$ km, see figure 12). In this specific diagram, where there is a total of 28 objects over 400 km, only one object presents 1σ probability of having $J - 3.6 \mu\text{m} > 0$, or, in other words, being dominated by silicates (namely, Salacia, which has a diameter of ~ 900 km; Fornasier et al. 2013). This translates into a 4% probability of an object over 400 km presenting $J - 3.6 \mu\text{m} > 0$. While there are 6 objects with $D < 400$ km (from a total of 38) with colors consistent with a surface dominated by silicates: 2000 GP₁₈₃, 2000 QL₂₅₁, 2001 CZ₃₁, 2001 QJ₁₈₁, 2002 CY₂₂₄, and 2004 EW₉₅. For all of them, we obtain over 80% of silicates on its surface, considering a mixture of H₂O, silicates and organics (see detailed information in appendix A). In fact, the spectrum of 2004 EW₉₅ was studied by Seccull et al. (2018). They demonstrated that its composition is “consistent” with a C-type asteroid and the spectrum present a clear feature produced by hydrated, iron-rich silicates. This result provides validity for these specific colors to indicate surface consistence with compositions dominated by silicates.

9. DIAGRAMS BY DWARF PLANETS AND HAUMEA'S FAMILY

However, Panel (a) in figure 13 shows the $V - 3.6 \mu\text{m}$ versus $3.6 - 4.5 \mu\text{m}$ diagram and indicates whether the objects are dwarf planets, Haumea family members, or neither of these two classifications. This diagram reveals that dwarf planets and Haumea family members (confirmed through dynamical models and spectroscopic measure-

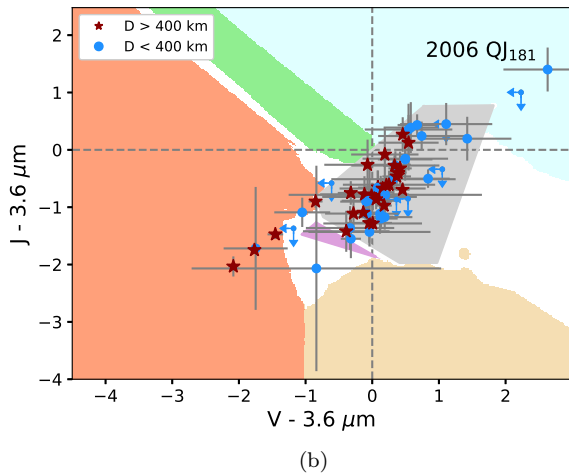


Figure 12. Diagram $V - 3.6 \mu\text{m}$ versus $J - 3.6 \mu\text{m}$ as a function of the size. Objects with diameters smaller than 400 km are represented by brown circles, while objects larger than 400 km are represented by red stars. Shaded regions are equivalent to those in figure 10 (b).

ments; Brown et al. 2007b; Snodgrass et al. 2010) appear segregated from the rest of the TNO population (including those non-Haumea family members that show H_2O), in regions dominated by H_2O , CH_4 or CH_3OH and in agreement with the previous knowledge about their composition.

In panel (b) of figure 13, these objects appear again in a detached region from the rest of the sample. The dwarf planets, Makemake, Eris and Haumea and 2002 TX₃₀₀ are clearly located over the region dominated by pure CH_4 or H_2O materials. The location of 1995 SM₅₅ is not as clear, however, it is detached from the rest of the population. Measurements for 2005 RR₄₃ and 1996 TO₆₆ are upper limits in both axes; however, these limits constrain the surface composition to models with high percentage of water, in agreement with their published spectra (Brown et al. 1999; Pinilla-Alonso et al. 2007; Barucci et al. 2011).

Due to the lack of measurements for Haumea family members either at infrared wavelength or at $4.5 \mu\text{m}$, we are not able to use the diagram $K - 3.6 \mu\text{m}$ vs $3.6 - 4.5 \mu\text{m}$ (Haumea and 2002 TX₃₀₀ are the only two objects within the family that provide such a combination of measurements).

New observations of objects that have been dynamically identified as part of the family could be also “spectroscopically” confirmed if they fall in the same region of both diagrams.

10. DIAGRAMS BY TAXONOMIC CLASSIFICATIONS

The paucity of spectroscopic data compelled different authors to establish taxonomic classes in order to interpret the different surfaces found in the trans-Neptunian region. Two different taxonomies can be found in the literature. One was first proposed by Barucci et al. (2005b), who proposed four different taxonomic groups: neutral objects (BB), two intermediate slightly red types (BR and IR), and the reddest objects (RR). This taxonomy was updated more recently by Belskaya et al. (2015), where the BB taxonomic group was divided between objects with high and low albedo (BBb and BB, respectively). The other system, first proposed by Fraser & Brown (2012) and developed in Lacerda et al. (2014) presented a different perspective, in which two main classes are defined: the red one includes objects with higher albedos and redder colors, and the blue one includes objects with lower albedos and less red colors. Furthermore, Lacerda et al. (2014) proposed two other groups within the latter taxonomy classification in order to distinguish between dwarf planets and Haumea’s family. The taxonomy proposed by Fraser & Brown (2012) is also discussed in Schwamb et al. (2019).

The most interesting diagrams to plot by taxonomy are the compositional clock ($3.6 \mu\text{m} - 4.5 \mu\text{m}$ versus $K - 3.6 \mu\text{m}$), and the $V - 3.6 \mu\text{m}$ versus $J - 3.6 \mu\text{m}$ diagrams (figure 14). In both cases, we see how blue (Lacerda et al. 2014) and neutral (Belskaya et al. 2015) objects, depending on the reference, fall within regions where our models indicate the presence of high percentages of water and/or silicates, which have generally more neutral spectroscopic slopes. In contrast, redder objects are found in regions where models indicate the presence of organic materials, which have redder spectral slopes. In panels (c) and (d) figure 14, we can also highlight the group of objects that are distinct from the rest of TNOs due to their extremely high albedo. This group can be seen where models with pure water, CH_4 , and CH_3OH are located, which have the common characteristic of presenting high albedos.

We want to emphasize that our data can generate a compositional context for the different taxonomic classifications. For instance, IR objects are consistent with having a mixture of similar proportions of silicates and complex organics and having non-zero H_2O . Also, most RR (Belskaya et al. 2015) and red (Lacerda et al. 2014) objects are consistent with being composed of material with smaller proportions of silicates and both rich in organics, and having a non-zero H_2O -ice content. While the latter was known for part of our sample from VNIR spectroscopy, the former was only inferred due to their

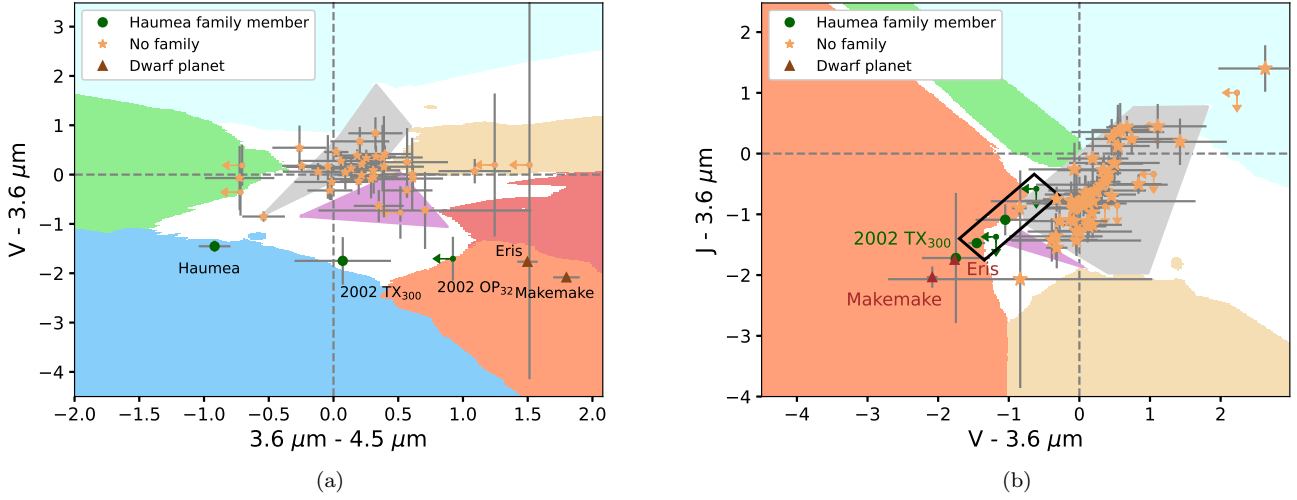


Figure 13. (a) Diagram $3.6 - 4.5 \mu\text{m}$ versus $V - 3.6 \mu\text{m}$. (b) $V - 3.6 \mu\text{m}$ versus $J - 3.6 \mu\text{m}$. In both panels, we represented the sample as a function of Haumea’s family members and dwarf planets (confirmed through dynamical models and spectroscopic measurements; [Brown et al. 2007b](#); [Snodgrass et al. 2010](#)) and dwarf planets. Objects within the black rectangle are as follows: Haumea, 2005 RR₄₃, 1995 SM₅₅, Orcus, and 1996 TO₆₆ (from left to right). In both panels, shaded regions are equivalent to those explained in figure 10.

red colors. Our measurements provide a high level of confidence that this red visible color is imparted by organic materials such as tholins (e.g., [Khare et al. 1993](#); [Materese et al. 2014, 2015](#)), which produce absorption bands beyond $2.2 \mu\text{m}$.

11. DIAGRAMS BY DYNAMICAL CLASSES

As mentioned in section 1, one might expect that different dynamical classes could experience different physical processes due to different past and present environments and therefore, exhibit at least slightly different surface composition. As expected, figure 15 shows that there is no distinction between detached, resonant and hot classical objects.

In particular, all of our inner classical belt objects fall firmly in with the majority of TNOs, even the low- i inner belt objects. This fact thus adds additional support to the hypothesis based on orbital dynamics ([Kavelaars et al. 2009](#); [Petit et al. 2011](#)) that the inner belt classical ($a < 39.4$ au classical objects) TNOs are entirely a captured hot population, and the low- i members are just the low-inclination tail of the hot distribution. This hypothesis was confirmed in optical colours by [Tegler et al. \(2016\)](#) and we extend this into the infrared. Thus, the cold classical population appears not to exist today for $a < 42.5$ au where it begins (between 39.4 and 42.5 au the ν_8 secular resonance rapidly removes all low- i TNOs).

It is highly desirable to examine the IR features of the cold classical population, as this population is

thought to have formed and remain in the same location throughout their life-time ([Kavelaars et al. 2009](#); [Parker & Kavelaars 2010](#)); it is thus a probe of the formation conditions at this distance ([Petit et al. 2011](#)). If any TNO population region should look spectrally distinct, this is the population to study. Unfortunately, we only have measurements for four cold classical objects, from which only three have colors to be represented in our diagrams. However, we can provide some limited statements. Panel (a) in figure 15 provides colors for one cold classical (Sila-Nunam) and an upper limit in the color $3.6 \mu\text{m} - 4.5 \mu\text{m}$ for another object (Borasisi). Panel (b) provides colors for Sila-Nunam and an upper limits in the color $3.6 \mu\text{m} - 4.5 \mu\text{m}$ for two objects (Borasisi and 1996 TK₆₆). In these two panels, all cold classical objects appear within the same region, however, note that only Sila-Nunam provides measured colors, as the other two only have $4.6 \mu\text{m}$ upper limits. Panel (c) provide colors for Sila-Nunam and Borasisi and upper limits in both colors for 1996 TK₆₆. In this panel, both objects with colors are located close to each other, and only the one with upper limits is in a region detached from them. Furthermore, agreement appears to exist between all the diagrams regarding the interpretation of the composition of those objects, namely, the colors are consistent with the existence of CH_3OH on their surfaces. This is especially true in the case of Sila-Nunam, which has accurate measurements in the three diagrams. This strongly motivates future work to obtain IR colours

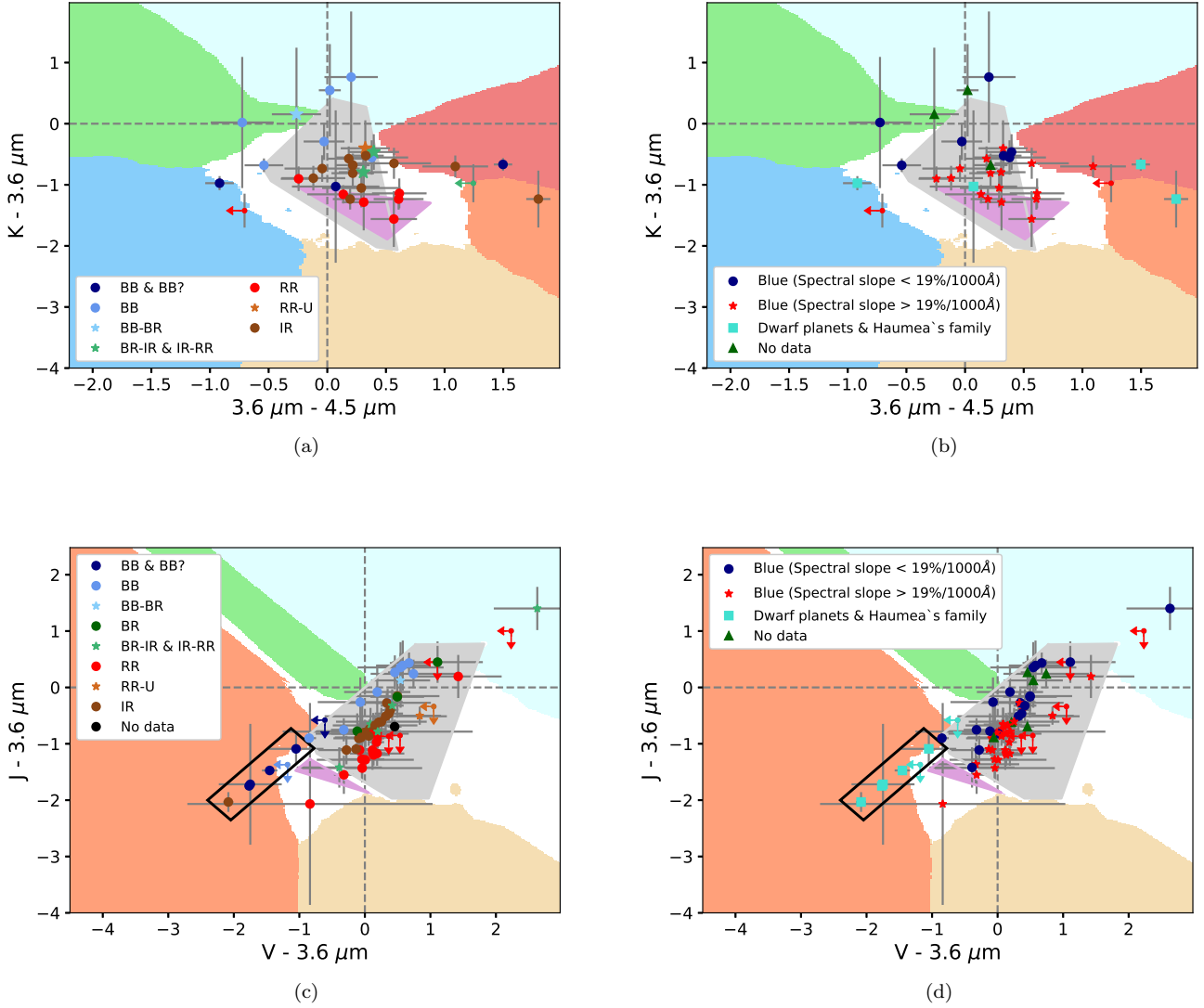


Figure 14. Upper panels: Compositional clock as a function of taxonomic classifications. (a) Taxonomy developed by Barucci et al. (2005a) and Belskaya et al. (2015). (b) Taxonomy developed by Fraser & Brown (2012) and Lacerda et al. (2014). **Bottom pannels:** $V - 3.6 \mu\text{m}$ versus $J - 3.6 \mu\text{m}$ diagrams as a function of taxonomy classifications. (c) Taxonomy developed by Barucci et al. (2005a) and Belskaya et al. (2015). (d) Taxonomy developed by Fraser & Brown (2012) and Lacerda et al. (2014). The group of objects with extremely high albedo claimed by both taxonomic theories are located within the black oval.

for a sample of cold classical objects; we tentatively hypothesize that they will be found to have features related to the existence of CH_3OH on their surfaces and appear distinct from the other TNO populations (with some overlap in some colours with large objects like Eris and MakeMake due to atmospheric physics).

Interestingly, Grundy et al. (2020) show that the spectra of Arrokoth (also a cold classical object), taken by LEISA on board of New Horizons, has clear CH_3OH absorption bands, but do not show convincing evidence for H_2O . As mentioned above, our models are consistent with Sila-Nunam containing CH_3OH . In order

to explain Arrokoth's composition, Grundy et al. (2020) propose that temperatures at the formation location of cold classical objects would have been low enough that volatile CO and CH_4 could freeze onto dust grains in the cold mid-plane of the nebula (where the sunlight was blocked), enabling production of CH_3OH and perhaps also destruction of H_2O . Once the dust and gas are dissipated from the nebula, the CH_4 volatilizes due to the high equilibrium temperature, leaving only CH_3OH . Thus, the cold population should show signatures of CH_3OH on their surfaces, either in spectra or color. It has been shown by different authors that cold classi-

cals are both brighter (a characteristic of CH_3OH on the spectrum), and redder (as the tholin material produced by the irradiation of CH_3OH) than other populations (e.g., Brucker et al. 2009; Vilenius et al. 2014). Grundy et al. (2020)’s hypothesis could be tested with new color measurements of cold classicals, but we will need to wait for JWST to achieve the desired sensitivity at the specific wavelengths in which CH_3OH absorption bands can be detected for such a faint population.

12. CONCLUSIONS

We present a new method to study the surface composition of small solar system bodies. Using VNIR colors, together with specific filters beyond $2.2\ \mu\text{m}$, we have built color-color diagrams in which different materials occupy different regions of the diagram. Using these color-color diagrams, we are able to study very faint objects for which spectroscopic techniques would be either very expensive in time or impossible to carry out. Specifically, the compositional clock can discern compositions that are consistent with mixtures that require small amounts of H_2O and other ices such as CO_2 , CH_4 , CH_3OH . The compositional clock also provides a high degree of confidence for the presence of complex organic materials such as tholins. The diagram $V - 36\ \mu\text{m}$ versus $J - 3.6\ \mu\text{m}$ also support this conclusion. A summary of the compositional interpretation by this method can be found in table 4.

From the compositional clock, we found that most of the TNOs within our sample (73%), which includes detached, resonant and classical objects, have colors consistent with surfaces mainly composed of a mixture of H_2O -ice, complex organics and amorphous silicates. 86% of the sample have signatures consistent with water ice on their surface and 23% have or may have CH_4 and/or CH_3OH . Also, 80% have colors consistent with the presence of complex organics. Using other diagrams, we notice that only smaller objects seem to have colors that indicate surfaces dominated by silicates. In agreement with other authors, we also noticed that

Haumea’s family members and dwarf planets have a peculiar composition when compared with other TNOs. We are not able to distinguish very clearly between CH_4 and CH_3OH using the compositional clock or the other diagrams. Observations with specific/narrower filters should be carried out in order to be able to distinguish between these two components (as IRAC filters are very wide passbands).

There is currently a lack of measurements for cold classical and detached objects at $4.5\ \mu\text{m}$ due to the faintness of these specific classes. In this regard, JWST will be advantageous for observing these objects. JWST will have a set of filters specifically for the detection of the different materials discussed in this work (figure 4), see Kalirai (2018). Thus, JWST will enable similar studies with much fainter objects and will provide additional filters for more specific detections. This capability will be extremely useful to constrain the surface composition of objects within the trans-Neptunian region.

ACKNOWLEDGEMENTS

E. Fernández-Valenzuela acknowledges support from the 2017 Preeminent Postdoctoral Program (P^3) at UCF and the “Earth and Space Based Studies in Support of NASA Space Missions” under the Space Research Initiative (SRI) Program at FSI. BG and CvL acknowledge funding support from NSERC. N. P.-A. acknowledges funding support from the Spitzer Space Telescope, operated by the Jet Propulsion Laboratory, California and from the SRI/FSI project “Digging-up Ice Rocks In The Solar System”. TM has received funding from the European Union Horizon 2020 Research and Innovation Programme, under Grant Agreement no 687378, as part of the project “Small Bodies Near and Far” (SBNF). This work is based on observations made with the Spitzer Space Telescope, which is operated by the Jet Propulsion Laboratory, California Institute of Technology under a contract with NASA. Support for this work was provided by NASA. We acknowledge Raúl Carballo-Rubio and the anonymous referees for providing useful comments that helped improve this manuscript.

REFERENCES

- Alvarez-Candal, A., Barucci, M. A., Merlin, F., Guilbert, A., & de Bergh, C. 2007, *A&A*, 475, 369, doi: [10.1051/0004-6361:20078123](https://doi.org/10.1051/0004-6361:20078123)
- Alvarez-Candal, A., Pinilla-Alonso, N., Ortiz, J. L., et al. 2016, *A&A*, 586, A155, doi: [10.1051/0004-6361/201527161](https://doi.org/10.1051/0004-6361/201527161)
- Alvarez-Candal, A., Pinilla-Alonso, N., Licandro, J., et al. 2011, *A&A*, 532, A130, doi: [10.1051/0004-6361/201117069](https://doi.org/10.1051/0004-6361/201117069)
- Barkume, K. M., Brown, M. E., & Schaller, E. L. 2008, *AJ*, 135, 55, doi: [10.1088/0004-6256/135/1/55](https://doi.org/10.1088/0004-6256/135/1/55)
- Barucci, M. A., Alvarez-Candal, A., Merlin, F., et al. 2011, *Icarus*, 214, 297, doi: [10.1016/j.icarus.2011.04.019](https://doi.org/10.1016/j.icarus.2011.04.019)

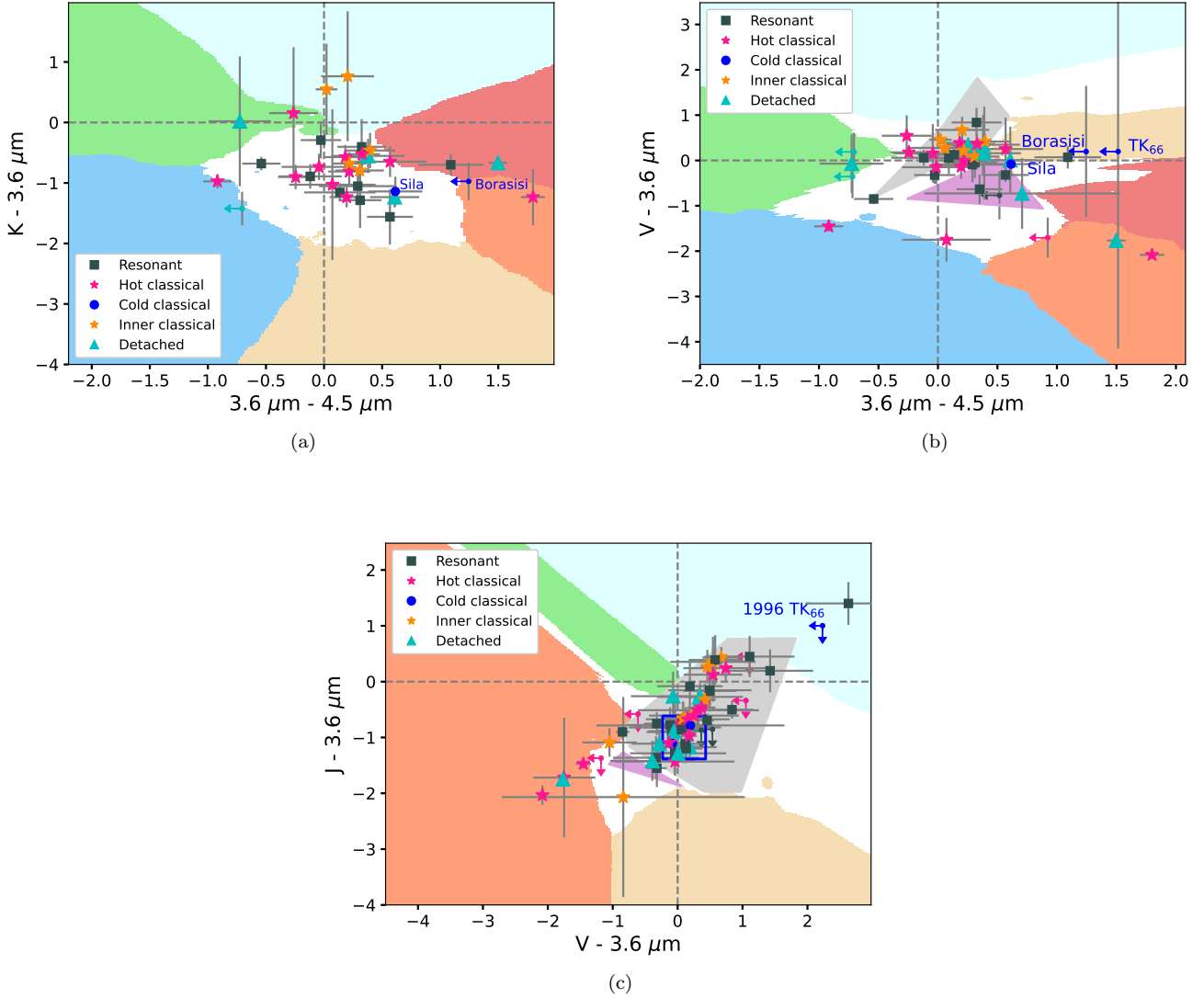


Figure 15. Compositional clock as a function of dynamical classes. Green squares depict resonant objects, turquoise triangles depict detached objects, pink stars depict hot classical objects and blue circles depict cold classical objects. Asterisks represent objects for which $3.6 - 4.5 \mu\text{m}$ color is an upper limit, and the asterisks color is matched to the dynamical class. (c) The blue square has been plotted to show the position of Borasisi and Sila-Nunam, which are the right and left blue circles within the square, respectively.

Barucci, M. A., Belskaya, I. N., Fulchignoni, M., & Birlan, M. 2005a, *AJ*, 130, 1291, doi: [10.1086/431957](https://doi.org/10.1086/431957)

Barucci, M. A., Cruikshank, D. P., Dotto, E., et al. 2005b, *A&A*, 439, L1, doi: [10.1051/0004-6361:200500144](https://doi.org/10.1051/0004-6361:200500144)

Barucci, M. A., Doressoundiram, A., Tholen, D., Fulchignoni, M., & Lazzarin, M. 1999, *Icarus*, 142, 476, doi: [10.1006/icar.1999.6212](https://doi.org/10.1006/icar.1999.6212)

Barucci, M. A., & Merlin, F. 2020, *Surface composition of Trans-Neptunian objects*, ed. D. Pralnik, M. A. Barucci, & L. Young, 109–126, doi: [10.1016/B978-0-12-816490-7.00005-9](https://doi.org/10.1016/B978-0-12-816490-7.00005-9)

Barucci, M. A., Merlin, F., Dotto, E., Doressoundiram, A., & de Bergh, C. 2006, *A&A*, 455, 725, doi: [10.1051/0004-6361:20064951](https://doi.org/10.1051/0004-6361:20064951)

Barucci, M. A., Merlin, F., Guilbert, A., et al. 2008, *A&A*, 479, L13, doi: [10.1051/0004-6361:20079079](https://doi.org/10.1051/0004-6361:20079079)

Belskaya, I. N., Barucci, M. A., Fulchignoni, M., & Dvognopol, A. N. 2015, *Icarus*, 250, 482, doi: [10.1016/j.icarus.2014.12.004](https://doi.org/10.1016/j.icarus.2014.12.004)

Bessell, M. S. 2005, *RA&A*, 43, 293, doi: [10.1146/annurev.astro.41.082801.100251](https://doi.org/10.1146/annurev.astro.41.082801.100251)

Table 4. Summary of the different compositions found using the color-color diagrams and taking into account the spectra published in the literature, as described in this work. Statistics are given according to the compositional clock.

Composition	Objects
Dominated by H ₂ O > 50% of H ₂ O Dominated by CH ₄ Dominated by silicates Presence of CH ₃ OH and/or CH ₄	Haumea Quaoar, Orcus Eris, Makemake Salacia, 1998 SN ₁₆₅ Sedna, Sila-Nunam, 1999 DE ₉ , 2002 VE ₉₅ , 2002 TX ₃₀₂ .
86% of the sample presents colors consistent with the presence of H ₂ O-ice 80% of the sample presents colors consistent with the presence of complex organics 93% of the sample presents colors consistent with the presence of amorphous silicates 23% of the objects in our sample has or may has CH ₄ and/or CH ₃ OH Only smaller objects are dominated by silicates	

- Bessell, M. S., & Brett, J. M. 1988, *PASP*, 100, 1134, doi: [10.1086/132281](https://doi.org/10.1086/132281)
- Boehnhardt, H., Tozzi, G. P., Birkle, K., et al. 2001, *A&A*, 378, 653, doi: [10.1051/0004-6361:20011212](https://doi.org/10.1051/0004-6361:20011212)
- Boehnhardt, H., Delsanti, A., Barucci, A., et al. 2002, *A&A*, 395, 297, doi: [10.1051/0004-6361:20021265](https://doi.org/10.1051/0004-6361:20021265)
- Brown, M. E. 2001, *AJ*, 121, 2804, doi: [10.1086/320391](https://doi.org/10.1086/320391)
- . 2008, *The Largest Kuiper Belt Objects*, ed. M. A. Barucci, H. Boehnhardt, D. P. Cruikshank, A. Morbidelli, & R. Dotson, 335
- Brown, M. E., Barkume, K. M., Blake, G. A., et al. 2007a, *AJ*, 133, 284, doi: [10.1086/509734](https://doi.org/10.1086/509734)
- Brown, M. E., Barkume, K. M., Ragozzine, D., & Schaller, E. L. 2007b, *Nature*, 446, 294, doi: [10.1038/nature05619](https://doi.org/10.1038/nature05619)
- Brown, R. H., Cruikshank, D. P., & Pendleton, Y. 1999, *ApJ*, 519, L101, doi: [10.1086/312098](https://doi.org/10.1086/312098)
- Brucker, M. J., Grundy, W. M., Stansberry, J. A., et al. 2009, *Icarus*, 201, 284, doi: [10.1016/j.icarus.2008.12.040](https://doi.org/10.1016/j.icarus.2008.12.040)
- Cruikshank, D. P., Imanaka, H., & Dalle Ore, C. M. 2005, *Advances in Space Research*, 36, 178, doi: [10.1016/j.asr.2005.07.026](https://doi.org/10.1016/j.asr.2005.07.026)
- Cruikshank, D. P., Roush, T. L., Bartholomew, M. J., et al. 1998, *Icarus*, 135, 389, doi: [10.1006/icar.1998.5997](https://doi.org/10.1006/icar.1998.5997)
- Dalle Ore, C. M., Barucci, M. A., Emery, J. P., et al. 2009, *A&A*, 501, 349, doi: [10.1051/0004-6361/200911752](https://doi.org/10.1051/0004-6361/200911752)
- de Bergh, C., Delsanti, A., Tozzi, G. P., et al. 2005, *A&A*, 437, 1115, doi: [10.1051/0004-6361:20042533](https://doi.org/10.1051/0004-6361:20042533)
- de Bergh, C., Boehnhardt, H., Barucci, M. A., et al. 2004, *A&A*, 416, 791, doi: [10.1051/0004-6361:20031727](https://doi.org/10.1051/0004-6361:20031727)
- Delsanti, A., Hainaut, O., Jourdeuil, E., et al. 2004, *A&A*, 417, 1145, doi: [10.1051/0004-6361:20034182](https://doi.org/10.1051/0004-6361:20034182)
- Delsanti, A., Merlin, F., Guilbert-Lepoutre, A., et al. 2010, *A&A*, 520, A40, doi: [10.1051/0004-6361/201014296](https://doi.org/10.1051/0004-6361/201014296)
- Delsanti, A., Peixinho, N., Boehnhardt, H., et al. 2006, *AJ*, 131, 1851, doi: [10.1086/499402](https://doi.org/10.1086/499402)
- Delsanti, A. C., Boehnhardt, H., Barrera, L., et al. 2001, *A&A*, 380, 347, doi: [10.1051/0004-6361:20011432](https://doi.org/10.1051/0004-6361:20011432)
- DeMeo, F. E., Barucci, M. A., Merlin, F., et al. 2010, *A&A*, 521, A35, doi: [10.1051/0004-6361/201014042](https://doi.org/10.1051/0004-6361/201014042)
- DeMeo, F. E., Fornasier, S., Barucci, M. A., et al. 2009, *A&A*, 493, 283, doi: [10.1051/0004-6361:200810561](https://doi.org/10.1051/0004-6361:200810561)
- Doressoundiram, A., Barucci, M. A., Romon, J., & Veillet, C. 2001, *Icarus*, 154, 277, doi: [10.1006/icar.2001.6724](https://doi.org/10.1006/icar.2001.6724)
- Doressoundiram, A., Boehnhardt, H., Tegler, S. C., & Trujillo, C. 2008, *Color Properties and Trends of the Transneptunian Objects*, ed. M. A. Barucci, H. Boehnhardt, D. P. Cruikshank, A. Morbidelli, & R. Dotson, 91–104
- Doressoundiram, A., Peixinho, N., de Bergh, C., et al. 2002, *AJ*, 124, 2279, doi: [10.1086/342447](https://doi.org/10.1086/342447)
- Doressoundiram, A., Peixinho, N., Doucet, C., et al. 2005, *Icarus*, 174, 90, doi: [10.1016/j.icarus.2004.09.009](https://doi.org/10.1016/j.icarus.2004.09.009)
- Doressoundiram, A., Peixinho, N., Moullet, A., et al. 2007, *AJ*, 134, 2186, doi: [10.1086/522783](https://doi.org/10.1086/522783)
- Doressoundiram, A., Tozzi, G. P., Barucci, M. A., et al. 2003, *AJ*, 125, 2721, doi: [10.1086/374632](https://doi.org/10.1086/374632)
- Dorschner, J., Begemann, B., Henning, T., Jaeger, C., & Mutschke, H. 1995, *A&A*, 300, 503
- Dotto, E., Barucci, M. A., Boehnhardt, H., et al. 2003, *Icarus*, 162, 408, doi: [10.1016/S0019-1035\(03\)00023-X](https://doi.org/10.1016/S0019-1035(03)00023-X)
- Emery, J. P., & Brown, R. H. 2004, *Icarus*, 170, 131, doi: [10.1016/j.icarus.2004.02.004](https://doi.org/10.1016/j.icarus.2004.02.004)
- Emery, J. P., Dalle Ore, C. M., Cruikshank, D. P., et al. 2007, *A&A*, 466, 395, doi: [10.1051/0004-6361:20067021](https://doi.org/10.1051/0004-6361:20067021)
- Fazio, G. G., Hora, J. L., Allen, L. E., et al. 2004, *ApJS*, 154, 10, doi: [10.1086/422843](https://doi.org/10.1086/422843)
- Fernández, J. 2020, *The Trans-Neptunian Solar System*, 1, doi: [10.1016/B978-0-12-816490-7.00001-1](https://doi.org/10.1016/B978-0-12-816490-7.00001-1)
- Fernandez, J. A. 1980, *MNRAS*, 192, 481, doi: [10.1093/mnras/192.3.481](https://doi.org/10.1093/mnras/192.3.481)

- Fornasier, S., Dotto, E., Barucci, M. A., & Barbieri, C. 2004a, *A&A*, 422, L43, doi: [10.1051/0004-6361:20048004](https://doi.org/10.1051/0004-6361:20048004)
- Fornasier, S., Doressoundiram, A., Tozzi, G. P., et al. 2004b, *A&A*, 421, 353, doi: [10.1051/0004-6361:20041221](https://doi.org/10.1051/0004-6361:20041221)
- Fornasier, S., Barucci, M. A., de Bergh, C., et al. 2009, *A&A*, 508, 457, doi: [10.1051/0004-6361/200912582](https://doi.org/10.1051/0004-6361/200912582)
- Fornasier, S., Lellouch, E., Müller, T., et al. 2013, *A&A*, 555, A15, doi: [10.1051/0004-6361/201321329](https://doi.org/10.1051/0004-6361/201321329)
- Fraser, W. C., & Brown, M. E. 2012, *ApJ*, 749, 33, doi: [10.1088/0004-637X/749/1/33](https://doi.org/10.1088/0004-637X/749/1/33)
- Fraser, W. C., Brown, M. E., & Glass, F. 2015, *ApJ*, 804, 31, doi: [10.1088/0004-637X/804/1/31](https://doi.org/10.1088/0004-637X/804/1/31)
- Fulchignoni, M., Belskaya, I., Barucci, M. A., de Sanctis, M. C., & Doressoundiram, A. 2008, *Transneptunian Object Taxonomy*, ed. M. A. Barucci, H. Boehnhardt, D. P. Cruikshank, A. Morbidelli, & R. Dotson, 181–192
- Gil-Hutton, R. 2002, *P&SS*, 50, 57, doi: [10.1016/S0032-0633\(01\)00073-3](https://doi.org/10.1016/S0032-0633(01)00073-3)
- Gladman, B., Marsden, B. G., & Vanlaerhoven, C. 2008, *Nomenclature in the Outer Solar System*, ed. M. A. Barucci, H. Boehnhardt, D. P. Cruikshank, A. Morbidelli, & R. Dotson, 43–57
- Gourgeot, F., Barucci, M. A., Alvarez-Candal, A., et al. 2015, *A&A*, 582, A13, doi: [10.1051/0004-6361/201526014](https://doi.org/10.1051/0004-6361/201526014)
- Grundy, W. M., Buie, M. W., & Spencer, J. R. 2005, *AJ*, 130, 1299, doi: [10.1086/431958](https://doi.org/10.1086/431958)
- Grundy, W. M., Schmitt, B., & Quirico, E. 2002, *Icarus*, 155, 486, doi: [10.1006/icar.2001.6726](https://doi.org/10.1006/icar.2001.6726)
- Grundy, W. M., Bird, M. K., Britt, D. T., et al. 2020, *Science*, 367, aay3705, doi: [10.1126/science.aay3705](https://doi.org/10.1126/science.aay3705)
- Guilbert, A., Alvarez-Candal, A., Merlin, F., et al. 2009, *Icarus*, 201, 272, doi: [10.1016/j.icarus.2008.12.023](https://doi.org/10.1016/j.icarus.2008.12.023)
- Hainaut, O. R., Boehnhardt, H., & Protopapa, S. 2012, *A&A*, 546, A115, doi: [10.1051/0004-6361/201219566](https://doi.org/10.1051/0004-6361/201219566)
- Hansen, G. B. 1997, *JGR*, 102, 21569, doi: [10.1029/97JE01875](https://doi.org/10.1029/97JE01875)
- Hapke, B. 1993, *Theory of reflectance and emittance spectroscopy*
- Hapke, B., & Wells, E. 1981, *J. Geophys. Res.*, 86, 3055, doi: [10.1029/JB086iB04p03055](https://doi.org/10.1029/JB086iB04p03055)
- Hastie, T., Tibshirani, R., & Friedman, J. 2001, *The Elements of Statistical Learning*, Springer Series in Statistics (New York, NY, USA: Springer New York Inc.)
- Imanaka, H., Cruikshank, D. P., Khare, B. N., & McKay, C. P. 2012, *Icarus*, 218, 247, doi: [10.1016/j.icarus.2011.11.018](https://doi.org/10.1016/j.icarus.2011.11.018)
- James, G., Witten, D., Hastie, T., & Tibshirani, R. 2013, *An Introduction to Statistical Learning: with Applications in R* (Springer). <https://faculty.marshall.usc.edu/gareth-james/ISL/>
- Jewitt, D. C., & Luu, J. 2004, *Nature*, 432, 731, doi: [10.1038/nature03111](https://doi.org/10.1038/nature03111)
- Jewitt, D. C., & Luu, J. X. 2001, *AJ*, 122, 2099, doi: [10.1086/323304](https://doi.org/10.1086/323304)
- Johnson, H. L. 1964, *Photoelectric Photometers and Amplifiers*, ed. W. A. Hiltner, 157
- Kalirai, J. 2018, *Contemporary Physics*, 59, 251, doi: [10.1080/00107514.2018.1467648](https://doi.org/10.1080/00107514.2018.1467648)
- Kavelaars, J. J., Jones, R. L., Gladman, B. J., et al. 2009, *AJ*, 137, 4917, doi: [10.1088/0004-6256/137/6/4917](https://doi.org/10.1088/0004-6256/137/6/4917)
- Khain, T., Becker, J. C., Adams, F. C., et al. 2018, *AJ*, 156, 273, doi: [10.3847/1538-3881/aaeb2a](https://doi.org/10.3847/1538-3881/aaeb2a)
- Khare, B. N., Sagan, C., Arakawa, E. T., et al. 1984, *Icarus*, 60, 127, doi: [10.1016/0019-1035\(84\)90142-8](https://doi.org/10.1016/0019-1035(84)90142-8)
- Khare, B. N., Thompson, W. R., Cheng, L., et al. 1993, *Icarus*, 103, 290, doi: [10.1006/icar.1993.1071](https://doi.org/10.1006/icar.1993.1071)
- Lacerda, P., Fornasier, S., Lellouch, E., et al. 2014, *ApJ Letters*, 793, L2, doi: [10.1088/2041-8205/793/1/L2](https://doi.org/10.1088/2041-8205/793/1/L2)
- Lellouch, E., Santos-Sanz, P., Lacerda, P., et al. 2013, *A&A*, 557, A60, doi: [10.1051/0004-6361/201322047](https://doi.org/10.1051/0004-6361/201322047)
- Levison, H. F., & Duncan, M. J. 1997, *Icarus*, 127, 13, doi: [10.1006/icar.1996.5637](https://doi.org/10.1006/icar.1996.5637)
- Licandro, J., di Fabrizio, L., Pinilla-Alonso, N., de León, J., & Oliva, E. 2006a, *A&A*, 457, 329, doi: [10.1051/0004-6361:20064906](https://doi.org/10.1051/0004-6361:20064906)
- Licandro, J., Grundy, W. M., Pinilla-Alonso, N., & Leisy, P. 2006b, *A&A*, 458, L5, doi: [10.1051/0004-6361:20066028](https://doi.org/10.1051/0004-6361:20066028)
- Licandro, J., Oliva, E., & Di Martino, M. 2001, *A&A*, 373, L29, doi: [10.1051/0004-6361:20010758](https://doi.org/10.1051/0004-6361:20010758)
- Licandro, J., Pinilla-Alonso, N., Pedani, M., et al. 2006c, *A&A*, 445, L35, doi: [10.1051/0004-6361:200500219](https://doi.org/10.1051/0004-6361:200500219)
- Lorenzi, V., Pinilla-Alonso, N., Licandro, J., Dalle Ore, C. M., & Emery, J. P. 2014, *A&A*, 562, A85, doi: [10.1051/0004-6361/201322251](https://doi.org/10.1051/0004-6361/201322251)
- Marsset, M., Fraser, W. C., Bannister, M. T., et al. 2020, *The Planetary Science Journal*, 1, 16, doi: [10.3847/PSJ/ab8cc0](https://doi.org/10.3847/PSJ/ab8cc0)
- Mastrapa, R. M., Sandford, S. A., Roush, T. L., Cruikshank, D. P., & Dalle Ore, C. M. 2009, *ApJ*, 701, 1347, doi: [10.1088/0004-637X/701/2/1347](https://doi.org/10.1088/0004-637X/701/2/1347)
- Materese, C. K., Cruikshank, D. P., Sandford, S. A., Imanaka, H., & Nuevo, M. 2015, *ApJ*, 812, 150, doi: [10.1088/0004-637X/812/2/150](https://doi.org/10.1088/0004-637X/812/2/150)
- Materese, C. K., Cruikshank, D. P., Sandford, S. A., et al. 2014, *ApJ*, 788, 111, doi: [10.1088/0004-637X/788/2/111](https://doi.org/10.1088/0004-637X/788/2/111)
- Merlin, F., Barucci, M. A., Dotto, E., de Bergh, C., & Lo Curto, G. 2005, *A&A*, 444, 977, doi: [10.1051/0004-6361:20053642](https://doi.org/10.1051/0004-6361:20053642)

- Merlin, F., Guilbert, A., Dumas, C., et al. 2007, *A&A*, 466, 1185, doi: [10.1051/0004-6361:20066866](https://doi.org/10.1051/0004-6361:20066866)
- Merlin, F., Quirico, E., Barucci, M. A., & de Bergh, C. 2012, *A&A*, 544, A20, doi: [10.1051/0004-6361/201219181](https://doi.org/10.1051/0004-6361/201219181)
- Merlin, F., Alvarez-Candal, A., Delsanti, A., et al. 2009, *AJ*, 137, 315, doi: [10.1088/0004-6256/137/1/315](https://doi.org/10.1088/0004-6256/137/1/315)
- Morbidelli, A., & Nesvorný, D. 2020, *The Trans-Neptunian Solar System*, 25, doi: [10.1016/B978-0-12-816490-7.00002-3](https://doi.org/10.1016/B978-0-12-816490-7.00002-3)
- Müller, T., Lellouch, E., & Fornasier, S. 2020, *Trans-Neptunian objects and Centaurs at thermal wavelengths*, ed. D. Prialnik, M. A. Barucci, & L. Young, 153–181, doi: [10.1016/B978-0-12-816490-7.00007-2](https://doi.org/10.1016/B978-0-12-816490-7.00007-2)
- Müller, T. G., Lellouch, E., Bönhardt, H., et al. 2009, *Earth Moon and Planets*, 105, 209, doi: [10.1007/s11038-009-9307-x](https://doi.org/10.1007/s11038-009-9307-x)
- Palmer, E. E., & Brown, R. H. 2008, *Icarus*, 195, 434, doi: [10.1016/j.icarus.2007.11.020](https://doi.org/10.1016/j.icarus.2007.11.020)
- Parker, A. H., & Kavelaars, J. J. 2010, *ApJL*, 722, L204, doi: [10.1088/2041-8205/722/2/L204](https://doi.org/10.1088/2041-8205/722/2/L204)
- Pedregosa, F., Varoquaux, G., Gramfort, A., et al. 2011, *Journal of Machine Learning Research*, 12, 2825
- Peixinho, N., Delsanti, A., & Doressoundiram, A. 2015, *A&A*, 577, A35, doi: [10.1051/0004-6361/201425436](https://doi.org/10.1051/0004-6361/201425436)
- Perna, D., Dotto, E., Barucci, M. A., et al. 2013, *A&A*, 554, A49, doi: [10.1051/0004-6361/201219859](https://doi.org/10.1051/0004-6361/201219859)
- Perna, D., Barucci, M. A., Fornasier, S., et al. 2010, *A&A*, 510, A53, doi: [10.1051/0004-6361/200913654](https://doi.org/10.1051/0004-6361/200913654)
- Petit, J.-M., Kavelaars, J. J., Gladman, B. J., et al. 2011, *AJ*, 142, 131, doi: [10.1088/0004-6256/142/4/131](https://doi.org/10.1088/0004-6256/142/4/131)
- Pinilla-Alonso, N., Brunetto, R., Licandro, J., et al. 2009, *A&A*, 496, 547, doi: [10.1051/0004-6361/200809733](https://doi.org/10.1051/0004-6361/200809733)
- Pinilla-Alonso, N., Licandro, J., Gil-Hutton, R., & Brunetto, R. 2007, *A&A*, 468, L25, doi: [10.1051/0004-6361:20077294](https://doi.org/10.1051/0004-6361:20077294)
- Pinilla-Alonso, N., Licandro, J., & Lorenzi, V. 2008, *A&A*, 489, 455, doi: [10.1051/0004-6361:200810226](https://doi.org/10.1051/0004-6361:200810226)
- Pinilla-Alonso, N., Roush, T. L., Marzo, G. A., Cruikshank, D. P., & Dalle Ore, C. M. 2011, *Icarus*, 215, 75, doi: [10.1016/j.icarus.2011.07.004](https://doi.org/10.1016/j.icarus.2011.07.004)
- Pinilla-Alonso, N., Stansberry, J. A., & Holler, B. J. 2020, *Physical and Compositional Properties of Large TNOs: from Spitzer, to JWST*, ed. D. Prialnik, M. A. Barucci, & L. Young, 395–412, doi: [10.1016/B978-0-12-816490-7.00018-7](https://doi.org/10.1016/B978-0-12-816490-7.00018-7)
- Protopapa, S., Alvarez-Candal, A., Barucci, M. A., et al. 2009, *A&A*, 501, 375, doi: [10.1051/0004-6361/200810572](https://doi.org/10.1051/0004-6361/200810572)
- Quirico, E., & Schmitt, B. 1997, *Icarus*, 127, 354, doi: [10.1006/icar.1996.5663](https://doi.org/10.1006/icar.1996.5663)
- Reach, W. T., Megeath, S. T., Cohen, M., et al. 2005, *PASP*, 117, 978, doi: [10.1086/432670](https://doi.org/10.1086/432670)
- Schaller, E. L., & Brown, M. E. 2007a, *ApJ*, 659, L61, doi: [10.1086/516709](https://doi.org/10.1086/516709)
- . 2007b, *ApJ*, 670, L49, doi: [10.1086/524140](https://doi.org/10.1086/524140)
- . 2008, *ApJ*, 684, L107, doi: [10.1086/592232](https://doi.org/10.1086/592232)
- Schwamb, M. E., Fraser, W. C., Bannister, M. T., et al. 2019, *ApJ*, 243, 12, doi: [10.3847/1538-4365/ab2194](https://doi.org/10.3847/1538-4365/ab2194)
- Seccull, T., Fraser, W. C., Puzia, T. H., Brown, M. E., & Schönebeck, F. 2018, *ApJ*, 855, L26, doi: [10.3847/2041-8213/aab3dc](https://doi.org/10.3847/2041-8213/aab3dc)
- Smith, E. V. P., & Gottlieb, D. M. 1974, *Space Sci. Rev.*, 16, 771, doi: [10.1007/BF00182600](https://doi.org/10.1007/BF00182600)
- Snodgrass, C., Carry, B., Dumas, C., & Hainaut, O. 2010, *A&A*, 511, A72, doi: [10.1051/0004-6361/200913031](https://doi.org/10.1051/0004-6361/200913031)
- Stansberry, J., Grundy, W., Brown, M., et al. 2008, *Physical Properties of Kuiper Belt and Centaur Objects: Constraints from the Spitzer Space Telescope*, ed. M. A. Barucci, H. Boehnhardt, D. P. Cruikshank, A. Morbidelli, & R. Dotson, 161–179
- Tegler, S. C., Romanishin, W., Consolmagno, G. J., & J., S. 2016, *AJ*, 152, 210, doi: [10.3847/0004-6256/152/6/210](https://doi.org/10.3847/0004-6256/152/6/210)
- Thirouin, A., Ortiz, J. L., Campo Bagatin, A., et al. 2012, *MNRAS*, 424, 3156, doi: [10.1111/j.1365-2966.2012.21477.x](https://doi.org/10.1111/j.1365-2966.2012.21477.x)
- Trujillo, C. A., & Brown, M. E. 2002, *APJ*, 566, L125, doi: [10.1086/339437](https://doi.org/10.1086/339437)
- Trujillo, C. A., Brown, M. E., Barkume, K. M., Schaller, E. L., & Rabinowitz, D. L. 2007, *ApJ*, 655, 1172, doi: [10.1086/509861](https://doi.org/10.1086/509861)
- Trujillo, C. A., Brown, M. E., Rabinowitz, D. L., & Geballe, T. R. 2005, *ApJ*, 627, 1057, doi: [10.1086/430337](https://doi.org/10.1086/430337)
- Van Laerhoven, C., Gladman, B., Volk, K., et al. 2019, *AJ*, 158, 49, doi: [10.3847/1538-3881/ab24e1](https://doi.org/10.3847/1538-3881/ab24e1)
- Vilenius, E., Kiss, C., Mommert, M., et al. 2012, *A&A*, 541, A94, doi: [10.1051/0004-6361/201118743](https://doi.org/10.1051/0004-6361/201118743)
- Vilenius, E., Kiss, C., Müller, T., et al. 2014, *A&A*, 564, A35, doi: [10.1051/0004-6361/201322416](https://doi.org/10.1051/0004-6361/201322416)
- Vilenius, E., Stansberry, J., Müller, T., et al. 2018, *A&A*, 618, A136, doi: [10.1051/0004-6361/201732564](https://doi.org/10.1051/0004-6361/201732564)
- Werner, M. W., Roellig, T. L., Low, F. J., et al. 2004, *ApJS*, 154, 1, doi: [10.1086/422992](https://doi.org/10.1086/422992)
- Young, L. A., Braga-Ribas, F., & Johnson, R. E. 2020, *Volatiles evolution and atmospheres of Trans-Neptunian objects*, ed. D. Prialnik, M. A. Barucci, & L. Young, 127–151, doi: [10.1016/B978-0-12-816490-7.00006-0](https://doi.org/10.1016/B978-0-12-816490-7.00006-0)

APPENDIX

A. INDIVIDUAL ANALYSIS OF THE SAMPLE

In the following, we analyze and provide the surface composition for each object individually. All proportions for different materials are calculated using the diagram $K - 3.6 \mu\text{m}$ versus $3.6 \mu\text{m} - 4.5 \mu\text{m}$, also named the compositional clock (unless otherwise indicated in the text):

- The spectra of 1996 GQ₂₁ was studied by [Doressoundiram et al. \(2003\)](#), who found no water detection. Later, [Barkume et al. \(2008\)](#) obtained a new spectrum claiming a detection of water at the 3σ level, which was later supported by [Barucci et al. \(2011\)](#). [Barkume et al. \(2008\)](#) also suggested the presence of CH₃OH. Our measurements for this object provide only an upper limit for the color index $3.6 \mu\text{m} - 4.5 \mu\text{m}$. However, this limit constrains the region in which the object is localized within the diagram, eliminating the possibility of having other ices but water. Nonetheless, it is possible that large amounts of water could be hiding the CH₃OH, as in the case for Orcus (see section 6.2).
- 1998 SN₁₆₅ has no spectrum published in the literature. Its location in the figure 9 indicates that the surface of this object is dominated by silicates, with a small probability of the presence of water ice (taking into account the error bars). We obtain a proportion of $90 \pm 20\%$ silicates, and $10 \pm 10\%$ H₂O, and no organics. Note that this object is an inner-belt classical object with a heliocentric ecliptic inclination of $i = 4.6^\circ$; we compute a free inclination (with respect to the local forced plane) of 3.5° . The fact that this object appears similar to hot classicals despite a low i provides evidence for Section 11’s argument for a “hot only” inner classical belt.
- 1999 DE₉ has been reported by several authors to have tentative water ice bands in its spectrum ([Jewitt & Luu 2001](#); [Brown et al. 2007b](#); [Barkume et al. 2008](#)). Counter to this, [Alvarez-Candal et al. \(2007\)](#) published a spectrum with no indications of water related bands, however, they mentioned that the absorption bands that the other authors found were placed at $2 \mu\text{m}$, a region of the spectrum that they had to remove due to the strong atmospheric absorption. Nonetheless, this object appears in a region of the compositional clock where there is no presence of water ice but CH₄. In fact, 1999 DE₉ was reported by [Jewitt & Luu \(2001\)](#) to have features near 1.4 and $2.25 \mu\text{m}$ similar to what is found in the centaur Pholus, for which they interpreted the presence of solid CH₃OH on its surface (although, they claim that the spectrum was not good enough for them to definitively make this identification). Our measurements are consistent with the detection of CH₃OH on its surface. We obtain a composition of $20 \pm 10\%$ H₂O, $60 \pm 10\%$ CH₃OH, and $20 \pm 10\%$ organics.
- 1999 OJ₄ for which we only provide measurements at $3.6 \mu\text{m}$. However, inspecting its spectrophotometric measurements, this object is red and with an absorption band at $3.6 \mu\text{m}$ with respect to the K -band. As no absorptions are found at VNIR wavelengths, and due to its deep slope, such an absorption band should be due to complex organics. Considering the diagram $V - 3.6 \mu\text{m}$ versus $J - 3.6 \mu\text{m}$, we obtain a composition of $40 \pm 50\%$ H₂O, $0 \pm 30\%$ silicates, and $60 \pm 50\%$ organics. Note that this object is an inner-belt classical object with a heliocentric ecliptic inclination of $i = 4.0^\circ$ for which we compute a free inclination of 2.3° .
- The published spectra for 2000 GN₁₇₁ have presented conflicting interpretations about the presence of water. [de Bergh et al. \(2004\)](#) found an absorption band at $\sim 1.6 \mu\text{m}$ that they reported to be related to water. However, [Alvarez-Candal et al. \(2007\)](#) obtained the spectrum of this object where no water bands were present. Later, [Barkume et al. \(2008\)](#) modeled a new spectra of 2000 GN₁₇₁ that included 10% of water. Finally, [Guilbert et al. \(2009\)](#) presented another spectrum that is in agreement with the one published by [Alvarez-Candal et al. \(2007\)](#). In the compositional clock, the position of this object corresponds to a composition of $20 \pm 20\%$ H₂O, $40 \pm 20\%$ silicates, and $40 \pm 20\%$ organics.
- 2000 PE₃₀ has no spectrum published in the literature. the position of this object in the diagram is consistent with a composition of $20 \pm 10\%$ H₂O, $60 \pm 20\%$ silicates, and $30 \pm 10\%$ organics.
- We only provide upper limit measurements of 2001 QT₃₂₂ at 3.6 and $4.5 \mu\text{m}$. However, this object appears similar to hot classicals despite a low i (1.8° , with a free inclination of 2.4°). This object provides evidence for Section 11’s argument for a “hot only” inner classical belt.

- Doressoundiram et al. (2005) and Barkume et al. (2008) both obtained the spectrum of 2002 AW₁₉₇ and both reported a very small fraction of water. However, Guilbert et al. (2009) also observed this object, and suggested that the band found at $2\ \mu\text{m}$ is related to incomplete removal of telluric features. Its position in the compositional clock corresponds to a composition of $20 \pm 10\%$ H₂O, $60 \pm 10\%$ silicates, and $20 \pm 10\%$ organics.
- 2002 KX₁₄ was studied by Barkume et al. (2008) and Guilbert et al. (2009) with no apparent detection of H₂O-ice bands in the spectra. Considering the diagram $3.6\ \mu\text{m} - 4.5\ \mu\text{m}$ versus $V - 3.6\ \mu\text{m}$, we obtain a composition of $20 \pm 10\%$ H₂O, $60 \pm 10\%$ silicates, and $20 \pm 10\%$ organics, in agreement with previous reports. Note that this object is an inner-belt classical object with a heliocentric ecliptic inclination of $i = 0.4^\circ$; we compute a free inclination (with respect to the local forced plane) of 2.7° . The fact that this object appears similar to hot classicals despite a low i provides evidence for Section 11’s argument for a “hot only” inner classical belt.
- 2002 TC₃₀₂ has been reported to tentatively have water ice (Barkume et al. 2008; Barucci et al. 2011). Stansberry et al. (2008) also suggested that this object has very little fresh ice on its surface. Our results agree with both conclusions, with a composition of $20 \pm 10\%$ H₂O, $30 \pm 20\%$ silicates, and $50 \pm 20\%$ organics. For a mixture of H₂O-CH₃OH-organics, we obtain $40 \pm 20\%$, $30 \pm 10\%$, and $30 \pm 30\%$, respectively; however, those amounts of H₂O should have been detected in its spectrum. Also, the visible colors of this object are very red (see appendix B), indicating that higher presence of complex organics are more likely.
- The published spectra for 2002 UX₂₅ has presented conflicting interpretations. Barkume et al. (2008) suggested a small fraction, 6%, of water on its surface. Later, Barucci et al. (2011) obtained a new spectrum and reported no water bands. However, its position correspond to a composition of $20 \pm 10\%$ H₂O, $50 \pm 10\%$ silicates, and $30 \pm 10\%$ organics, similar to 2002 AW₁₉₇.
- 2002 VE₉₅ has a strong detection of CH₃OH (Barucci et al. 2006) and our measurements are in agreement with this detection. This object was discussed in section 6.2. We obtain a composition of $20 \pm 10\%$ H₂O, $40 \pm 10\%$ CH₃OH, and $40 \pm 20\%$ organics.
- 2003 QA₉₂ only presents measurements at $3.6\ \mu\text{m}$. The lack of infrared data prevent us to provide the existence or not of absorption bands. Note that this object is an inner-belt classical object with a heliocentric ecliptic inclination of $i = 3.4^\circ$ for which we compute a free inclination of 2.4° .
- 2004 EW₉₅ was studied by Seccull et al. (2018). They demonstrated that its composition is “consistent” with a C-type asteroid and the spectrum present a clear feature produced by hydrated, iron-rich silicates. We obtain a composition of Considering the diagram $V - 3.6\ \mu\text{m}$ versus $J - 3.6\ \mu\text{m}$, we obtain a composition of $10 \pm 10\%$ H₂O, $80 \pm 10\%$ silicates, and $10 \pm 10\%$ organics.
- 2004 NT₃₃ has been studied by several authors who are in agreement that there is no detection of water (Barkume et al. 2008; Barucci et al. 2011). We obtain a composition of $20 \pm 40\%$ H₂O, $80 \pm 60\%$ silicates, and $0 \pm 20\%$ organics. Additionally, the presence of CO₂ on its surface is also a possibility. CO₂ has been previously detected on the surface of Iapetus (Saturn’s moon), where H₂O-ice and complex organics coexist (e.g., Palmer & Brown 2008; Pinilla-Alonso et al. 2011). CO₂ could be originated as a byproduct of the interaction of these two materials.
- 2004 TY₃₆₄ has been reported to tentatively have water ice (Barkume et al. 2008; Barucci et al. 2011). Barucci et al. (2011) measured a depth for the band of 5.8%, in agreement with previous works (e.g., Barkume et al. 2008). Additionally, Merlin et al. (2012) found a band at $2.27\ \mu\text{m}$ in the spectrum of 2004 TY₃₆₄, which could be associated with methanol. The position of this object in the compositional clock corresponds to a composition of $20 \pm 10\%$ H₂O, $50 \pm 10\%$ silicates, and $30 \pm 10\%$ organics. However, if we considere a mixture of H₂O, CH₃OH, and organics, we obtain a proportion of $50 \pm 10\%$, $30 \pm 10\%$, and $20 \pm 10\%$ for each material, respectively, which increase the amount of H₂O too much for not have being clearly detected in its spectrum.
- 2005 RM₄₃ has been studied spectroscopically by Fornasier et al. (2009) and Barucci et al. (2011). No water detection was obtained by Fornasier et al. (2009), but tentative detection was reported by Barucci et al. (2011), who model the spectra using up to $\sim 40\%$. The position of this object in figure 9 is quite interesting, as this region is the one dominated by CO₂. However, error bars are quite large and could easily place the object in

a region where the surface would be completely dominated by water. Nonetheless, such amount of H_2O should be detected by VNIR spectroscopy, which is not the case. Other color-color diagrams support the possibility of this object having CO_2 (see section 7). For a mixture of H_2O , silicates and organics, we obtain a proportion of $50 \pm 40\%$, $50 \pm 40\%$, a 0% for each material, respectively.

- 2005 RN₄₃ has been reported to not have water ice on its surface by [Barkume et al. \(2008\)](#) and [Guilbert et al. \(2009\)](#); however its position in figure 9 indicates that this object is composed of $20 \pm 10\%$ H_2O , $50 \pm 10\%$ silicates, and $30 \pm 10\%$ organics.
- 2007 JJ₄₃ was studied by [Gourgeot et al. \(2015\)](#). They proposed a surface composition of around 50% of complex organics and up to 6.5% water. Our measurements result in a composition of $40 \pm 30\%$ H_2O , $40 \pm 20\%$ silicates, and $20 \pm 10\%$ organics.
- Borasisi's spectrum was published in [Barkume et al. \(2008\)](#), they obtained a spectral slope of $28.67 \pm 3.61\%/100$ nm and no absorption bands. In our data, Borasisi has only upper limit measurements in the color index $3.6 \mu\text{m} - 4.5 \mu\text{m}$ and, due to its position in the compositional clock, no strong conclusions can be drawn about the composition of this object. However, the color index $K - 3.6 \mu\text{m}$ indicates that there is an absorption band that may be either related to ices or complex organics. Also, considering the diagram $V - 3.6 \mu\text{m}$ versus $J - 3.6 \mu\text{m}$, we obtain a composition of $30 \pm 50\%$ H_2O , $40 \pm 30\%$ silicates, and $30 \pm 20\%$ organics.
- The spectrum of Huya has been studied by [Licandro et al. \(2001\)](#); [Jewitt & Luu \(2001\)](#) and [Fornasier et al. \(2004b\)](#) with the conclusion that no water ice is observed. Nonetheless, [Jewitt & Luu \(2001\)](#) suggested the possibility of a wide absorption band near $2.0 \mu\text{m}$ that could be related to water. In figure 9, the position of this object indicates a proportion of $40 \pm 20\%$ H_2O , $30 \pm 10\%$ silicates, and $30 \pm 10\%$ organics.
- [Barucci et al. \(2008\)](#); [Delsanti et al. \(2010\)](#) and [DeMeo et al. \(2010\)](#) suggested the presence of methane and their irradiated products on the surface of Orcus. We obtain a composition of $70 \pm 10\%$ H_2O , $20 \pm 10\%$ silicates, and $10 \pm 10\%$ organics. Due to the large amount of water ice found in this object, we are unable to detect methane or the irradiated products with our method, and therefore we do not exclude CH_4 as part of its composition. [DeMeo et al. \(2010\)](#) also suggested the possibility of the presence of CO_2 , and due to the position of this object in figure 11, close to the region dominated by CO_2 , we also support this possibility.
- The spectrum of Quaoar has been studied in detail by [Dalle Ore et al. \(2009\)](#) using VNIR spectroscopic and IRAC data, who reported the presence of H_2O ice and CH_4 . Our measurements agree with the results from [Dalle Ore et al. \(2009\)](#), and we report a composition of $60 \pm 10\%$ H_2O , $20 \pm 10\%$ silicates, and $20 \pm 10\%$ organics. The high percentage of water prevents from clearly detecting the presence of CH_4 . Quaoar could be then a good reference for objects with similar spectra.
- [Schaller & Brown \(2008\)](#) reported that the fraction of water ice in the surface of Salacia is consistent with zero, which is in a very good agreement with our measurements (see figure 3). Its position in the compositional clock suggests that the surface of Salacia is dominated by silicates and depleted from ices. We obtain a composition of $10 \pm 10\%$ H_2O , $90 \pm 20\%$ silicates, and no organics.
- The spectrum of Sila-Nunam has been studied by [Grundy et al. \(2005\)](#), where no water bands were found. Also, [Barucci et al. \(2011\)](#)'s reanalysis of the spectrum published by [Grundy et al. \(2005\)](#) is in agreement. [Grundy et al. \(2005\)](#) reported a neutral spectrum with no strong evidence for H_2O or CH_4 , although they noticed a dip around $2.33 \mu\text{m}$ that may arise from absorption by an organic ice. Our measurements indicate the presence of CH_4 or CH_3OH on the surface of Sila-Nunam. Due to the small size of the binary system (around 340 km; [Vilenius et al. 2012](#)), it is unlikely that this object possesses CH_4 on its surface, being more realistic to think that its position in figure 11 is due to CH_3OH . We obtain a composition of $30 \pm 10\%$ H_2O , $50 \pm 10\%$ CH_3OH , and $20 \pm 10\%$ organics.
- Varda's spectrum has been studied by [Barucci et al. \(2011\)](#), whose results are in good agreement with its position in the compositional clock. We obtain a composition of $20 \pm 10\%$ H_2O , $60 \pm 10\%$ silicates, and $30 \pm 10\%$ organics.

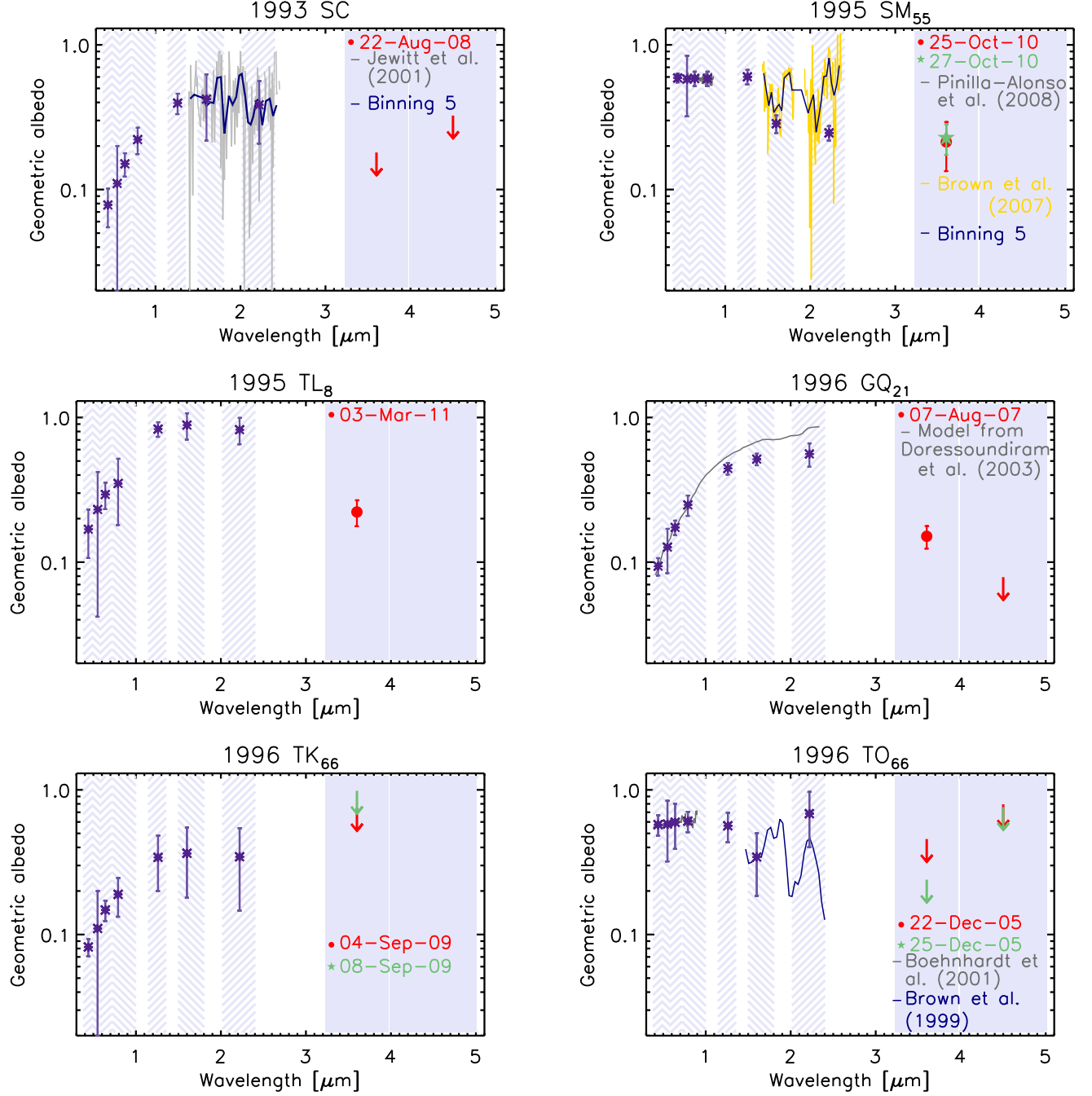
- 2001 UR₁₆₃, and 2004 GV₉ are both located within the pink circle in figure 9. The spectra of these two were studied by [Barkume et al. \(2008\)](#); [Barucci et al. \(2011\)](#); [Guilbert et al. \(2009\)](#). We obtain a composition of 20 ± 10 H₂O, $60 \pm 20\%$ silicates and 20 ± 20 organics for 2001 UR₁₆₃, and 20 ± 10 H₂O, $60 \pm 20\%$ silicates and 20 ± 10 organics for 2004 GV₉.
- G!kún||'hòmdímà was studied by [Barucci et al. \(2011\)](#), who reported water detection. We can analyze this object considering the diagram and $V - 3.6 \mu\text{m}$ versus $3.6 \mu\text{m} - 4.5 \mu\text{m}$, for which we obtain a composition of 20 ± 50 H₂O, $10 \pm 20\%$ silicates and 70 ± 50 organics.

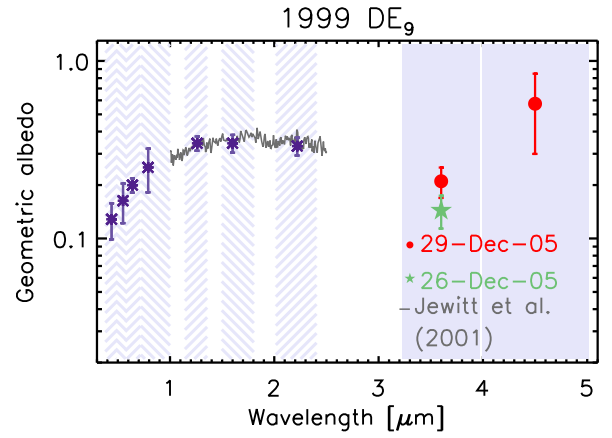
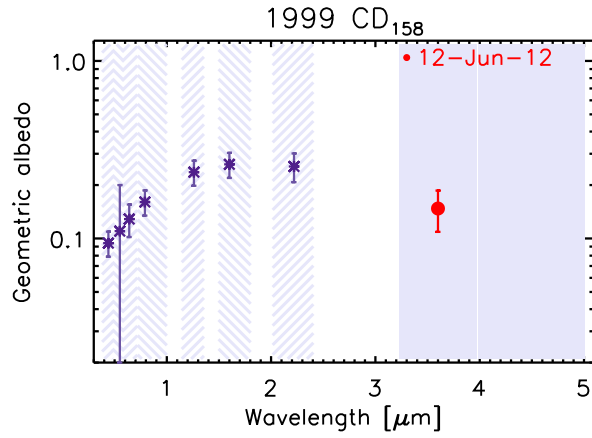
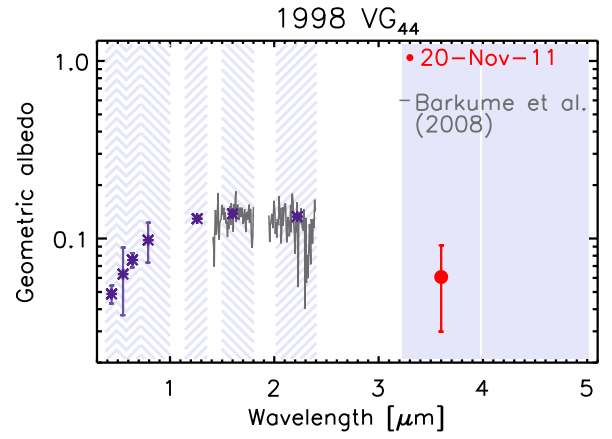
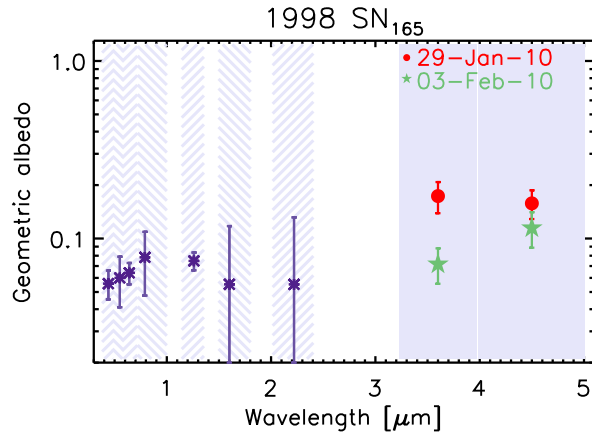
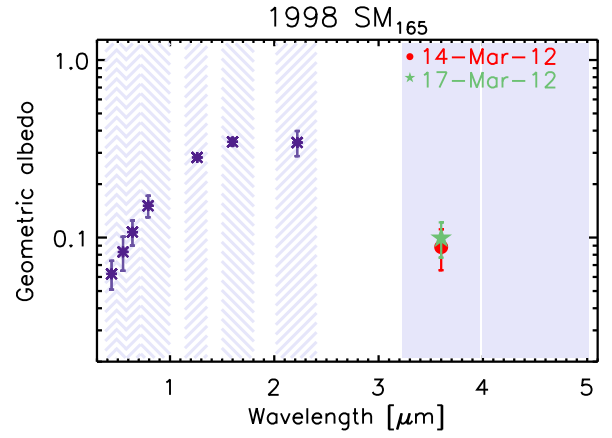
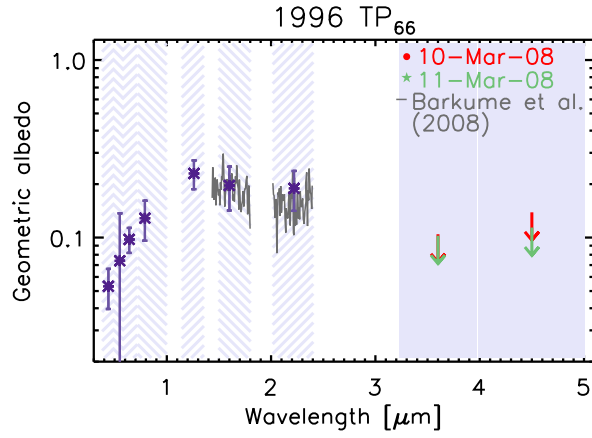
The following objects have no spectrum published in the literature. Considering the diagram $V - 3.6 \mu\text{m}$ versus $J - 3.6 \mu\text{m}$, we obtain a surface composition as follows:

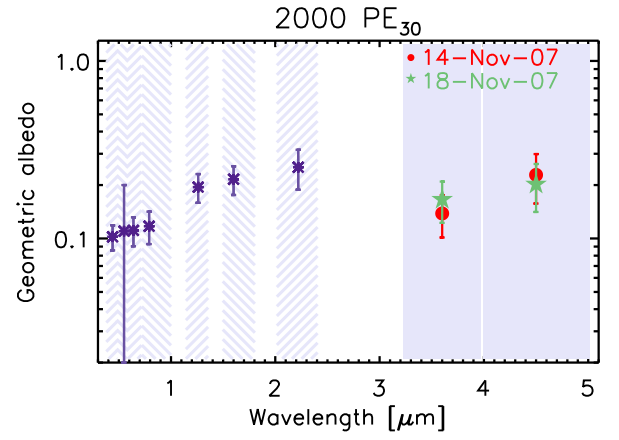
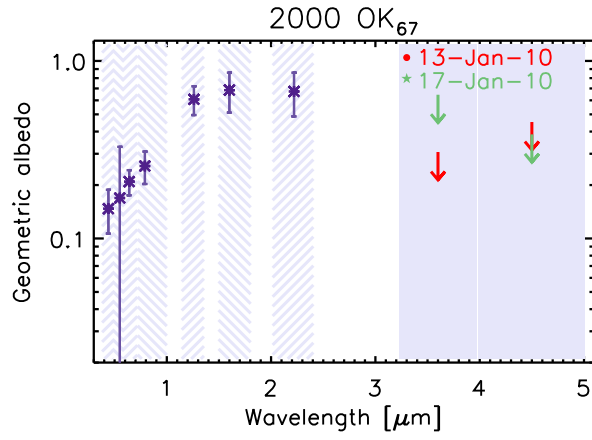
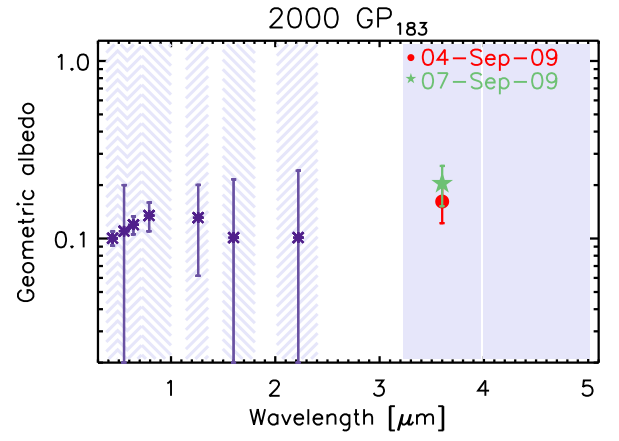
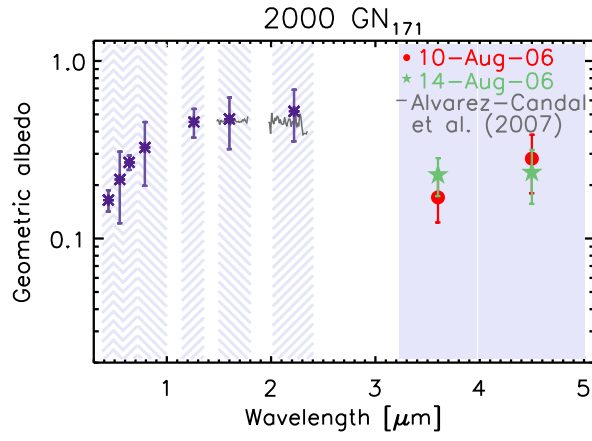
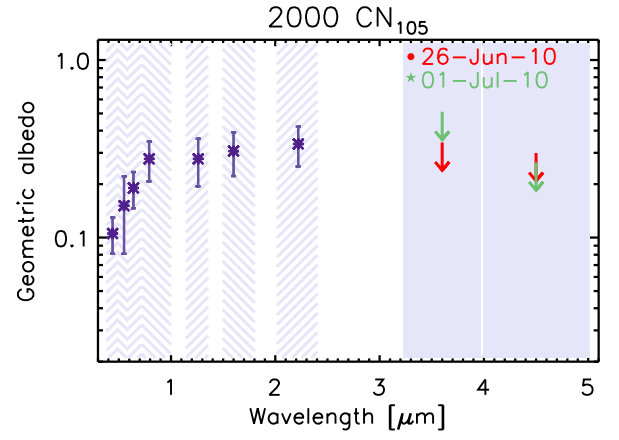
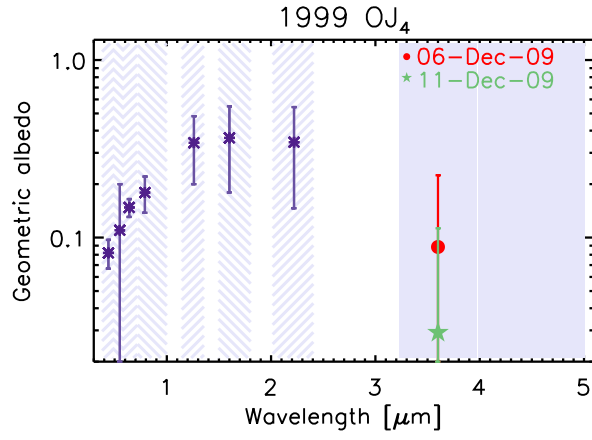
- 2000 GP₁₈₃: $10 \pm 10\%$ H₂O, $80 \pm 10\%$ silicates, and $10 \pm 10\%$ organics.
- 2000 QL₂₅₁: $10 \pm 10\%$ H₂O, $90 \pm 10\%$ silicates, and $10 \pm 10\%$ organics.
- 2001 CZ₃₁: $10 \pm 10\%$ H₂O, $80 \pm 10\%$ silicates, and $10 \pm 10\%$ organics.
- 2001 QJ₁₈₁: no H₂O, $90 \pm 10\%$ silicates, $10 \pm 10\%$, and organics.
- 2002 CY₂₂₄: no H₂O, $90 \pm 10\%$ silicates, $10 \pm 10\%$, and organics.

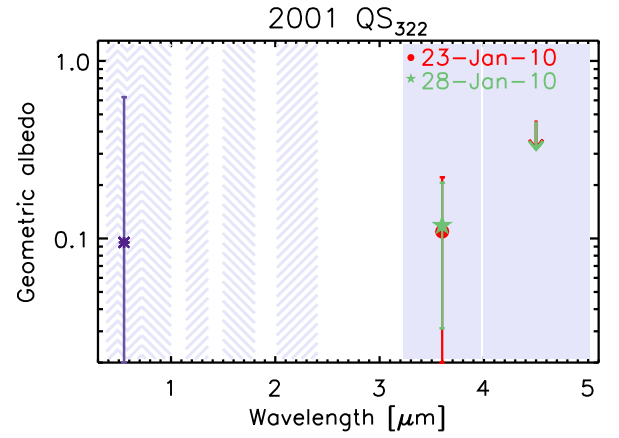
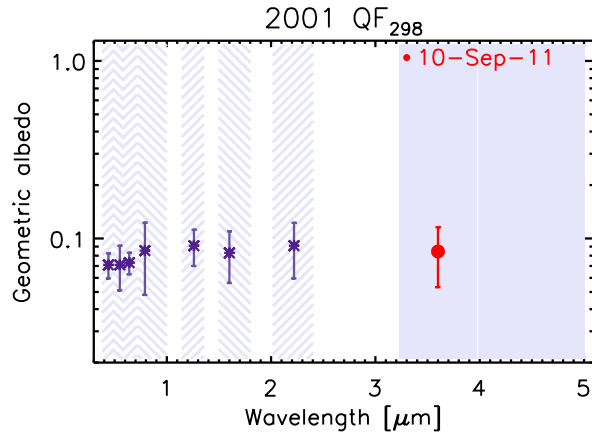
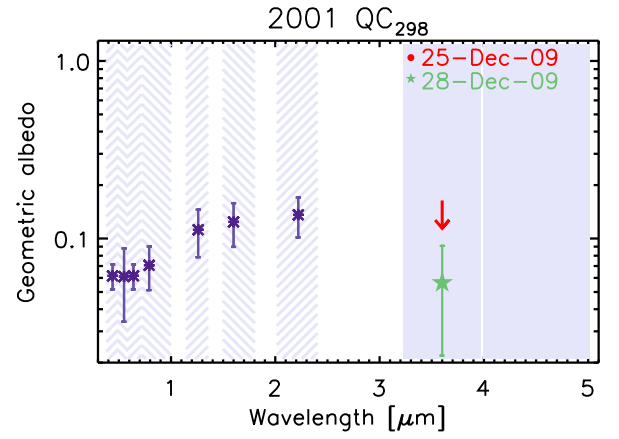
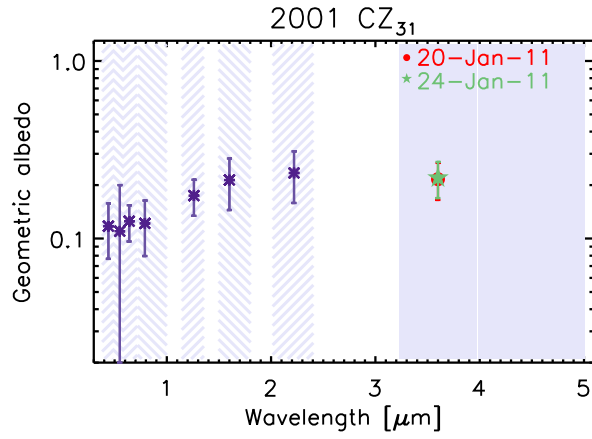
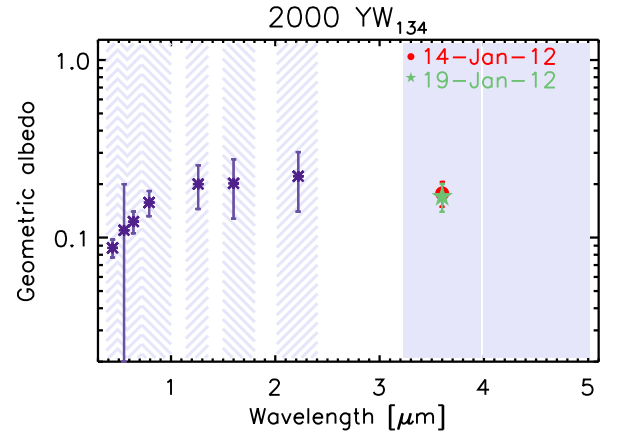
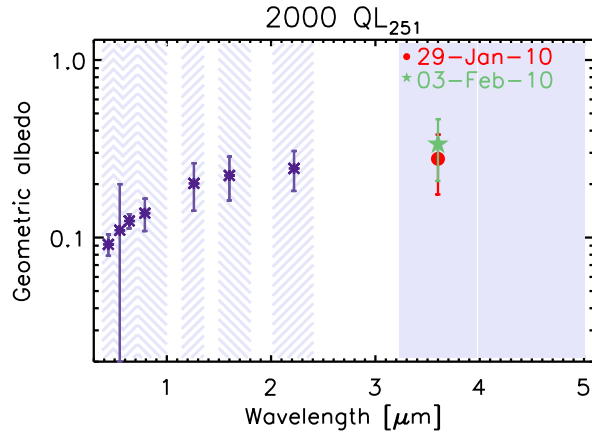
B. SPECTROPHOTOMETRIC MEASUREMENTS PLOTTED FOR EACH OBJECT

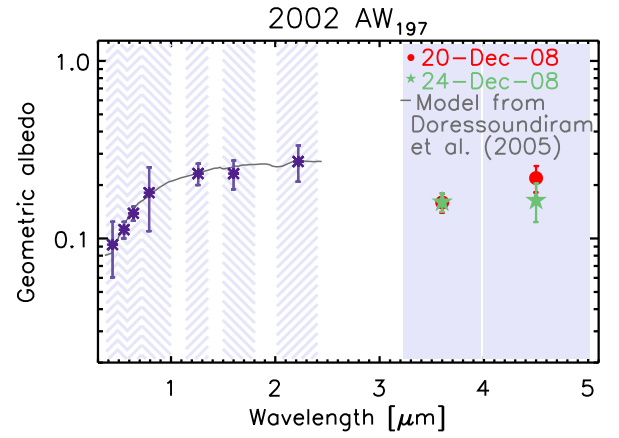
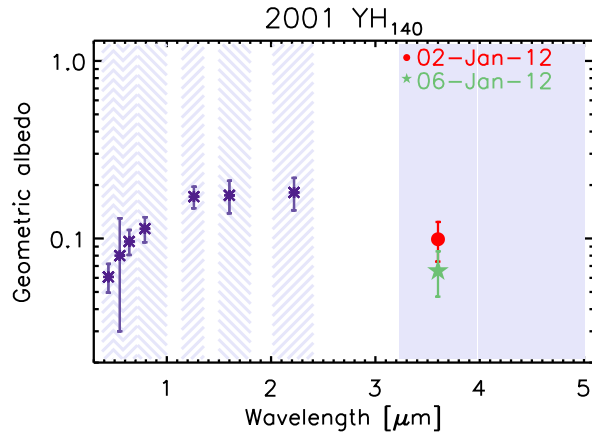
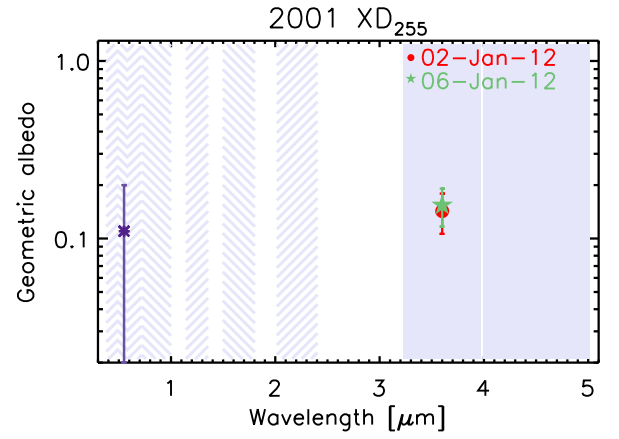
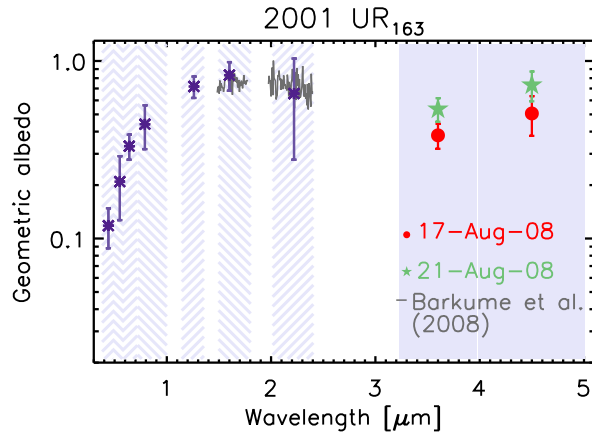
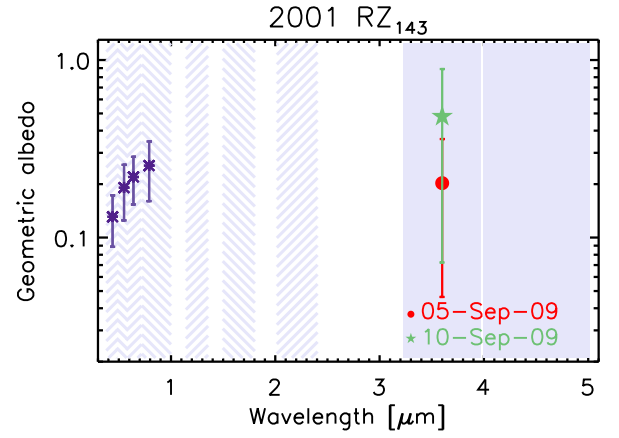
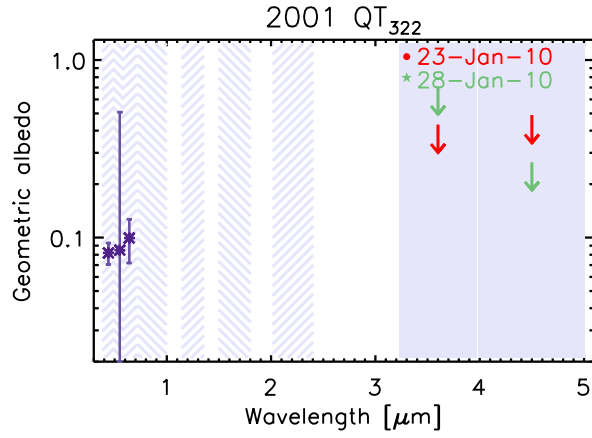
In this appendix we present the spectrophotometric measurements of our sample. When available, we also plotted the spectrum or the spectrum model (references are indicated on the plots). The figures are ordered by provisional designation in ascending order, followed by the named objects in alphabetical order.

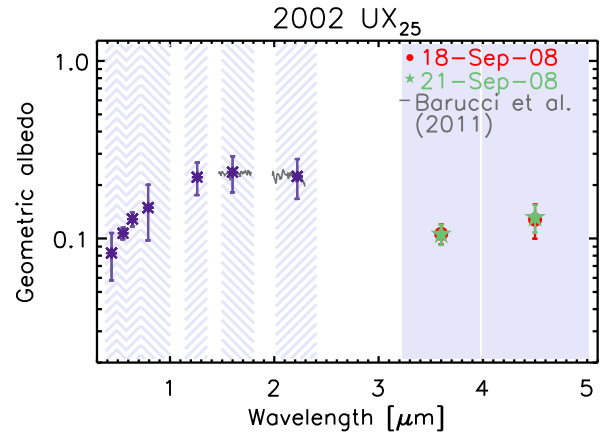
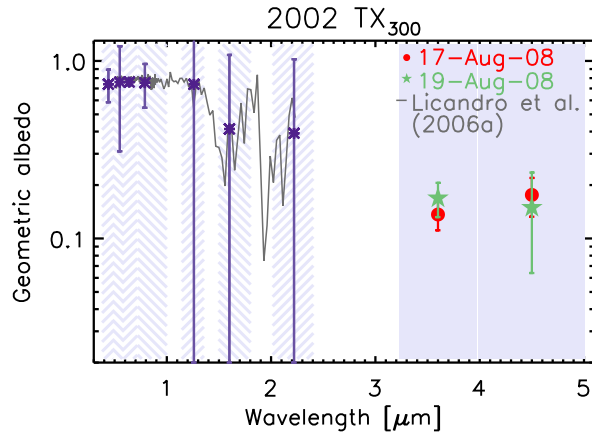
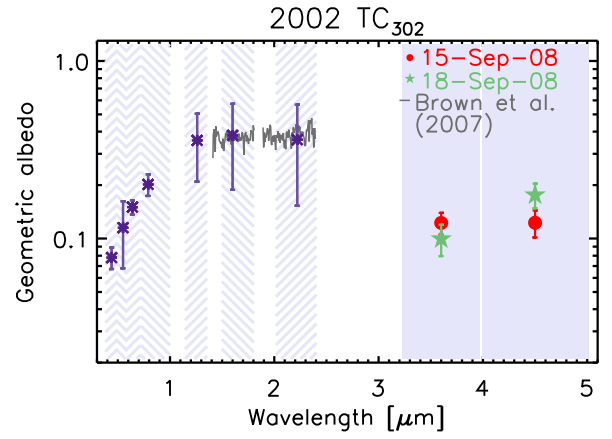
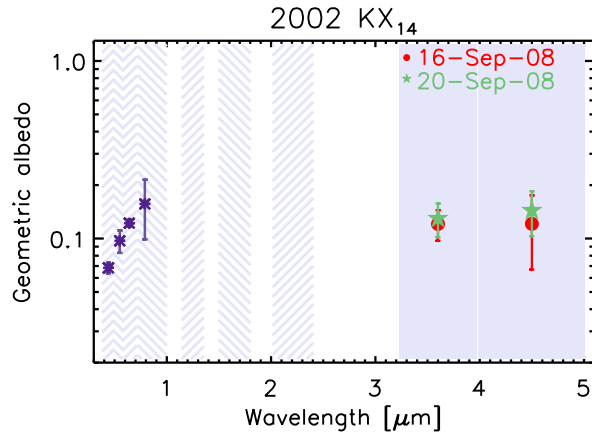
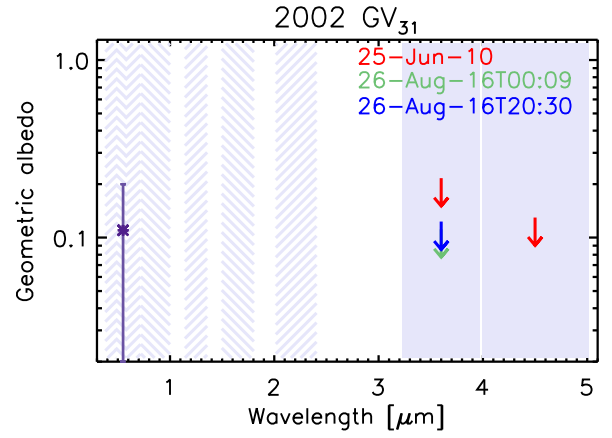
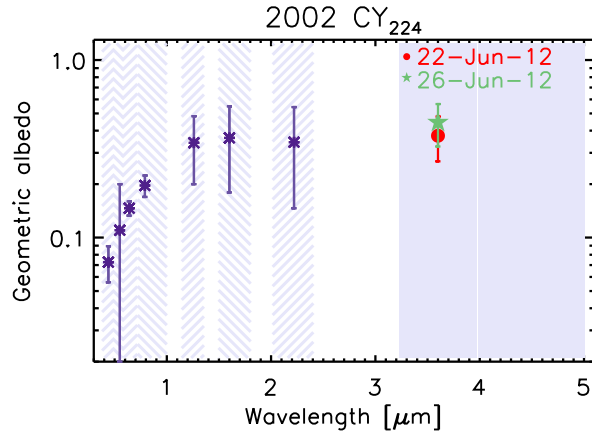


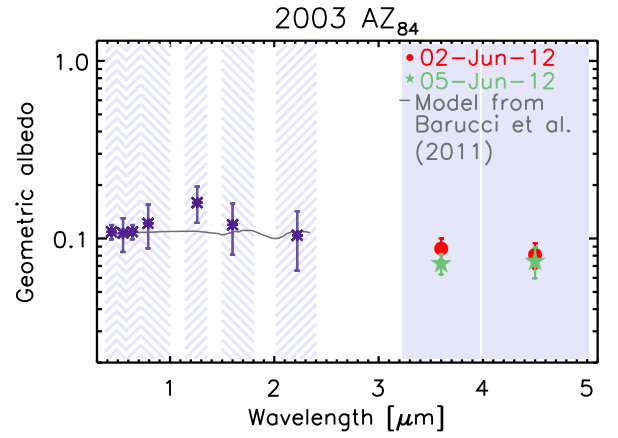
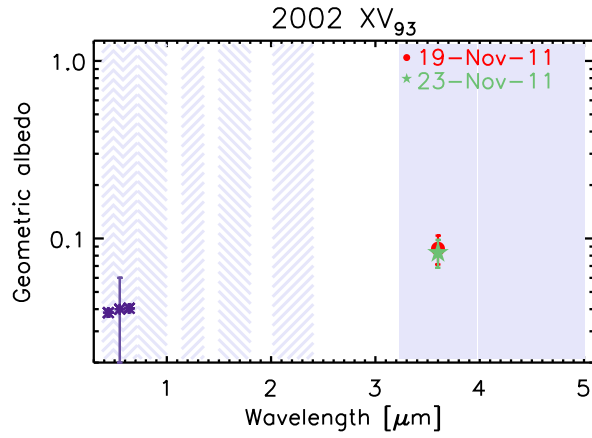
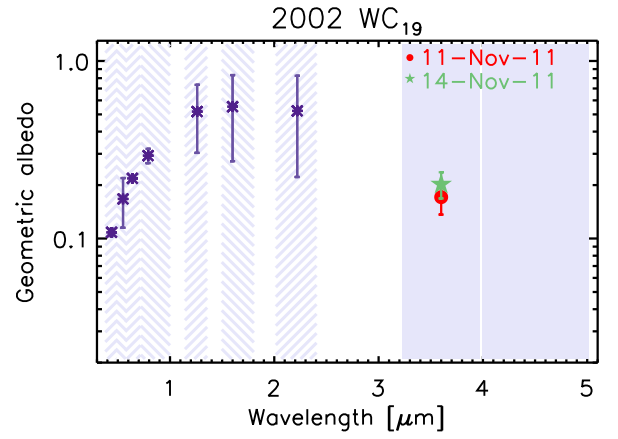
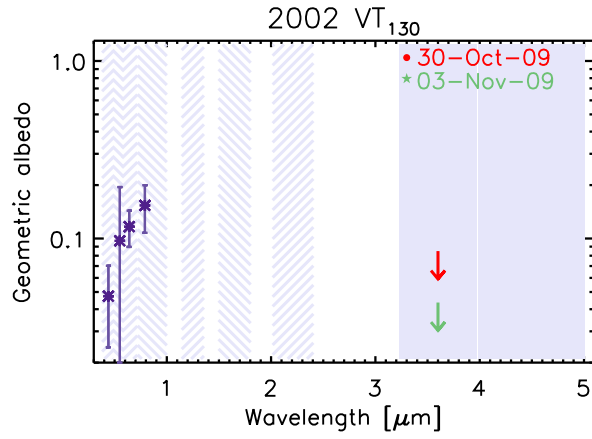
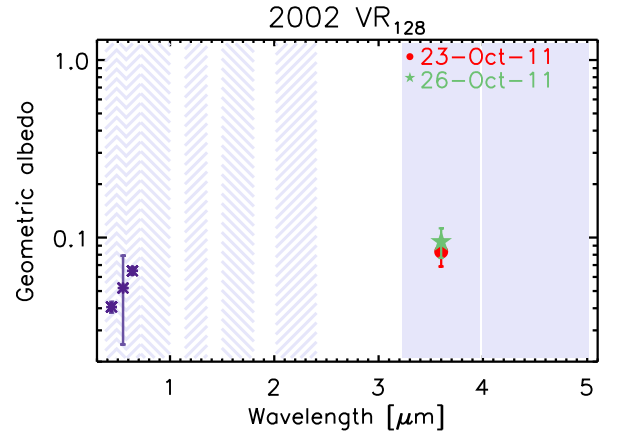
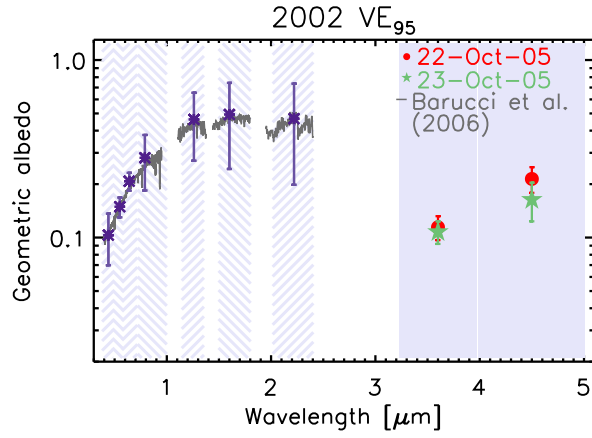


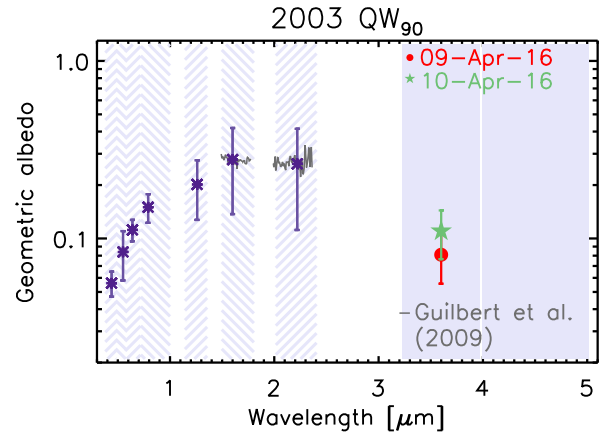
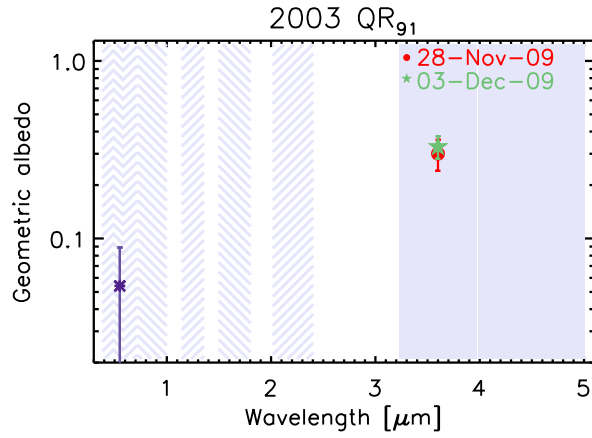
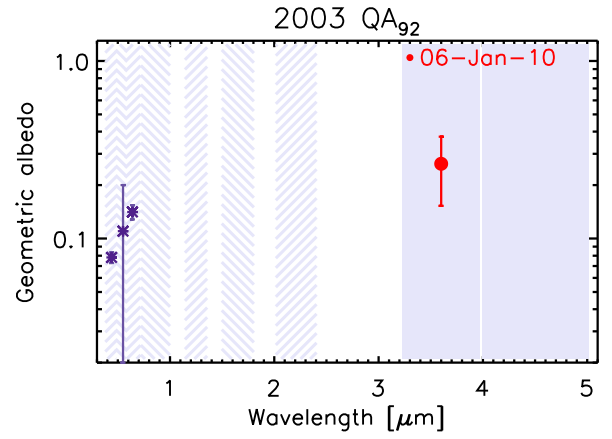
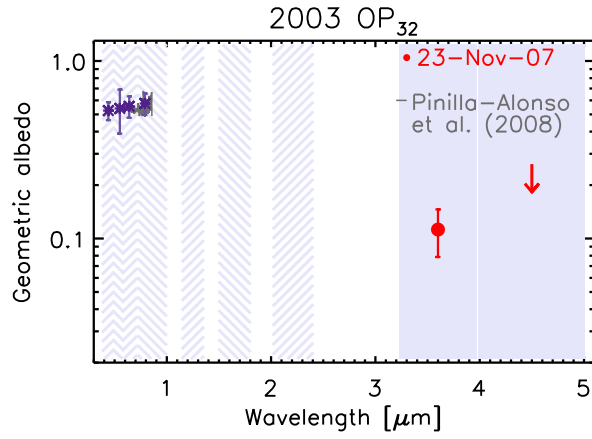
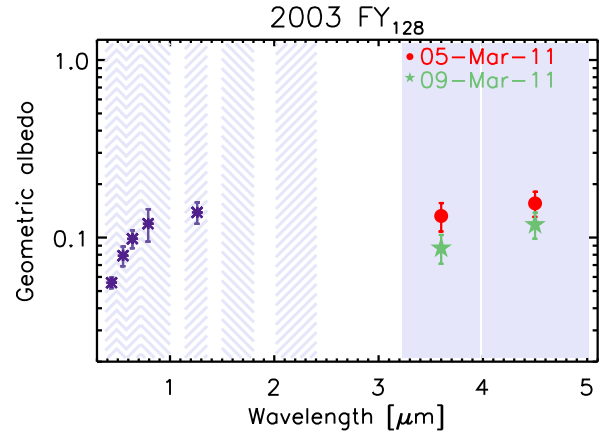
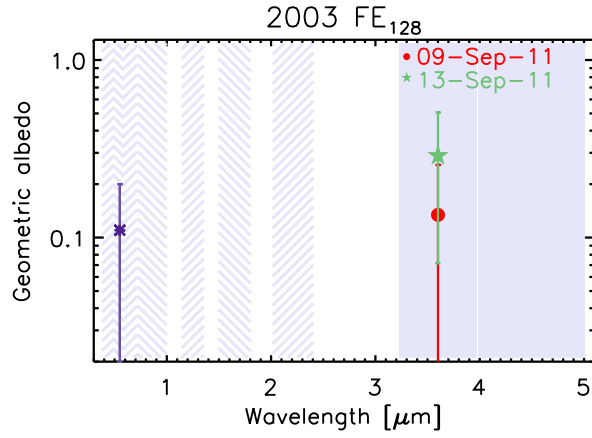


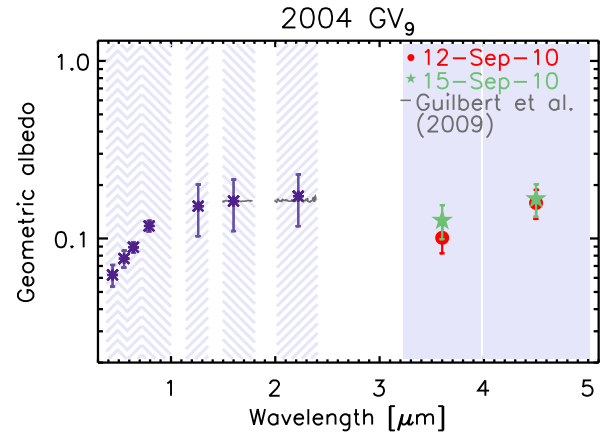
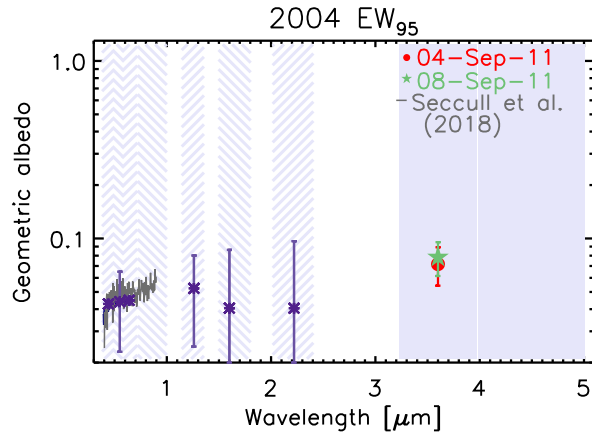
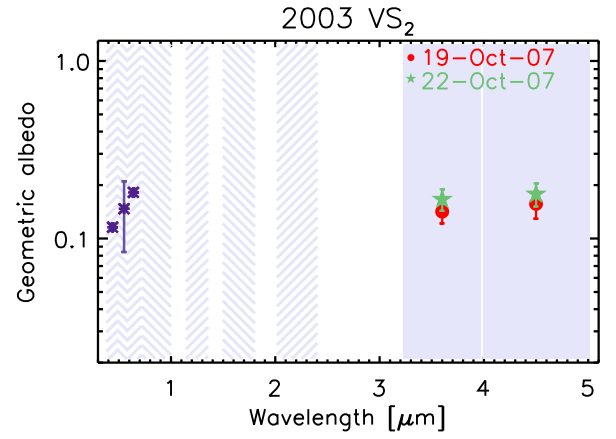
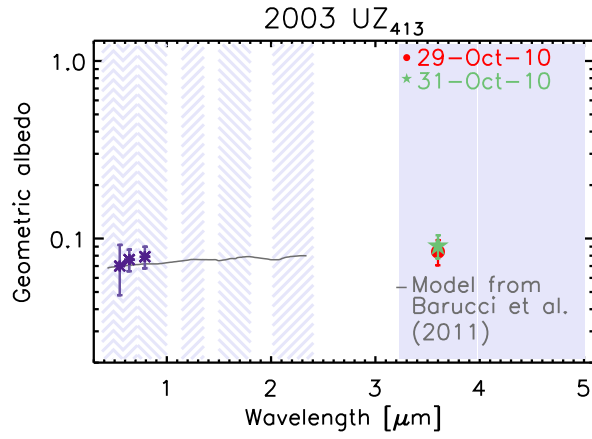
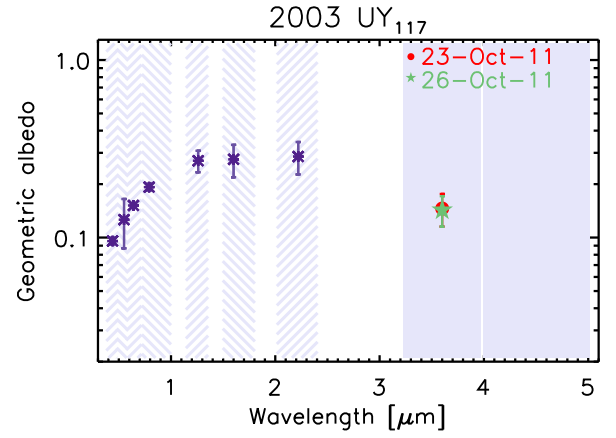
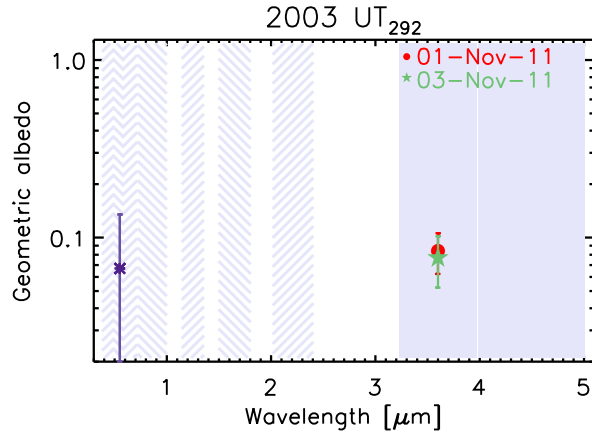


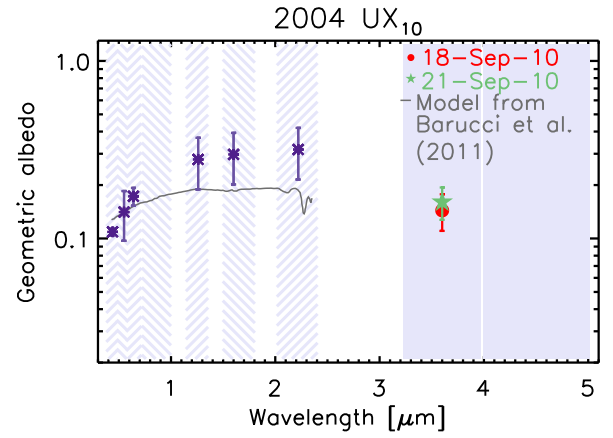
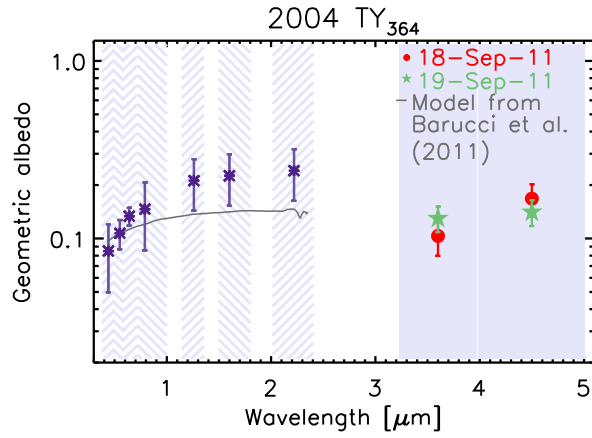
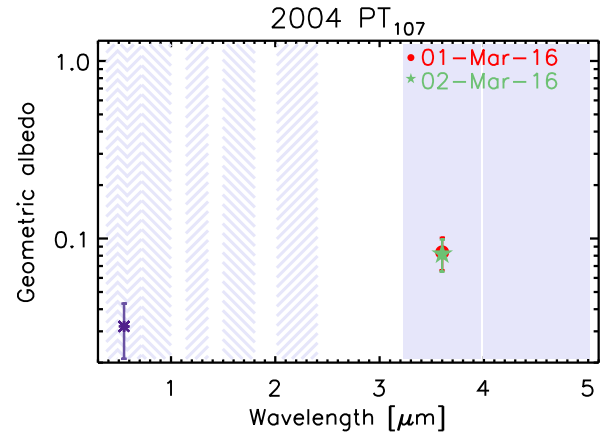
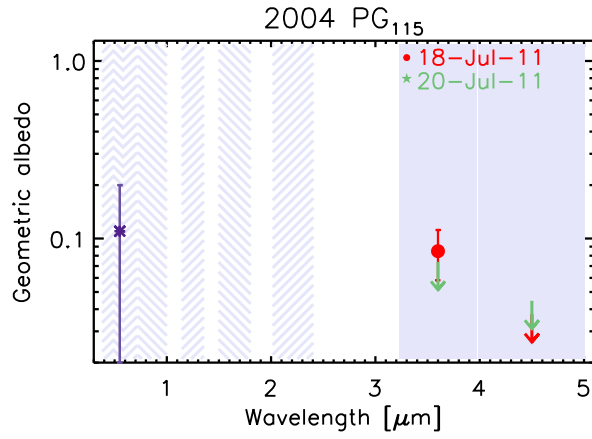
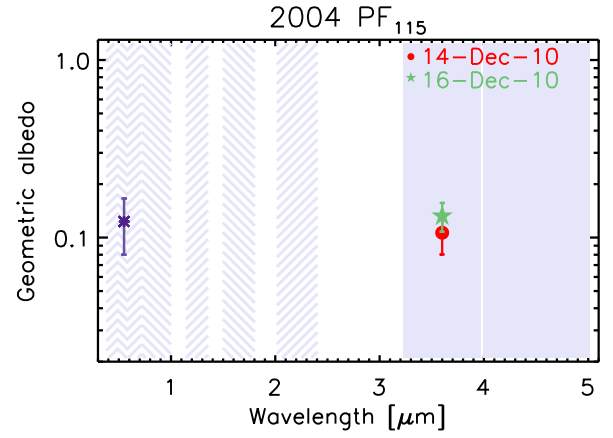
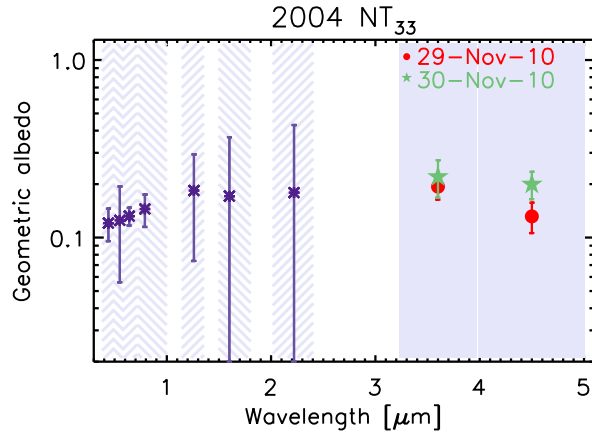


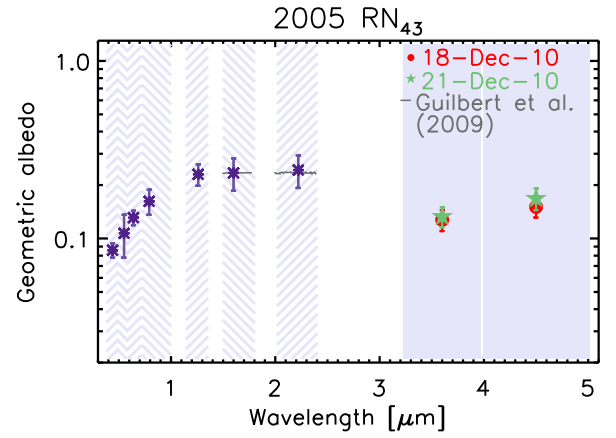
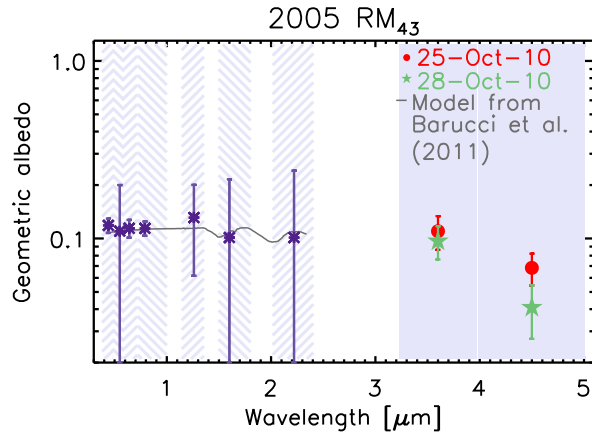
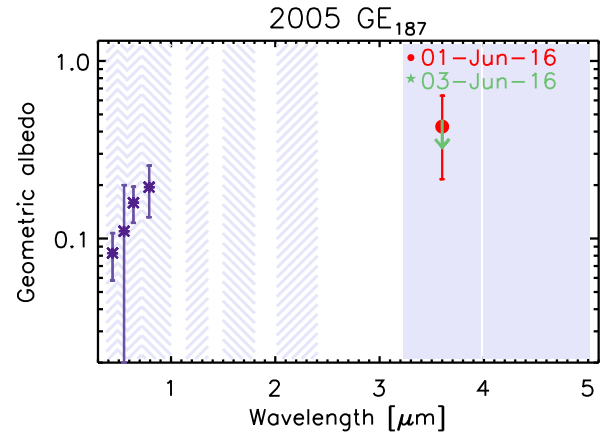
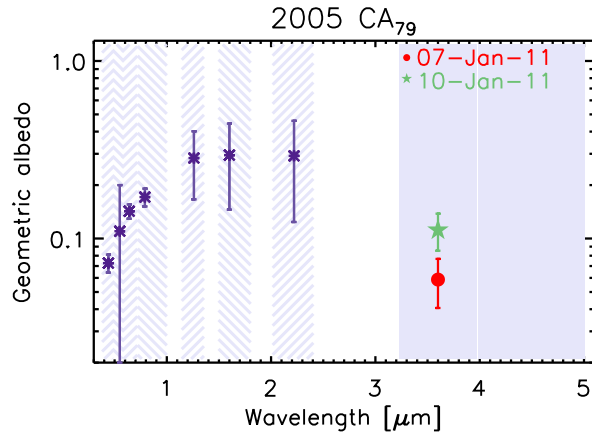
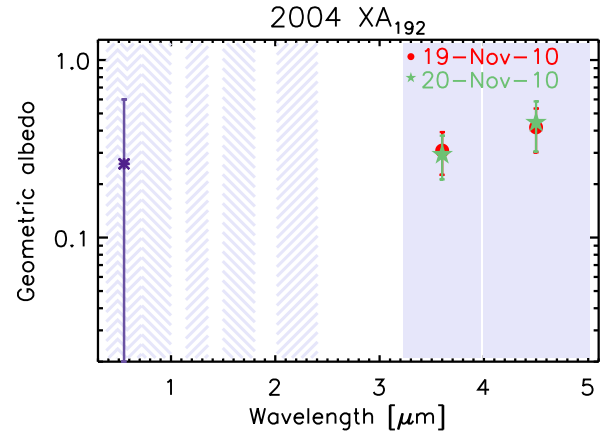
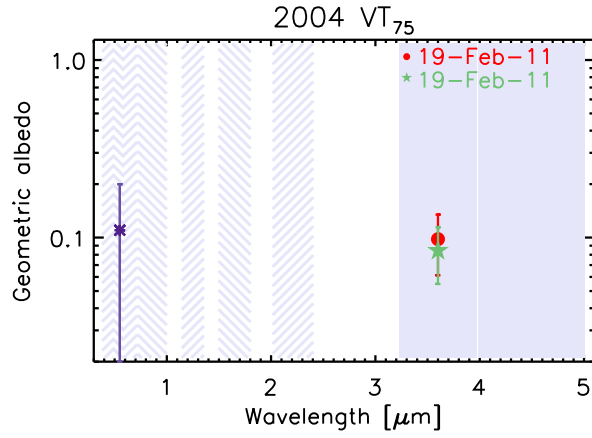


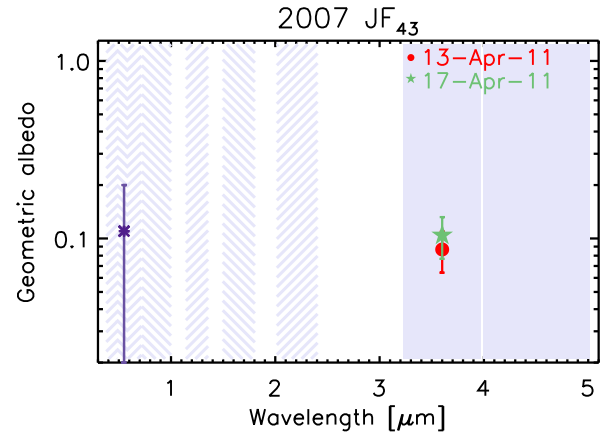
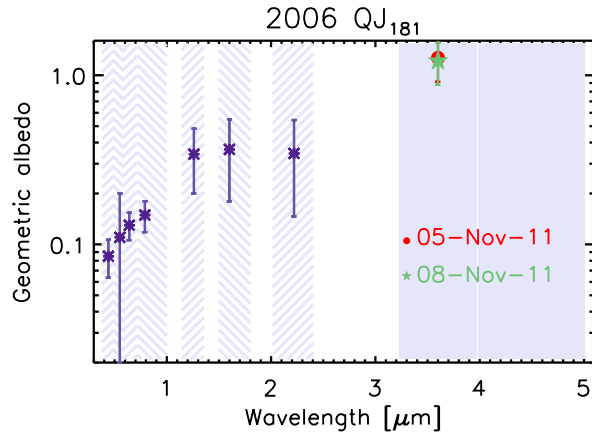
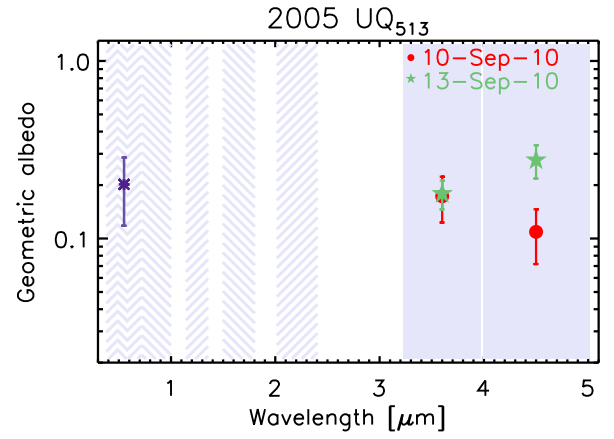
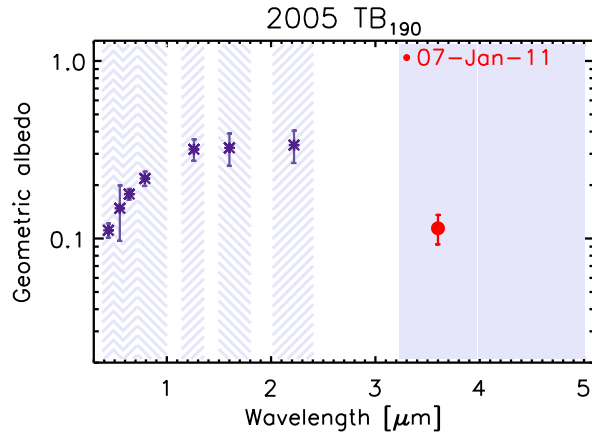
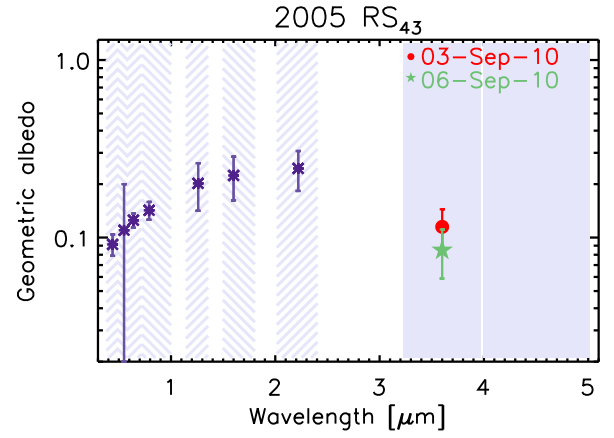
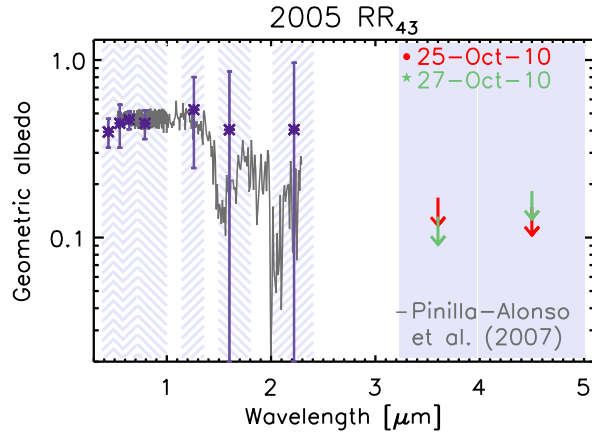


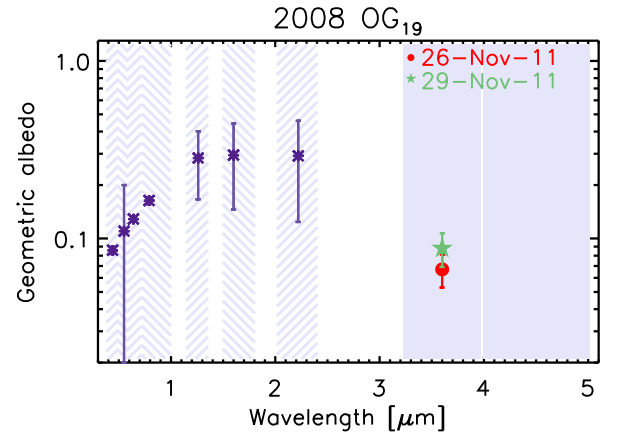
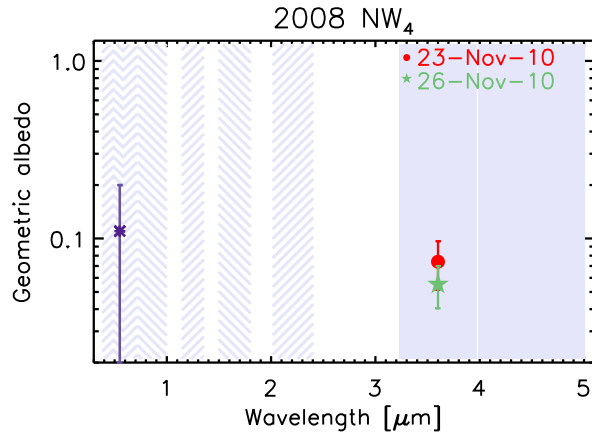
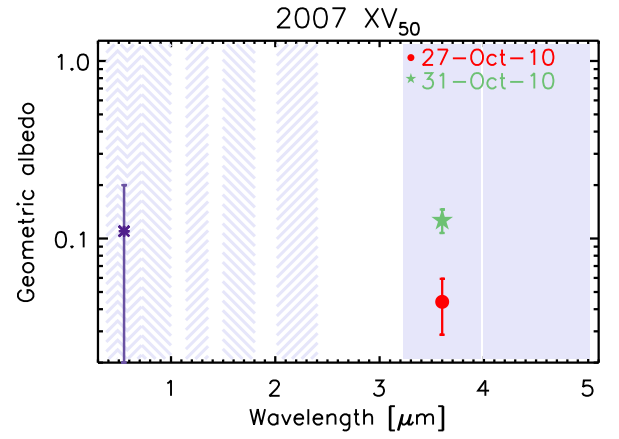
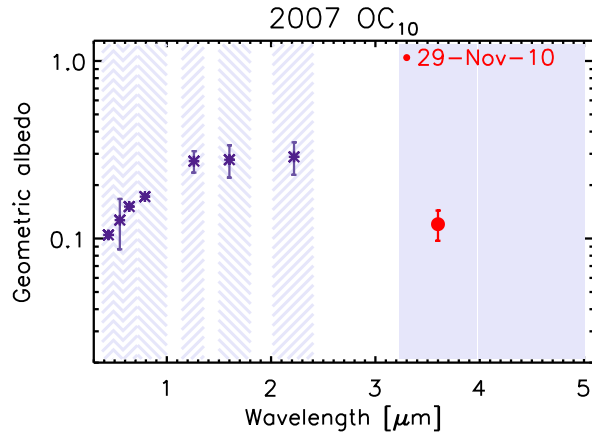
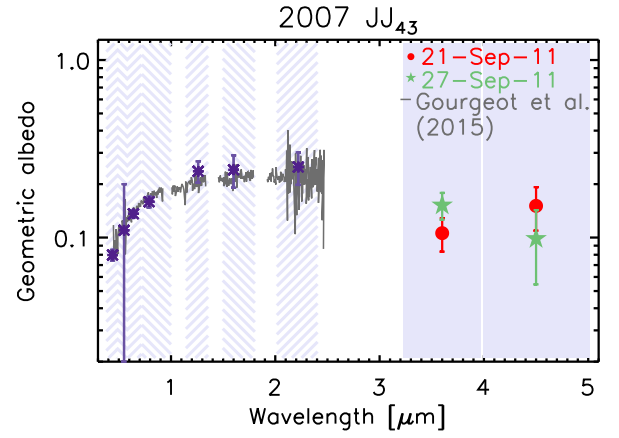
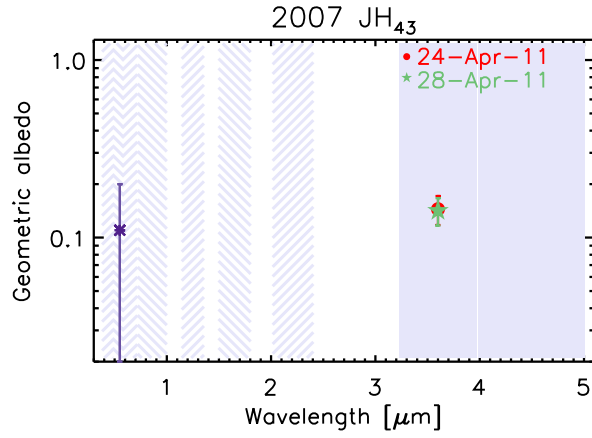


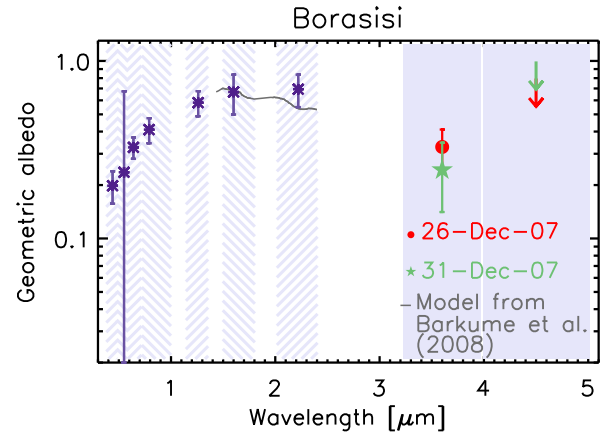
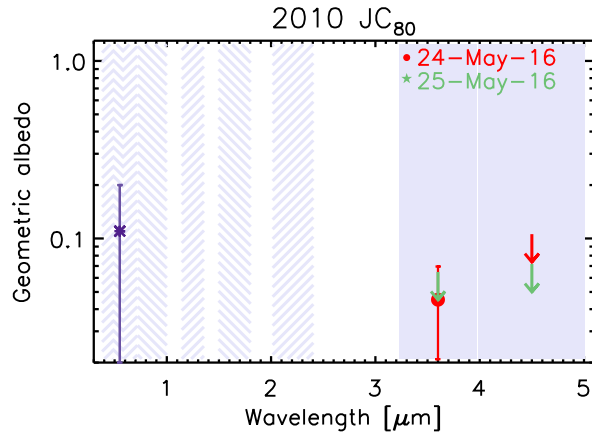
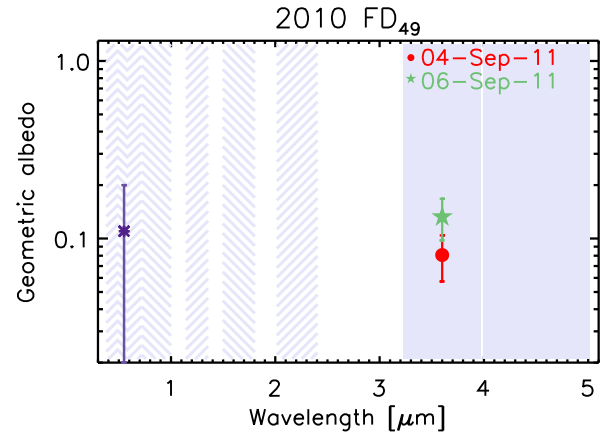
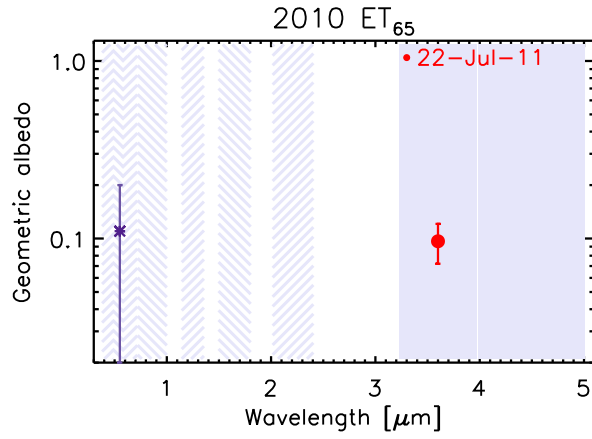
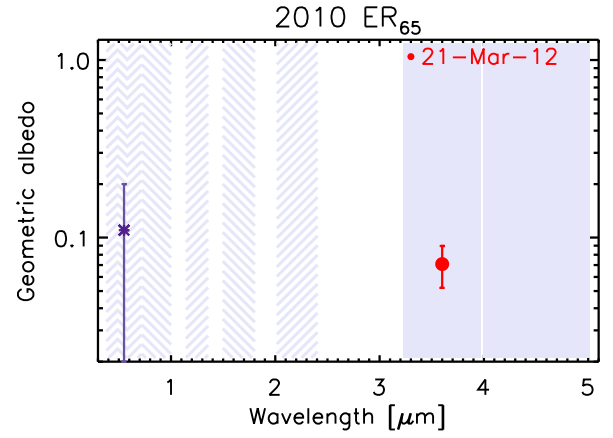
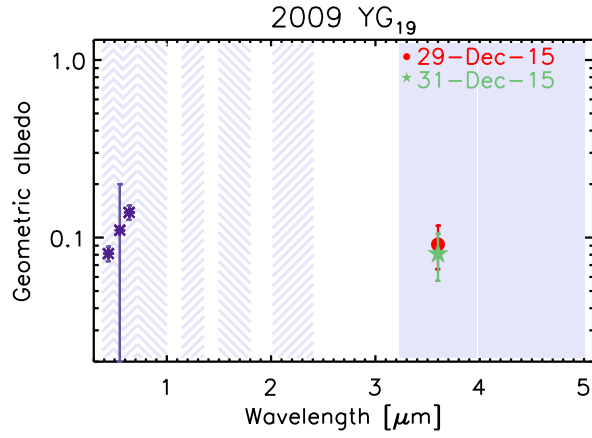


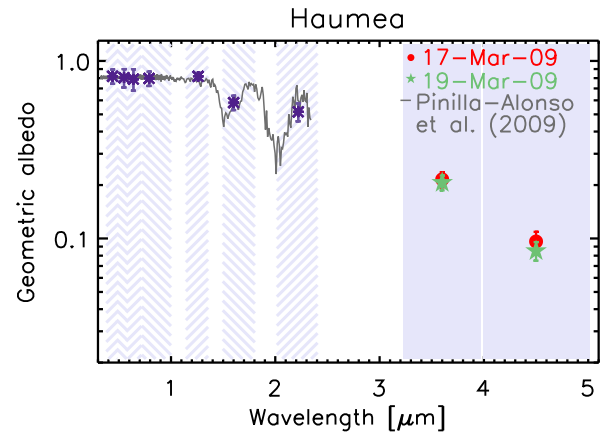
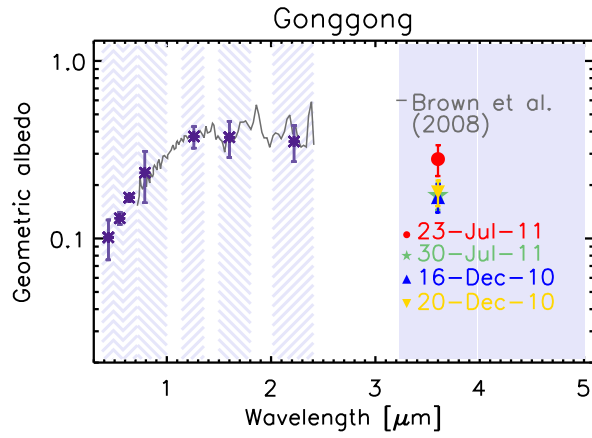
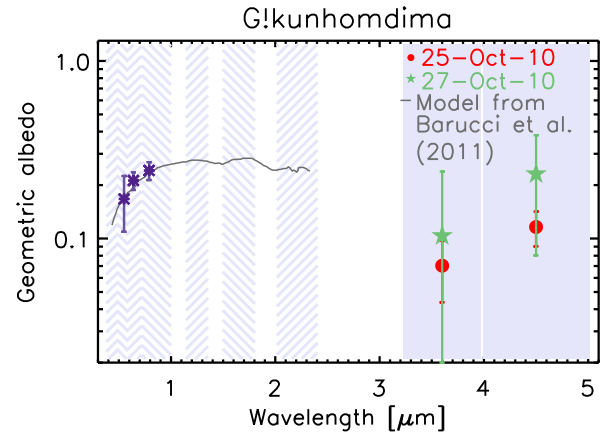
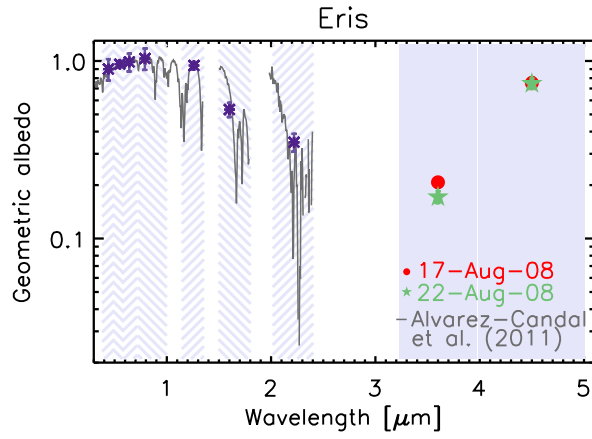
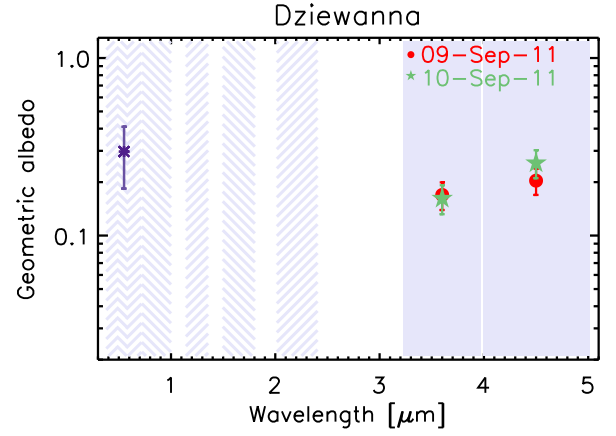
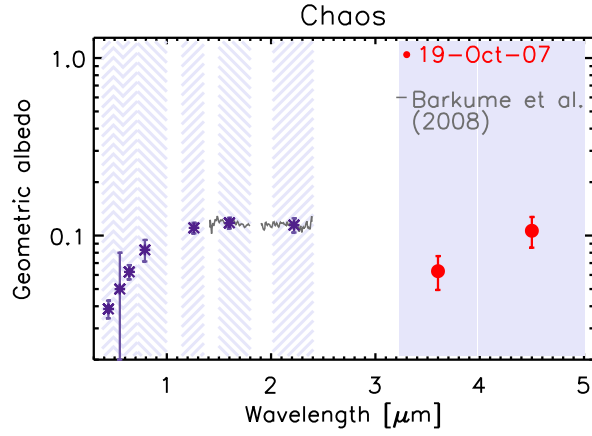


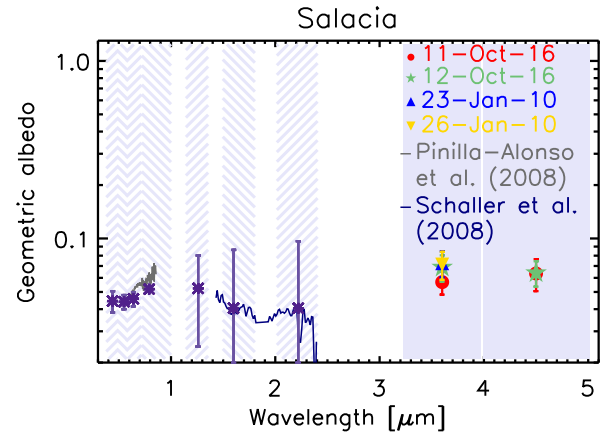
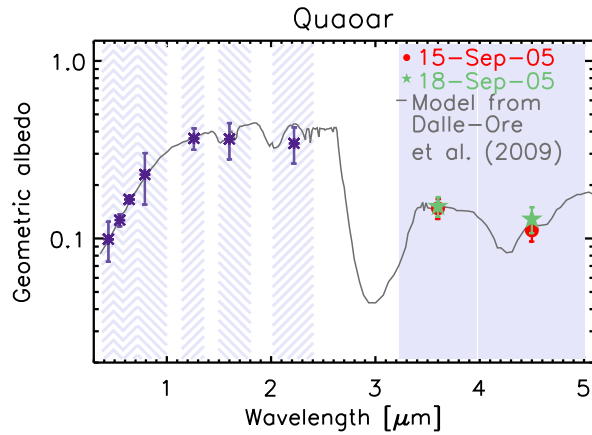
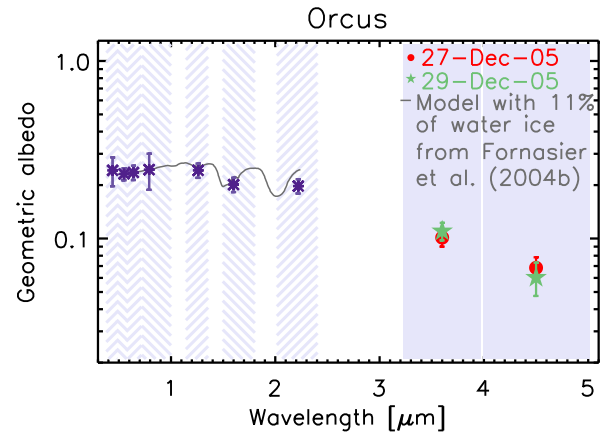
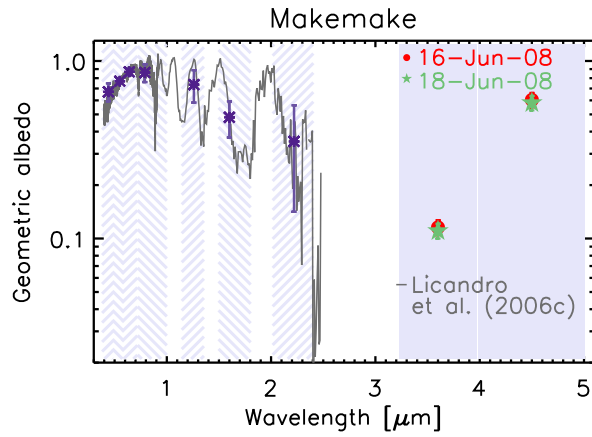
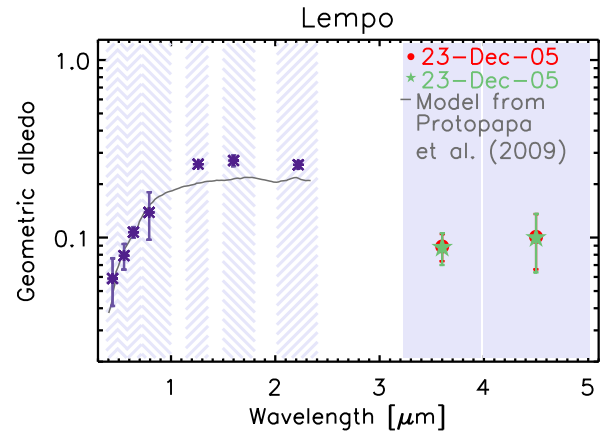
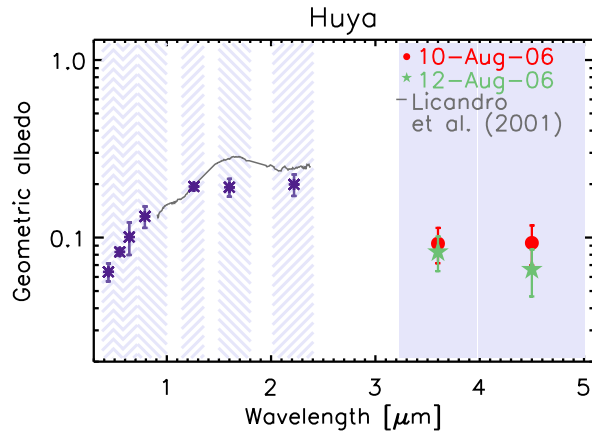


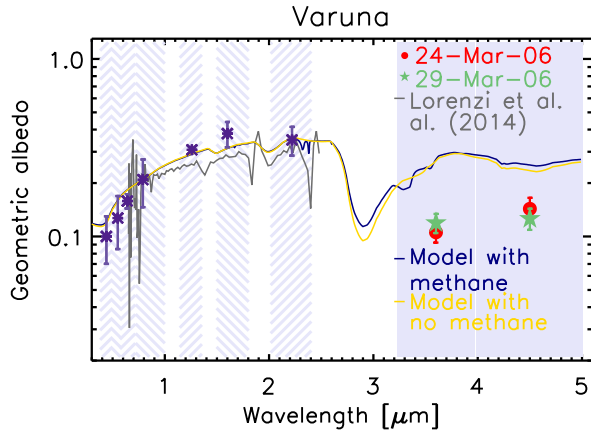
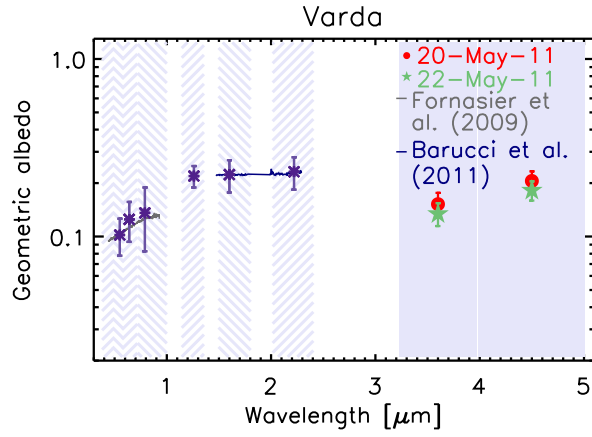
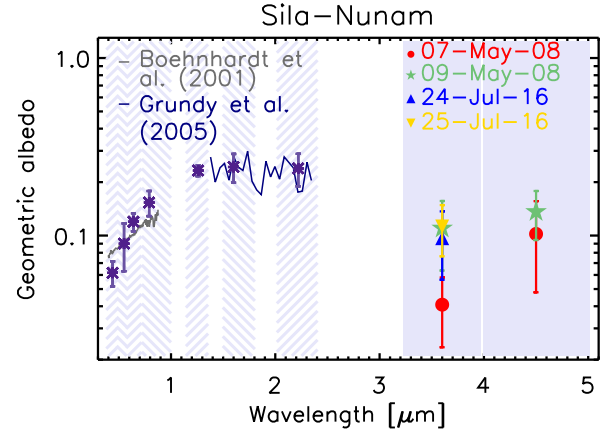
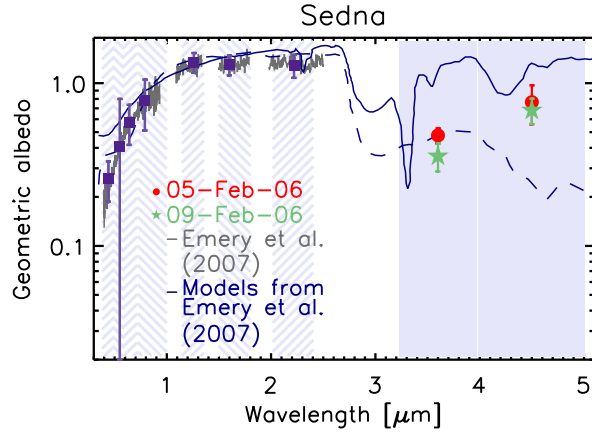












C. TABLES

Table 5. Summary of observations. Abbreviations are defined as follows: geocentric distance (Δ), heliocentric distance (r_H), phase angle (α), flux at 3.6 and 4.5 μm ($F_{3.6\mu\text{m}}$ and $F_{4.5\mu\text{m}}$, respectively), geometric albedo at 3.6 and 4.5 μm ($p_{3.6\mu\text{m}}$ and $p_{4.5\mu\text{m}}$, respectively).

Designation	Date (DD/MM/YY)	Δ (au)	r_H (au)	α ($^\circ$)	$F_{3.6\mu\text{m}}$ (μJy)	$F_{4.5\mu\text{m}}$ (μJy)	$p_{3.6\mu\text{m}}$	$p_{4.5\mu\text{m}}$
1993 SC	22-Aug-08	36.335	36.329	1.615	< 1.4	< 1.7	< 0.2	< 0.3
1995 SM ₅₅	25-Oct-10	38.109	38.572	1.372	2.6 ± 0.9	—	0.21 ± 0.08	—
	27-Oct-10	38.080	38.571	1.349	2.8 ± 0.6	—	0.23 ± 0.05	—
1995 TL ₈	03-Mar-11	43.670	44.145	1.155	2.0 ± 0.3	—	0.22 ± 0.05	—
1996 GQ ₂₁	07-Aug-07	40.254	40.656	1.329	3.8 ± 0.5	1.3	0.15 ± 0.03	< 0.08
1996 TK ₆₆	04-Sep-09	42.827	42.988	1.352	< 1.8	—	< 0.75	—
	08-Sep-09	42.761	42.988	1.337	< 2.3	—	< 1.0	—
1996 TO ₆₆	22-Dec-05	46.094	46.486	1.151	< 2.0	< 2.3	< 0.46	< 0.79
	25-Dec-05	46.142	46.486	1.173	< 1.1	< 2.2	< 0.24	< 0.76
1996 TP ₆₆	10-Mar-08	26.772	26.926	2.114	< 2.4	< 2.1	< 0.10	< 0.14
	11-Mar-08	26.789	26.926	2.119	< 2.4	< 1.8	< 0.10	< 0.11
1998 SM ₁₆₅	14-Mar-12	38.350	38.590	1.453	1.9 ± 0.4	—	0.09 ± 0.02	—
	17-Mar-12	38.403	38.593	1.468	2.1 ± 0.4	—	0.10 ± 0.02	—
1998 SN ₁₆₅	29-Jan-10	37.438	37.750	1.463	7.3 ± 1.1	4.4 ± 0.5	0.17 ± 0.03	0.16 ± 0.03
	03-Feb-10	37.520	37.750	1.495	3.0 ± 0.5	3.2 ± 0.6	0.07 ± 0.02	0.11 ± 0.03
1998 VG ₄₄	20-Nov-11	29.392	29.390	1.999	2.6 ± 1.2	—	0.06 ± 0.03	—
1999 CD ₁₅₈	12-Jun-12	46.828	47.229	1.121	2.0 ± 0.3	—	0.15 ± 0.04	—
1999 DE ₉	29-Dec-05	35.073	35.146	1.645	7.2 ± 0.9	12.9 ± 5.8	0.21 ± 0.04	0.57 ± 0.27
	26-Dec-05	35.121	35.143	1.649	4.9 ± 0.7	—	0.14 ± 0.03	—
1999 OJ ₄	06-Dec-09	37.460	37.989	1.322	0.6 ± 0.8	—	0.09 ± 0.14	—
	11-Dec-09	37.535	37.989	1.382	0.2 ± 0.5	—	0.03 ± 0.08	—
2000 CN ₁₀₅	26-Jun-10	46.157	46.571	1.137	< 2.5	< 1.5	< 0.34	< 0.30
	01-Jul-10	46.237	46.573	1.177	< 3.8	< 1.3	< 0.51	< 0.27
2000 GN ₁₇₁	10-Aug-06	28.344	28.372	2.066	2.9 ± 0.6	3.2 ± 1.0	0.17 ± 0.05	0.28 ± 0.10
	14-Aug-06	28.410	28.371	2.064	3.9 ± 0.6	2.7 ± 0.7	0.23 ± 0.06	0.24 ± 0.08
2000 GP ₁₈₃	04-Sep-09	36.807	36.989	1.563	3.0 ± 0.4	—	0.16 ± 0.04	—
	07-Sep-09	36.857	36.988	1.575	3.8 ± 0.5	—	0.20 ± 0.05	—
2000 OK ₆₇	13-Jan-10	40.175	40.318	1.427	< 1.7	< 1.7	< 0.31	< 0.45
	17-Jan-10	40.242	40.318	1.436	< 3.6	< 1.4	< 0.65	< 0.39
2000 PE ₃₀	14-Nov-07	37.812	38.210	1.415	2.5 ± 0.5	2.8 ± 0.7	0.14 ± 0.04	0.23 ± 0.07
	18-Nov-07	37.878	38.212	1.450	3.0 ± 0.5	2.4 ± 0.5	0.17 ± 0.04	0.20 ± 0.06
2000 QL ₂₅₁	29-Jan-10	39.041	39.281	1.434	2.0 ± 0.6	—	0.28 ± 0.10	—
	03-Feb-10	39.127	39.283	1.456	2.4 ± 0.7	—	0.34 ± 0.13	—
2000 YW ₁₃₄	14-Jan-12	44.380	44.525	1.299	4.0 ± 0.4	—	0.18 ± 0.03	—
	19-Jan-12	44.300	44.528	1.279	3.9 ± 0.5	—	0.17 ± 0.03	—

Table 5 *continued*

Table 5 (*continued*)

Designation	Date	Δ	r_H	α	$F_{3.6\mu m}$	$F_{4.5\mu m}$	$p_{3.6\mu m}$	$p_{4.5\mu m}$
	(DD/MM/YY)	(au)	(au)	($^\circ$)	(μ Jy)	(μ Jy)		
2001 CZ ₃₁	20-Jan-11	40.519	40.626	1.425	3.1 ± 0.4	—	0.22 ± 0.05	—
	24-Jan-11	40.451	40.625	1.413	3.1 ± 0.4	—	0.22 ± 0.05	—
2001 QC ₂₉₈	25-Dec-09	40.144	40.655	1.244	< 3.1	—	< 0.16	—
	28-Dec-09	40.189	40.655	1.278	1.1 ± 0.6	—	0.06 ± 0.03	—
2001 QF ₂₉₈	10-Sep-11	42.797	43.176	1.269	2.3 ± 0.8	—	0.08 ± 0.03	—
2001 QS ₃₂₂	23-Jan-10	42.111	42.357	1.330	0.7 ± 0.6	1.8	0.11 ± 0.11	< 0.46
	28-Jan-10	42.196	42.357	1.351	0.7 ± 0.5	1.8	0.12 ± 0.09	< 0.46
2001 QT ₃₂₂	23-Jan-10	36.704	37.031	1.485	< 3.2	< 2.4	< 0.43	< 0.49
	28-Jan-10	36.786	37.031	1.520	< 5.3	< 1.3	< 0.71	< 0.27
2001 RZ ₁₄₃	05-Sep-09	41.281	41.308	1.422	0.7 ± 0.6	—	0.20 ± 0.16	—
	10-Sep-09	41.197	41.308	1.416	1.8 ± 1.5	—	0.48 ± 0.41	—
2001 UR ₁₆₃	17-Aug-08	50.597	50.481	1.152	4.1 ± 0.4	3.5 ± 0.8	0.38 ± 0.06	0.51 ± 0.13
	21-Aug-08	50.533	50.484	1.160	5.7 ± 0.5	5.1 ± 0.7	0.54 ± 0.08	0.73 ± 0.14
2001 XD ₂₅₅	02-Jan-12	39.308	39.467	1.466	3.0 ± 0.5	—	0.14 ± 0.04	—
	06-Jan-12	39.240	39.466	1.448	3.2 ± 0.5	—	0.15 ± 0.04	—
2001 YH ₁₄₀	02-Jan-12	36.608	36.674	1.591	3.6 ± 0.7	—	0.10 ± 0.02	—
	06-Jan-12	36.541	36.675	1.581	2.4 ± 0.6	—	0.07 ± 0.02	—
2002 AW ₁₉₇	20-Dec-08	46.580	46.566	1.251	11.1 ± 0.5	10.0 ± 1.3	0.16 ± 0.02	0.22 ± 0.04
	24-Dec-08	46.512	46.564	1.250	11.2 ± 0.4	7.5 ± 1.6	0.16 ± 0.02	0.16 ± 0.04
2002 CY ₂₂₄	22-Jun-12	37.117	37.644	1.312	1.5 ± 0.3	—	0.37 ± 0.11	—
	26-Jun-12	37.178	37.646	1.365	1.8 ± 0.3	—	0.45 ± 0.12	—
2002 GV ₃₁	25-Jun-10	39.769	40.283	1.243	< 2.7	< 1.1	< 0.22	< 0.13
	26-Aug-16	39.684	40.117	1.312	< 1.4	—	< 0.1	—
	26-Aug-16	39.684	40.117	1.312	< 0.9	—	< 0.1	—
2002 KX ₁₄	16-Sep-08	39.242	39.486	1.447	5.7 ± 0.8	3.7 ± 1.6	0.12 ± 0.02	0.12 ± 0.05
	20-Sep-08	39.307	39.486	1.467	6.1 ± 1.0	4.4 ± 1.1	0.13 ± 0.03	0.14 ± 0.04
2002 TC ₃₀₂	15-Sep-08	46.572	46.822	1.222	4.9 ± 0.4	3.2 ± 0.4	0.12 ± 0.02	0.12 ± 0.02
	18-Sep-08	46.521	46.820	1.207	4.0 ± 0.7	4.6 ± 0.5	0.10 ± 0.02	0.18 ± 0.03
2002 TX ₃₀₀	17-Aug-08	41.362	41.397	1.417	2.7 ± 0.3	2.3 ± 0.5	0.14 ± 0.03	0.18 ± 0.04
	19-Aug-08	41.331	41.397	1.415	3.3 ± 0.6	1.9 ± 1.1	0.17 ± 0.04	0.15 ± 0.09
2002 UX ₂₅	18-Sep-08	41.517	41.866	1.328	9.4 ± 0.3	7.4 ± 1.3	0.11 ± 0.01	0.13 ± 0.03
	21-Sep-08	41.468	41.865	1.304	9.4 ± 0.5	7.7 ± 1.0	0.11 ± 0.01	0.13 ± 0.02
2002 VE ₉₅	22-Oct-05	27.347	28.093	1.449	6.6 ± 0.5	8.1 ± 0.8	0.11 ± 0.02	0.21 ± 0.04
	23-Oct-05	27.336	28.093	1.425	6.2 ± 0.4	6.2 ± 1.3	0.11 ± 0.02	0.16 ± 0.04
2002 VR ₁₂₈	23-Oct-11	37.695	37.924	1.518	4.5 ± 0.5	—	0.08 ± 0.01	—
	26-Oct-11	37.649	37.926	1.500	5.1 ± 0.6	—	0.09 ± 0.02	—
2002 VT ₁₃₀	30-Oct-09	42.611	42.862	1.335	< 1.5	—	< 0.09	—
	03-Nov-09	42.547	42.862	1.311	< 0.8	—	< 0.0	—
2002 WC ₁₉	11-Nov-11	41.996	42.008	1.400	3.7 ± 0.6	—	0.17 ± 0.03	—
	14-Nov-11	41.944	42.006	1.398	4.3 ± 0.5	—	0.20 ± 0.03	—

Table 5 *continued*

Table 5 (*continued*)

Designation	Date	Δ	r_H	α	$F_{3.6\mu m}$	$F_{4.5\mu m}$	$p_{3.6\mu m}$	$p_{4.5\mu m}$
	(DD/MM/YY)	(au)	(au)	($^\circ$)	(μ Jy)	(μ Jy)		
2002 XV ₉₃	19-Nov-11	39.465	39.514	1.486	5.9 ± 0.7	—	0.09 ± 0.02	—
	23-Nov-11	39.397	39.513	1.480	5.6 ± 0.7	—	0.08 ± 0.01	—
2003 AZ ₈₄	02-Jun-12	44.824	45.151	1.208	6.3 ± 0.5	3.8 ± 0.5	0.09 ± 0.01	0.08 ± 0.01
	05-Jun-12	44.871	45.150	1.227	5.2 ± 0.4	3.5 ± 0.6	0.07 ± 0.01	0.07 ± 0.01
2003 FE ₁₂₈	09-Sep-11	35.421	35.860	1.482	0.6 ± 0.5	—	0.13 ± 0.12	—
	13-Sep-11	35.483	35.860	1.525	1.3 ± 0.9	—	0.29 ± 0.22	—
2003 FY ₁₂₈	05-Mar-11	38.853	38.857	1.485	6.7 ± 0.8	5.2 ± 0.4	0.13 ± 0.02	0.16 ± 0.03
	09-Mar-11	38.786	38.859	1.482	4.4 ± 0.5	3.9 ± 0.4	0.09 ± 0.02	0.12 ± 0.02
2003 OP ₃₂	23-Nov-07	40.874	41.283	1.301	1.6 ± 0.5	2.5	0.11 ± 0.03	< 0.26
2003 QA ₉₂	06-Jan-10	37.346	37.432	1.549	2.4 ± 0.8	—	0.26 ± 0.11	—
2003 QR ₉₁	28-Nov-09	38.698	39.221	1.288	5.7 ± 0.8	—	0.30 ± 0.06	—
	03-Dec-09	38.775	39.222	1.345	6.2 ± 0.3	—	0.33 ± 0.05	—
2003 QW ₉₀	09-Apr-16	43.538	43.552	1.324	2.0 ± 0.6	—	0.08 ± 0.03	—
	10-Apr-16	43.555	43.552	1.324	2.7 ± 0.8	—	0.11 ± 0.03	—
2003 UT ₂₉₂	01-Nov-11	29.066	29.090	2.022	2.1 ± 0.4	—	0.08 ± 0.02	—
	03-Nov-11	29.033	29.089	2.021	1.9 ± 0.5	—	0.08 ± 0.02	—
2003 UY ₁₁₇	23-Oct-11	32.400	32.857	1.616	4.2 ± 0.6	—	0.15 ± 0.03	—
	26-Oct-11	32.356	32.858	1.576	4.2 ± 0.5	—	0.14 ± 0.03	—
2003 UZ ₄₁₃	29-Oct-10	42.091	42.575	1.228	6.6 ± 0.7	—	0.08 ± 0.01	—
	31-Oct-10	42.064	42.576	1.206	7.1 ± 0.7	—	0.09 ± 0.01	—
2003 VS ₂	19-Oct-07	36.017	36.441	1.479	12.3 ± 0.4	8.9 ± 1.0	0.14 ± 0.02	0.16 ± 0.03
	22-Oct-07	35.973	36.441	1.445	14.5 ± 0.4	10.2 ± 0.6	0.17 ± 0.02	0.18 ± 0.03
2004 EW ₉₅	04-Sep-11	27.080	27.330	2.085	5.7 ± 0.8	—	0.07 ± 0.02	—
	08-Sep-11	27.144	27.329	2.114	6.2 ± 0.6	—	0.08 ± 0.02	—
2004 GV ₉	12-Sep-10	39.070	39.190	1.488	10.8 ± 1.3	11.2 ± 1.4	0.10 ± 0.02	0.16 ± 0.03
	15-Sep-10	39.119	39.190	1.494	13.6 ± 2.3	11.8 ± 1.8	0.13 ± 0.03	0.17 ± 0.03
2004 NT ₃₃	29-Nov-10	37.769	38.297	1.317	9.2 ± 0.9	4.1 ± 0.6	0.19 ± 0.03	0.13 ± 0.03
	30-Nov-10	37.781	38.297	1.327	10.4 ± 2.1	6.2 ± 0.8	0.22 ± 0.05	0.20 ± 0.04
2004 PF ₁₁₅	14-Dec-10	40.935	41.425	1.242	4.5 ± 1.0	—	0.11 ± 0.03	—
	16-Dec-10	40.964	41.425	1.263	5.6 ± 0.8	—	0.13 ± 0.02	—
2004 PG ₁₁₅	18-Jul-11	36.908	36.994	1.568	4.1 ± 1.1	1.2	0.08 ± 0.03	< 0.04
	20-Jul-11	36.876	36.995	1.564	< 3.6	< 1.4	< 0.07	< 0.04
2004 PT ₁₀₇	01-Mar-16	38.293	38.223	1.514	3.4 ± 0.5	—	0.08 ± 0.02	—
	02-Mar-16	38.310	38.223	1.512	3.3 ± 0.5	—	0.08 ± 0.02	—
2004 TY ₃₆₄	18-Sep-11	39.464	39.418	1.487	6.1 ± 1.1	6.5 ± 1.0	0.10 ± 0.02	0.17 ± 0.03
	19-Sep-11	39.448	39.418	1.488	7.7 ± 0.7	5.5 ± 0.5	0.13 ± 0.02	0.14 ± 0.02
2004 UX ₁₀	18-Sep-10	38.881	38.957	1.506	5.4 ± 1.0	—	0.14 ± 0.03	—
	21-Sep-10	38.832	38.957	1.500	6.0 ± 0.9	—	0.16 ± 0.03	—
2004 VT ₇₅	19-Feb-11	37.393	37.847	1.368	1.4 ± 0.4	—	0.10 ± 0.04	—
	19-Feb-11	37.393	37.847	1.368	1.2 ± 0.4	—	0.08 ± 0.03	—

Table 5 *continued*

Table 5 (*continued*)

Designation	Date	Δ	r_H	α	$F_{3.6\mu m}$	$F_{4.5\mu m}$	$p_{3.6\mu m}$	$p_{4.5\mu m}$
	(DD/MM/YY)	(au)	(au)	($^\circ$)	(μ Jy)	(μ Jy)		
2004 XA ₁₉₂	19-Nov-10	35.683	35.729	1.643	11.7 ± 1.0	10.4 ± 1.1	0.31 ± 0.08	0.42 ± 0.12
	20-Nov-10	35.669	35.728	1.642	11.2 ± 1.2	11.1 ± 2.0	0.29 ± 0.08	0.45 ± 0.14
2005 CA ₇₉	07-Jan-11	37.164	37.297	1.552	2.2 ± 0.5	—	0.06 ± 0.02	—
	10-Jan-11	37.115	37.298	1.541	4.2 ± 0.6	—	0.11 ± 0.03	—
2005 GE ₁₈₇	01-Jun-16	28.627	28.609	2.009	1.6 ± 0.7	—	0.43 ± 0.21	—
	03-Jun-16	28.593	28.608	2.010	< 1.8	—	< 0.5	—
2005 RM ₄₃	25-Oct-10	35.261	35.454	1.634	8.0 ± 1.2	3.3 ± 0.4	0.11 ± 0.02	0.07 ± 0.01
	28-Oct-10	35.214	35.455	1.619	7.1 ± 1.1	2.0 ± 0.6	0.10 ± 0.02	0.04 ± 0.01
2005 RN ₄₃	18-Dec-10	40.166	40.681	1.244	12.2 ± 0.9	9.5 ± 0.5	0.13 ± 0.02	0.15 ± 0.02
	21-Dec-10	40.210	40.681	1.278	12.7 ± 0.6	10.5 ± 0.8	0.13 ± 0.02	0.17 ± 0.02
2005 RR ₄₃	25-Oct-10	38.558	38.794	1.481	< 3.7	< 2.1	< 0.17	< 0.15
	27-Oct-10	38.527	38.795	1.470	< 2.9	< 2.6	< 0.13	< 0.18
2005 RS ₄₃	03-Sep-10	42.284	42.334	1.385	3.2 ± 0.6	—	0.11 ± 0.03	—
	06-Sep-10	42.235	42.336	1.381	2.3 ± 0.6	—	0.08 ± 0.03	—
2005 TB ₁₉₀	07-Jan-11	45.925	46.330	1.155	3.1 ± 0.5	—	0.11 ± 0.02	—
2005 UQ ₅₁₃	10-Sep-10	48.478	48.672	1.188	4.3 ± 1.2	1.8 ± 0.6	0.17 ± 0.05	0.11 ± 0.04
	13-Sep-10	48.432	48.672	1.177	4.5 ± 0.7	4.5 ± 0.8	0.18 ± 0.03	0.28 ± 0.06
2006 QJ ₁₈₁	05-Nov-11	33.867	33.892	1.735	2.7 ± 0.4	—	1.27 ± 0.35	—
	08-Nov-11	33.814	33.890	1.732	2.6 ± 0.4	—	1.22 ± 0.34	—
2007 JF ₄₃	13-Apr-11	38.705	38.713	1.486	2.6 ± 0.5	—	0.09 ± 0.02	—
	17-Apr-11	38.634	38.711	1.483	3.1 ± 0.6	—	0.10 ± 0.03	—
2007 JH ₄₃	24-Apr-11	40.454	40.554	1.413	7.5 ± 0.8	—	0.14 ± 0.03	—
	28-Apr-11	40.385	40.554	1.402	7.4 ± 0.6	—	0.14 ± 0.02	—
2007 JJ ₄₃	21-Sep-11	40.996	41.527	1.213	5.2 ± 0.8	4.8 ± 1.1	0.11 ± 0.02	0.15 ± 0.04
	27-Sep-11	41.084	41.525	1.280	7.4 ± 0.7	3.1 ± 1.3	0.15 ± 0.03	0.10 ± 0.04
2007 OC ₁₀	29-Nov-10	35.034	35.525	1.454	4.1 ± 0.6	—	0.12 ± 0.02	—
2007 XV ₅₀	27-Oct-10	46.290	46.371	1.266	1.5 ± 0.5	—	0.04 ± 0.02	—
	31-Oct-10	46.224	46.372	1.257	4.3 ± 0.4	—	0.13 ± 0.02	—
2008 NW ₄	23-Nov-10	36.266	36.773	1.391	2.5 ± 0.6	—	0.07 ± 0.02	—
	26-Nov-10	36.310	36.773	1.427	1.9 ± 0.4	—	0.06 ± 0.01	—
2008 OG ₁₉	26-Nov-11	38.128	38.602	1.352	3.6 ± 0.5	—	0.07 ± 0.01	—
	29-Nov-11	38.173	38.602	1.384	4.7 ± 0.7	—	0.09 ± 0.02	—
2009 YG ₁₉	29-Dec-15	34.188	34.545	1.603	2.5 ± 0.4	—	0.09 ± 0.03	—
	31-Dec-15	34.158	34.546	1.583	2.2 ± 0.5	—	0.08 ± 0.02	—
2010 ER ₆₅	21-Mar-12	39.959	40.239	1.382	2.4 ± 0.5	—	0.07 ± 0.02	—
2010 ET ₆₅	22-Jul-11	39.168	39.637	1.304	3.3 ± 0.6	—	0.10 ± 0.02	—
2010 FD ₄₉	04-Sep-11	32.021	32.070	1.824	2.2 ± 0.4	—	0.08 ± 0.02	—
	06-Sep-11	32.054	32.069	1.826	3.5 ± 0.4	—	0.13 ± 0.03	—
2010 JC ₈₀	24-May-16	32.724	32.668	1.756	1.5 ± 0.7	2.3	0.05 ± 0.02	< 0.11
	25-May-16	32.707	32.668	1.758	< 2.1	< 1.5	< 0.06	< 0.07

Table 5 *continued*

Table 5 (*continued*)

Designation	Date	Δ	r_H	α	$F_{3.6\mu m}$	$F_{4.5\mu m}$	$p_{3.6\mu m}$	$p_{4.5\mu m}$
	(DD/MM/YY)	(au)	(au)	($^\circ$)	(μ Jy)	(μ Jy)		
Borasisi	26-Dec-07	41.286	41.362	1.401	1.6 ± 0.4	2.6	0.33 ± 0.08	< 0.80
	31-Dec-07	41.372	41.363	1.402	1.2 ± 0.5	3.3	0.24 ± 0.10	< 0.99
Chaos	19-Oct-07	41.522	41.848	1.338	4.2 ± 0.7	4.6 ± 0.7	0.06 ± 0.01	0.11 ± 0.02
Dziewanna	09-Sep-11	38.654	38.795	1.497	7.7 ± 0.8	6.1 ± 0.6	0.17 ± 0.03	0.20 ± 0.03
	10-Sep-11	38.668	38.794	1.500	7.3 ± 0.9	7.6 ± 0.9	0.16 ± 0.03	0.26 ± 0.05
Eris	17-Aug-08	96.747	96.751	0.606	7.6 ± 0.3	18.0 ± 0.9	0.21 ± 0.01	0.75 ± 0.06
	22-Aug-08	96.665	96.750	0.605	6.3 ± 0.3	17.9 ± 0.7	0.17 ± 0.01	0.75 ± 0.05
G!kún 'hòmdímà	25-Oct-10	44.688	44.870	1.293	3.5 ± 1.2	3.8 ± 0.7	0.07 ± 0.03	0.12 ± 0.03
	27-Oct-10	44.655	44.868	1.286	5.1 ± 6.6	7.5 ± 4.8	0.10 ± 0.13	0.23 ± 0.15
Gonggong	23-Jul-11	86.337	86.381	0.673	4.6 ± 0.9	—	0.28 ± 0.06	—
	30-Jul-11	86.223	86.385	0.667	2.9 ± 0.5	—	0.17 ± 0.03	—
	16-Dec-10	85.719	86.234	0.584	2.9 ± 0.5	—	0.17 ± 0.03	—
	20-Dec-10	85.781	86.236	0.605	3.1 ± 0.5	—	0.18 ± 0.03	—
Haumea	17-Mar-09	50.638	51.069	1.024	28.1 ± 0.7	8.2 ± 0.8	0.22 ± 0.02	0.10 ± 0.01
	19-Mar-09	50.611	51.069	1.009	27.0 ± 0.7	7.3 ± 0.5	0.21 ± 0.02	0.09 ± 0.01
Huya	10-Aug-06	28.954	29.013	2.019	14.3 ± 1.8	9.4 ± 1.6	0.09 ± 0.02	0.09 ± 0.02
	12-Aug-06	28.986	29.012	2.021	12.8 ± 1.5	6.7 ± 1.5	0.08 ± 0.02	0.07 ± 0.02
Lempo	23-Dec-05	30.558	30.964	1.721	8.2 ± 0.6	6.1 ± 1.9	0.09 ± 0.02	0.10 ± 0.03
	23-Dec-05	30.558	30.964	1.721	8.1 ± 1.0	6.0 ± 2.0	0.09 ± 0.02	0.10 ± 0.04
Makemake	16-Jun-08	51.610	52.059	1.000	18.7 ± 0.5	64.0 ± 0.7	0.12 ± 0.01	0.60 ± 0.06
	18-Jun-08	51.636	52.059	1.014	17.8 ± 0.4	61.4 ± 0.7	0.11 ± 0.01	0.58 ± 0.05
Orcus	27-Dec-05	47.359	47.711	1.144	10.2 ± 0.3	4.5 ± 0.5	0.10 ± 0.01	0.07 ± 0.01
	29-Dec-05	47.329	47.711	1.130	11.2 ± 0.5	4.0 ± 0.7	0.11 ± 0.01	0.06 ± 0.01
Quaoar	15-Sep-05	43.276	43.331	1.353	26.7 ± 0.8	13.2 ± 0.6	0.15 ± 0.02	0.11 ± 0.01
	18-Sep-05	43.326	43.331	1.354	27.3 ± 0.6	15.2 ± 1.7	0.15 ± 0.02	0.13 ± 0.02
Salacia	11-Oct-16	44.455	44.658	1.290	6.5 ± 0.6	4.8 ± 0.8	0.06 ± 0.01	0.06 ± 0.01
	12-Oct-16	44.439	44.658	1.286	7.9 ± 0.9	4.8 ± 0.5	0.07 ± 0.01	0.06 ± 0.01
	23-Jan-10	44.009	44.107	1.308	8.7 ± 1.0	—	0.07 ± 0.01	—
	26-Jan-10	44.057	44.107	1.312	8.5 ± 1.1	—	0.07 ± 0.01	—
Sedna	05-Feb-06	88.509	88.854	0.607	3.7 ± 0.3	3.9 ± 1.0	0.48 ± 0.05	0.76 ± 0.21
	09-Feb-06	88.569	88.850	0.620	2.8 ± 0.5	3.5 ± 0.6	0.36 ± 0.07	0.68 ± 0.12
Sila-Nunam	07-May-08	43.104	43.522	1.207	0.8 ± 0.3	1.3 ± 0.7	0.04 ± 0.02	0.10 ± 0.05
	09-May-08	43.135	43.522	1.225	2.0 ± 0.8	1.7 ± 0.5	0.11 ± 0.05	0.14 ± 0.04
	24-Jul-16	43.113	43.471	1.244	1.8 ± 0.7	—	0.10 ± 0.04	—
	25-Jul-16	43.129	43.471	1.252	2.1 ± 0.6	—	0.11 ± 0.04	—
Varda	20-May-11	47.281	47.588	1.158	10.6 ± 1.2	9.4 ± 0.7	0.15 ± 0.02	0.21 ± 0.03
	22-May-11	47.250	47.587	1.146	9.4 ± 1.0	8.3 ± 0.5	0.13 ± 0.02	0.18 ± 0.02
Varuna	24-Mar-06	42.791	43.307	1.141	7.7 ± 0.5	6.9 ± 0.8	0.11 ± 0.01	0.14 ± 0.02
	29-Mar-06	42.868	43.307	1.196	8.6 ± 0.5	6.0 ± 0.5	0.12 ± 0.01	0.13 ± 0.02

Table 6. Compilation of the physical properties used in this work for our sample. Geometric albedo in V -band (p_V), absolute magnitude in V -band (H_V) and diameter (D) have been compiled from “TNOs are cool” data base. In the case, the object was not study by this project (marked with the symbol †), we calculated the median value of p_V from this data base, with H_V from the Minor Planet Center; and we calculated D using the equation (1). For the Haumea family members for which “TNOs are cool” project only provided a lower limit (marked with *), we used the procedure but using a median value from those family members with known albedo ($p_{V,\text{Haumea}} = 0.58 \pm 0.26$). Taxonomy was taken [Fulchignoni et al. \(2008\)](#), with the exception of those marked with the symbol ‡, for which was taken from [Belskaya et al. \(2015\)](#). The spectral gradient was taken from [Peixinho et al. \(2015\)](#). Binariness was taken from the webpage of [Lowell Observatory](#); in this column, Haumea family members are labeled as HH. Dynamical classification (Dyn. Class.) following the work by [Gladman et al. \(2008\)](#). The orbital behavior (OB) is characterized as secure (S) or insecure (I).

Designation	p_V	H_V (mag)	D (km)	Taxonomy	S' (%/1000)	Binarity	Dyn. Class.	OB
1993 SC†	0.11 ± 0.09	7.00 ± 0.70	160.0 ± 50.0	RR	6.84 ± 4.88	No	Resonant	S
1995 SM ₅₅ *	0.58 ± 0.26	4.49 ± 0.03	220.0 ± 17.0	BBb?	1.27 ± 2.91	No	Inner Classical	S
1995 TL ₈	0.23 ± 0.19	5.29 ± 0.06	244.0 ± 82.0	RR	3.17 ± 6.08	Si	Hot Classical	I
1996 GQ ₂₁	0.13 ± 0.04	5.20 ± 0.30	349.0 ± 49.0	RR	4.74 ± 3.15	No	Detached	I
1996 TK ₆₆ †	0.11 ± 0.09	6.10 ± 0.60	120.0 ± 30.0	RR	8.62 ± 4.51	—	Cold Classical	S
1996 TO ₆₆ *	0.58 ± 0.26	4.81 ± 0.11	190.0 ± 17.0	BBb?	8.12 ± 8.43	HH	Hot Classical	S
1996 TP ₆₆	0.07 ± 0.06	7.51 ± 0.09	154.0 ± 33.0	RR	0.36 ± 4.74	No	Resonant	S
1998 SM ₁₆₅	0.08 ± 0.02	6.02 ± 0.08	291.0 ± 26.0	RR	9.02 ± 4.33	Si	Resonant	S
1998 SN ₁₆₅	0.06 ± 0.02	5.71 ± 0.09	393.0 ± 39.0	BB	8.24 ± 4.91	No	Inner Classical	S
1998 VG ₄₄	0.06 ± 0.03	6.67 ± 0.04	248.0 ± 43.0	IR	9.02 ± 3.08	No	Resonant	S
1999 CD ₁₅₈ †	0.11 ± 0.09	5.35 ± 0.67	340.0 ± 100.0	IR	6.73 ± 5.83	No	Hot Classical	S
1999 DE ₉	0.16 ± 0.04	5.16 ± 0.05	311.0 ± 32.0	IR	0.12 ± 2.25	No	Resonant	S
1999 OJ ₄ †	0.11 ± 0.09	7.10 ± 0.71	152.0 ± 50.0	RR	7.37 ± 3.21	Si	Inner Classical	S
2000 CN ₁₀₅	0.15 ± 0.07	5.20 ± 0.30	247.0 ± 63.0	RR	7.80 ± 5.69	No	Hot Classical	I
2000 GN ₁₇₁	0.21 ± 0.09	6.45 ± 0.34	147.0 ± 20.0	IR	3.88 ± 2.88	No	Resonant	S
2000 GP ₁₈₃ †	0.11 ± 0.09	6.00 ± 0.60	253.0 ± 70.0	BB	8.18 ± 3.45	No	Inner Classical	S
2000 OK ₆₇	0.17 ± 0.16	6.47 ± 0.13	164.0 ± 45.0	RR-U	0.14 ± 4.59	No	Hot Classical	S
2000 PE ₃₀ †	0.11 ± 0.09	5.90 ± 0.59	265.0 ± 72.0	BB	2.78 ± 4.11	No	Detached	S
2000 QL ₂₅₁ †	0.11 ± 0.09	6.80 ± 0.68	175.0 ± 55.0	BR	1.64 ± 2.46	Si	Resonant	S
2000 YW ₁₃₄ †	0.11 ± 0.09	4.88 ± 0.05	400.0 ± 10.0	IR	4.45 ± 3.51	Si	Resonant	S
2001 CZ _{31t} †	0.11 ± 0.09	5.90 ± 0.59	265.0 ± 72.0	BB	—	No	Hot Classical	S
2001 QC ₂₉₈	0.06 ± 0.03	6.26 ± 0.32	303.0 ± 30.0	BR	7.90 ± 4.21	Si	Resonant	S
2001 QF ₂₉₈	0.07 ± 0.02	5.43 ± 0.07	408.0 ± 44.0	BB	4.60 ± 4.64	No	Resonant	S
2001 QS ₃₂₂	0.10 ± 0.53	6.91 ± 0.68	186.0 ± 99.0	—	—	No	Cold Classical	S
2001 QT ₃₂₂	0.09 ± 0.42	7.29 ± 0.67	159.0 ± 47.0	—	5.58 ± 11.08	No	Inner Classical	S
2001 RZ ₁₄₃	0.19 ± 0.07	6.69 ± 0.13	140.0 ± 39.0	—	3.26 ± 7.24	Si	Hot Classical	I
2001 UR ₁₆₃	0.21 ± 0.08	4.10 ± 0.30	352.0 ± 85.0	RR-U	2.52 ± 4.66	No	Resonant	S
2001 XD ₂₅₅ †	0.11 ± 0.09	5.60 ± 0.56	304.0 ± 78.0	—	—	No	Resonant	S
2001 YH ₁₄₀	0.08 ± 0.05	5.80 ± 0.20	349.0 ± 81.0	IR	7.01 ± 3.18	No	Resonant	S
2002 AW ₁₉₇	0.11 ± 0.01	3.57 ± 0.05	768.0 ± 39.0	IR	3.45 ± 3.25	No	Hot Classical	S
2002 CY ₂₂₄ †	0.11 ± 0.09	6.10 ± 0.60	120.0 ± 30.0	RR	0.91 ± 2.70	—	Resonant	S
2002 GV ₃₁ †	0.11 ± 0.09	6.10 ± 0.60	240.0 ± 70.0	—	—	No	Hot Classical	S

Table 6 continued

Table 6 (*continued*)

Designation	p_V	H_V (mag)	D (km)	Taxonomy	S' (%/1000)	Binarity	Dyn. Class.	OB
2002 KX ₁₄	0.10 ± 0.01	4.86 ± 0.10	455.0 ± 27.0	—	3.82 ± 2.06	No	Inner Classical	S
2002 TC ₃₀₂	0.12 ± 0.05	4.17 ± 0.10	584.0 ± 105.0	RR	9.33 ± 2.40	No	Resonant	I
2002 TX ₃₀₀	0.76 ± 0.45	3.37 ± 0.05	323.0 ± 95.0	BBb	0.07 ± 1.39	HH	Hot Classical	S
2002 UX ₂₅	0.11 ± 0.01	3.87 ± 0.02	697.0 ± 24.0	IR	9.31 ± 2.44	Si	Hot Classical	S
2002 VE ₉₅	0.15 ± 0.02	5.70 ± 0.06	249.0 ± 13.0	RR	7.77 ± 3.71	No	Resonant	S
2002 VR ₁₂₈	0.05 ± 0.03	5.58 ± 0.37	448.0 ± 43.0	—	2.76 ± 2.06	No	Resonant	S
2002 VT ₁₃₀	0.10 ± 0.10	5.80 ± 0.30	324.0 ± 68.0	U	—	Si	Inner Classical	S
2002 WC ₁₉	0.17 ± 0.05	4.88 ± 0.07	348.0 ± 45.0	RR	9.36 ± 0.94	Si	Resonant	S
2002 XV ₉₃	0.04 ± 0.02	5.42 ± 0.46	549.0 ± 23.0	—	0.85 ± 2.06	No	Resonant	S
2003 AZ ₈₄	0.11 ± 0.02	3.74 ± 0.08	727.0 ± 66.0	BB	3.65 ± 3.46	Si	Resonant	S
2003 FE ₁₂₈ [†]	0.11 ± 0.09	6.30 ± 0.63	114.0 ± 12.0	—	—	Si	Resonant	S
2003 FY ₁₂₈ [†]	0.08 ± 0.01	5.09 ± 0.09	460.0 ± 21.0	IR	1.48 ± 3.46	No	Detached	S
2003 OP ₃₂	0.54 ± 0.15	4.10 ± 0.07	274.0 ± 47.0	BBb?	2.40 ± 3.75	HH	Hot Classical	S
2003 QA ₉₂ [†]	0.11 ± 0.09	6.70 ± 0.67	183.0 ± 57.0	—	5.97 ± 3.79	No	Inner Classical	I
2003 QR ₉₁	0.05 ± 0.04	6.55 ± 0.56	280.0 ± 30.0	—	—	Si	Hot Classical	S
2003 QW ₉₀ [†]	0.08 ± 0.03	5.00 ± 0.30	401.0 ± 63.0	RR	0.80 ± 3.43	No	Hot Classical	S
2003 UT ₂₉₂	0.07 ± 0.07	6.85 ± 0.68	185.0 ± 18.0	—	—	No	Resonant	S
2003 UY ₁₁₇	0.13 ± 0.04	5.70 ± 0.30	247.0 ± 30.0	IR	0.28 ± 0.94	No	Resonant	S
2003 UZ ₄₁₃	0.07 ± 0.02	5.70 ± 0.30	670.0 ± 84.0	—	6.64 ± 3.72	No	Resonant	S
2003 VS ₂	0.15 ± 0.06	4.11 ± 0.38	523.0 ± 35.0	—	1.71 ± 2.06	No	Resonant	S
2004 EW ₉₅	0.04 ± 0.02	6.69 ± 0.35	291.0 ± 25.0	BB	1.71 ± 2.06	No	Resonant	S
2004 GV ₉	0.08 ± 0.01	4.23 ± 0.10	680.0 ± 34.0	BR-IR	4.61 ± 2.91	No	Inner Classical	S
2004 NT ₃₃	0.12 ± 0.07	4.74 ± 0.11	423.0 ± 87.0	BB-BR	—	No	Hot Classical	S
2004 PF ₁₁₅	0.12 ± 0.04	4.54 ± 0.25	468.0 ± 49.0	—	—	No	Inner Classical	S
2004 PG ₁₁₅ [†]	0.11 ± 0.09	4.80 ± 0.48	410.0 ± 34.0	—	—	No	Detached	I
2004 PT ₁₀₇	0.03 ± 0.01	6.33 ± 0.11	400.0 ± 51.0	—	—	No	Inner Classical	S
2004 TY ₃₆₄	0.11 ± 0.02	4.52 ± 0.07	512.0 ± 40.0	BR-IR	0.78 ± 3.17	No	Inner Classical	S
2004 UX ₁₀	0.14 ± 0.04	4.75 ± 0.16	398.0 ± 39.0	IR-BR	0.23 ± 4.40	No	Inner Classical	S
2004 VT ₇₅ [†]	0.11 ± 0.09	6.20 ± 0.62	231.0 ± 66.0	—	—	No	Resonant	S
2004 XA ₁₉₂	0.26 ± 0.34	4.42 ± 0.63	339.0 ± 120.0	—	—	No	Detached	S
2005 CA ₇₉ [†]	0.11 ± 0.09	5.20 ± 0.52	365.0 ± 88.0	RR-IR	3.62 ± 2.46	No	Resonant	S
2005 GE ₁₈₇ [†]	0.11 ± 0.09	7.30 ± 0.70	70.0 ± 20.0	—	5.29 ± 6.49	No	Resonant	S
2005 RM ₄₃ [†]	0.11 ± 0.09	4.40 ± 0.44	460.0 ± 17.0	BB	3.01 ± 4.89	No	Detached	S
2005 RN ₄₃	0.11 ± 0.03	3.89 ± 0.05	679.0 ± 73.0	IR	—	No	Inner Classical	S
2005 RR ₄₃	0.44 ± 0.12	4.13 ± 0.08	300.0 ± 43.0	BB	3.89 ± 4.89	No	Hot Classical	S
2005 RS ₄₃ [†]	0.11 ± 0.09	5.00 ± 0.50	401.0 ± 93.0	BR	1.95 ± 2.46	No	Resonant	S
2005 TB ₁₉₀	0.15 ± 0.05	4.40 ± 0.11	464.0 ± 62.0	IR	8.63 ± 1.89	No	Detached	S
2005 UQ ₅₁₃	0.20 ± 0.08	3.87 ± 0.14	498.0 ± 75.0	—	—	No	Hot Classical	S
2006 QJ ₁₈₁ [†]	0.11 ± 0.09	7.20 ± 0.70	73.0 ± 20.0	BR-IR	4.76 ± 4.04	No	Resonant	S
2007 JF ₄₃ [†]	0.11 ± 0.09	5.30 ± 0.53	349.0 ± 85.0	—	—	No	Resonant	S

Table 6 *continued*

Table 6 (*continued*)

Designation	p_V	H_V	D	Taxonomy	S'	Binarity	Dyn. Class.	OB
		(mag)	(km)		(%/1000)			
2007 JH ₄₃ [†]	0.11 ± 0.09	4.50 ± 0.45	504.0 ± 105.0	—	—	No	Resonant	I
2007 JJ ₄₃ [†]	0.11 ± 0.09	4.50 ± 0.45	504.0 ± 105.0	IR	9.12 ± 1.33	No	Hot Classical	I
2007 OC ₁₀	0.13 ± 0.04	5.43 ± 0.10	309.0 ± 37.0	IR	—	No	Detached	S
2007 XV ₅₀ [†]	0.11 ± 0.09	4.40 ± 0.44	528.0 ± 10.0	—	—	No	Hot Classical	S
2008 NW ₄ [†]	0.11 ± 0.09	5.40 ± 0.54	333.0 ± 83.0	—	—	No	Detached	S
2008 OG ₁₉ [†]	0.11 ± 0.09	4.70 ± 0.47	460.0 ± 100.0	IR-RR	8.30 ± 0.94	No	Detached	I
2009 YG ₁₉ [†]	0.11 ± 0.09	5.90 ± 0.59	264.0 ± 72.0	—	—	No	Resonant	S
2010 ER ₆₅ [†]	0.11 ± 0.09	5.00 ± 0.50	401.0 ± 92.0	—	—	No	Detached	S
2010 ET ₆₅ [†]	0.11 ± 0.09	5.10 ± 0.51	383.0 ± 90.0	—	—	No	Detached	S
2010 FD ₄₉ [†]	0.11 ± 0.09	6.20 ± 0.62	231.0 ± 66.0	—	—	No	Resonant	S
2010 JC ₈₀ [†]	0.11 ± 0.09	5.90 ± 0.60	265.0 ± 73.0	—	—	No	Resonant	S
Borasisi	0.24 ± 0.44	6.21 ± 0.07	163.0 ± 66.0	IR-RR	34.20 ± 3.90	Si	Cold Classical	I
Chaos	0.05 ± 0.03	5.00 ± 0.06	600.0 ± 140.0	IR	24.58 ± 2.94	No	Hot Classical	S
Dziewanna	0.30 ± 0.11	3.80 ± 0.10	433.0 ± 64.0	—	—	No	Resonant	S
Eris	0.96 ± 0.04	-1.12 ± 0.03	2326.0 ± 12.0	BBb	1.85 ± 3.08	Si	Detached	S
G'kún 'hòmdímà	0.17 ± 0.06	3.69 ± 0.10	599.0 ± 77.0	U	0.85 ± 3.17	Si	Detached	S
Gonggong	0.13 ± 0.01	2.34 ± 0.05	1252.0 ± 43.0	—	—	No	Resonant	S
Haumea	0.80 ± 0.10	0.43 ± 0.11	1239.0 ± 68.0	BBb	-1.53 ± 3.34	HH	Hot Classical	I
Huya	0.08 ± 0.00	5.04 ± 0.03	458.0 ± 9.0	IR	21.89 ± 4.59	Si	Resonant	S
Lempo	0.08 ± 0.01	5.41 ± 0.10	393.0 ± 26.0	RR	2.06 ± 2.34	Si	Resonant	S
Makemake	0.77 ± 0.02	0.14 ± 0.05	1430.0 ± 9.0	BBb-U	8.32 ± 1.65	Xx	Hot Classical	S
Orcus	0.23 ± 0.02	2.30 ± 0.03	958.0 ± 22.0	BB	1.92 ± 2.47	Si	Resonant	S
Quaoar [‡]	0.13 ± 0.01	2.73 ± 0.06	1073.0 ± 37.0	RR	63.39 ± 1.34	Si	Hot Classical	S
Salacia	0.04 ± 0.00	4.25 ± 0.05	901.0 ± 45.0	BB	—	Si	Inner Classical	I
Sedna	0.41 ± 0.39	1.83 ± 0.05	906.0 ± 314.0	RR	37.31 ± 7.28	No	Detached	S
Sila-Nunam	0.09 ± 0.03	5.56 ± 0.04	343.0 ± 42.0	RR	8.39 ± 3.34	Si	Cold Classical	S
Varda	0.10 ± 0.02	3.61 ± 0.05	792.0 ± 91.0	IR	17.11 ± 7.64	Si	Hot Classical	S
Varuna	0.13 ± 0.04	3.76 ± 0.04	668.0 ± 154.0	IR	24.07 ± 1.91	No	Hot Classical	S

Table 7. Visible and near-infrared colors compilation for our sample. Visible colors are taken from [Peixinho et al. \(2015\)](#) and infrared colors are taken from [Fulchignoni et al. \(2008\)](#). For those objects without VNIR colors but taxonomic classification, we took the average color for the correspondent taxonomy (*). See table's footnote and section 3 for exceptions.

Designation	$B - V$	$V - R$	$V - I$	$V - J$	$V - H$	V-K
	(mag)	(mag)	(mag)	(mag)	(mag)	(mag)
1993 SC	1.04 ± 0.13	0.70 ± 0.08	1.45 ± 0.09	2.42 ± 0.07	2.82 ± 0.21	2.78 ± 0.20
1995 SM ₅₅	0.65 ± 0.03	0.37 ± 0.05	0.70 ± 0.05	1.07 ± 0.05	0.59 ± 0.06	0.49 ± 0.05
1995 TL ₈	1.01 ± 0.16	0.62 ± 0.09	1.14 ± 0.21	2.42 ± 0.05	2.82 ± 0.09	2.8 ± 0.09

Table 7 *continued*

Table 7 (*continued*)

Designation	$B - V$	$V - R$	$V - I$	$V - J$	$V - H$	V-K
	(mag)	(mag)	(mag)	(mag)	(mag)	(mag)
1996 GQ ₂₁	1.00 ± 0.06	0.70 ± 0.05	1.42 ± 0.07	2.39 ± 0.04	2.88 ± 0.04	3.03 ± 0.08
1996 TK ₆₆ [*]	0.99 ± 0.06	0.68 ± 0.07	1.28 ± 0.13	2.26 ± 0.18	2.66 ± 0.22	2.66 ± 0.25
1996 TO ₆₆	0.68 ± 0.07	0.39 ± 0.15	0.74 ± 0.07	$1. \pm 0.1$	0.79 ± 0.2	1.6 ± 0.18
1996 TP ₆₆	1.03 ± 0.11	0.66 ± 0.07	1.29 ± 0.11	2.26 ± 0.08	2.42 ± 0.12	2.44 ± 0.11
1998 SM ₁₆₅	0.98 ± 0.08	0.64 ± 0.07	1.34 ± 0.06	2.36 ± 0.01	2.91 ± 0.02	2.96 ± 0.07
1998 SN ₁₆₅ [*]	0.75 ± 0.08	0.43 ± 0.06	0.98 ± 0.17	1.27 ± 0.05	1.27 ± 0.49	1.33 ± 0.6
1998 VG ₄₄	0.95 ± 0.05	0.56 ± 0.04	1.17 ± 0.11	1.81 ± 0.01	2.21 ± 0.01	2.23 ± 0.01
1999 CD ₁₅₈	0.84 ± 0.07	0.53 ± 0.09	1.10 ± 0.07	1.86 ± 0.07	2.3 ± 0.07	2.33 ± 0.08
1999 DE ₉	0.93 ± 0.10	0.58 ± 0.04	1.16 ± 0.12	1.84 ± 0.04	2.17 ± 0.05	2.19 ± 0.05
1999 OJ ₄ [*]	0.99 ± 0.08	0.68 ± 0.05	1.22 ± 0.10	2.26 ± 0.18	2.66 ± 0.22	2.66 ± 0.25
2000 CN ₁₀₅ [*]	1.06 ± 0.10	0.61 ± 0.10	1.35 ± 0.11	1.69 ± 0.13	2.13 ± 0.12	2.29 ± 0.11
2000 GN ₁₇₁	0.96 ± 0.06	0.60 ± 0.04	1.14 ± 0.17	1.84 ± 0.08	2.21 ± 0.14	2.38 ± 0.14
2000 GP ₁₈₃ [*]	0.77 ± 0.04	0.45 ± 0.05	0.91 ± 0.08	1.22 ± 0.23	1.27 ± 0.49	1.33 ± 0.6
2000 OK ₆₇	0.82 ± 0.12	0.59 ± 0.07	1.14 ± 0.09	2.42 ± 0.08	2.88 ± 0.11	2.92 ± 0.12
2000 PE ₃₀	0.75 ± 0.07	0.37 ± 0.08	0.76 ± 0.09	1.65 ± 0.08	2.09 ± 0.08	2.32 ± 0.11
2000 QL ₂₅₁ [*]	0.87 ± 0.06	0.49 ± 0.04	0.93 ± 0.09	1.69 ± 0.13	2.13 ± 0.12	2.29 ± 0.11
2000 YW ₁₃₄	0.92 ± 0.05	0.48 ± 0.06	1.08 ± 0.07	1.68 ± 0.12	2.02 ± 0.16	2.18 ± 0.16
2001 CZ ₃₁ [§]	0.6 ± 0.15	0.5 ± 0.1	0.8 ± 0.15	1.53 ± 0.1	2.08 ± 0.14	2.24 ± 0.14
2001 QC ₂₉₈ [*]	0.66 ± 0.07	0.37 ± 0.07	0.85 ± 0.12	1.69 ± 0.13	2.13 ± 0.12	2.29 ± 0.11
2001 QF ₂₉₈	0.67 ± 0.07	0.39 ± 0.06	0.89 ± 0.19	1.3 ± 0.1	1.53 ± 0.14	1.69 ± 0.15
2001 QS ₃₂₂	—	—	—	—	—	—
2001 QT ₃₂₂	0.71 ± 0.06	0.53 ± 0.12	—	—	—	—
2001 RZ ₁₄₃	1.08 ± 0.14	0.51 ± 0.13	1.00 ± 0.16	—	—	—
2001 UR ₁₆₃	1.29 ± 0.11	0.86 ± 0.07	1.50 ± 0.12	2.37 ± 0.06	2.86 ± 0.08	2.66 ± 0.25
2001 XD ₂₅₅	—	—	—	—	—	—
2001 YH ₁₄₀ [*]	0.97 ± 0.08	0.56 ± 0.07	1.07 ± 0.07	1.86 ± 0.06	2.21 ± 0.09	2.31 ± 0.09
2002 AW ₁₉₇	0.88 ± 0.15	0.59 ± 0.04	1.21 ± 0.17	1.82 ± 0.06	2.15 ± 0.08	2.38 ± 0.10
2002 CY ₂₂₄ [*]	1.12 ± 0.10	0.67 ± 0.04	1.32 ± 0.06	2.26 ± 0.18	2.66 ± 0.22	2.66 ± 0.25
2002 GV ₃₁	—	—	—	—	—	—
2002 KX ₁₄	1.05 ± 0.03	0.61 ± 0.02	1.21 ± 0.16	—	—	—
2002 TC ₃₀₂ [*]	1.09 ± 0.06	0.65 ± 0.04	1.30 ± 0.06	2.26 ± 0.18	2.66 ± 0.22	2.66 ± 0.25
2002 TX ₃₀₀ [♣]	0.70 ± 0.09	0.36 ± 0.02	0.68 ± 0.12	1.0 ± 0.6	0.7 ± 0.7	0.7 ± 0.7
2002 UX ₂₅	0.95 ± 0.13	0.56 ± 0.04	1.05 ± 0.15	1.82 ± 0.09	2.22 ± 0.1	2.22 ± 0.11
2002 VE ₉₅ [*]	1.07 ± 0.14	0.72 ± 0.05	1.38 ± 0.15	2.26 ± 0.18	2.66 ± 0.22	2.66 ± 0.25
2002 VR ₁₂₈	0.94 ± 0.03	0.60 ± 0.02	—	—	—	—
2002 VT ₁₃₀ [*]	1.45 ± 0.21	0.56 ± 0.1	1.19 ± 0.13	—	—	—
2002 WC ₁₉ [*]	1.14 ± 0.02	0.65 ± 0.01	1.30 ± 0.04	2.26 ± 0.18	2.66 ± 0.22	2.66 ± 0.25
2002 XV ₉₃	0.72 ± 0.02	0.37 ± 0.02	—	—	—	—
2003 AZ ₈₄	0.65 ± 0.04	0.38 ± 0.04	0.83 ± 0.12	1.46 ± 0.1	1.48 ± 0.14	1.39 ± 0.16
2003 FE ₁₂₈	—	—	—	—	—	—

Table 7 *continued*

Table 7 (*continued*)

Designation	$B - V$	$V - R$	$V - I$	$V - J$	$V - H$	V-K
	(mag)	(mag)	(mag)	(mag)	(mag)	(mag)
2003 FY ₁₂₈	1.05 ± 0.03	0.60 ± 0.05	1.14 ± 0.09	1.64 ± 0.06	—	—
2003 OP ₃₂	0.70 ± 0.05	0.39 ± 0.06	0.76 ± 0.06	—	—	—
2003 QA ₉₂	1.04 ± 0.03	0.63 ± 0.04	—	—	—	—
2003 QR ₉₁	—	—	—	—	—	—
2003 QW ₉₀ *	1.11 ± 0.07	0.67 ± 0.06	1.32 ± 0.08	1.98 ± 0.16	2.66 ± 0.22	2.66 ± 0.25
2003 UT ₂₉₂	—	—	—	—	—	—
2003 UY ₁₁₇ *	0.97 ± 0.02	0.56 ± 0.01	1.15 ± 0.02	1.86 ± 0.06	2.21 ± 0.09	2.31 ± 0.09
2003 UZ ₄₁₃	—	0.45 ± 0.06	0.82 ± 0.06	—	—	—
2003 VS ₂	0.93 ± 0.02	0.59 ± 0.02	—	—	—	—
2004 EW ₉₅ [†] *	0.70 ± 0.02	0.38 ± 0.02	—	1.22 ± 0.23	1.27 ± 0.49	1.33 ± 0.6
2004 GV ₉ *	0.90 ± 0.06	0.52 ± 0.03	1.15 ± 0.03	1.77 ± 0.14	2.17 ± 0.14	2.3 ± 0.14
2004 NT ₃₃ *	0.71 ± 0.09	0.42 ± 0.05	0.85 ± 0.09	1.45 ± 0.26	1.7 ± 0.5	1.81 ± 0.61
2004 PF ₁₁₅	—	—	—	—	—	—
2004 PG ₁₁₅	—	—	—	—	—	—
2004 PT ₁₀₇	—	—	—	—	—	—
2004 TY ₃₆₄ *	0.92 ± 0.18	0.60 ± 0.05	1.03 ± 0.18	1.77 ± 0.14	2.17 ± 0.14	2.3 ± 0.14
2004 UX ₁₀ *	0.95 ± 0.02	0.58 ± 0.05	—	1.77 ± 0.14	2.17 ± 0.14	2.3 ± 0.14
2004 VT ₇₅	—	—	—	—	—	—
2004 XA ₁₉₂	—	—	—	—	—	—
2005 CA ₇₉ *	1.12 ± 0.05	0.64 ± 0.04	1.17 ± 0.05	2.06 ± 0.18	2.43 ± 0.22	2.48 ± 0.25
2005 GE ₁₈₇	0.98 ± 0.13	0.76 ± 0.10	1.31 ± 0.14	—	—	—
2005 RM ₄₃ *	0.59 ± 0.04	0.40 ± 0.05	0.73 ± 0.04	1.22 ± 0.23	1.27 ± 0.49	1.33 ± 0.6
2005 RN ₄₃ *	0.91 ± 0.04	0.58 ± 0.04	1.14 ± 0.07	1.86 ± 0.06	2.21 ± 0.09	2.31 ± 0.09
2005 RR ₄₃ *	0.79 ± 0.08	0.41 ± 0.05	0.69 ± 0.08	1.22 ± 0.23	1.27 ± 0.49	1.33 ± 0.6
2005 RS ₄₃ *	0.87 ± 0.06	0.50 ± 0.04	0.97 ± 0.05	1.69 ± 0.13	2.13 ± 0.12	2.29 ± 0.11
2005 TB ₁₉₀ *	0.98 ± 0.04	0.56 ± 0.03	1.11 ± 0.04	1.86 ± 0.06	2.21 ± 0.09	2.31 ± 0.09
2005 UQ ₅₁₃	—	—	—	—	—	—
2006 QJ ₁₈₁ *	0.95 ± 0.11	0.54 ± 0.08	1.02 ± 0.09	2.26 ± 0.18	2.66 ± 0.22	2.66 ± 0.25
2007 JF ₄₃	—	—	—	—	—	—
2007 JH ₄₃	—	—	—	—	—	—
2007 JJ ₄₃ *	1.02 ± 0.03	0.59 ± 0.02	1.09 ± 0.03	1.86 ± 0.06	2.21 ± 0.09	2.31 ± 0.09
2007 OC ₁₀ [¶] *	0.88 ± 0.01	0.55 ± 0.01	1.02 ± 0.01	1.86 ± 0.06	2.21 ± 0.09	2.31 ± 0.09
2007 XV ₅₀	—	—	—	—	—	—
2008 NW ₄	—	—	—	—	—	—
2008 OG ₁₉ *	0.94 ± 0.02	0.53 ± 0.01	1.12 ± 0.02	2.06 ± 0.18	2.43 ± 0.22	2.48 ± 0.25
2009 YG ₁₉ [†]	1 ± 0.04	0.61 ± 0.04	—	—	—	—
2010 ER ₆₅	—	—	—	—	—	—
2010 ET ₆₅	—	—	—	—	—	—
2010 FD ₄₉	—	—	—	—	—	—
2010 JC ₈₀	—	—	—	—	—	—

Table 7 *continued*

Table 7 (*continued*)

Designation	$B - V$	$V - R$	$V - I$	$V - J$	$V - H$	V-K
	(mag)	(mag)	(mag)	(mag)	(mag)	(mag)
Borasisi	0.86 ± 0.09	0.71 ± 0.06	1.29 ± 0.07	2.01 ± 0.07	2.49 ± 0.11	2.59 ± 0.09
Chaos	0.95 ± 0.05	0.60 ± 0.04	1.24 ± 0.06	1.89 ± 0.03	2.29 ± 0.03	2.32 ± 0.04
Dziewanna	—	—	—	—	—	—
Eris	0.74 ± 0.06	0.39 ± 0.05	0.77 ± 0.06	1.01 ± 0.02	0.72 ± 0.04	0.32 ± 0.05
G!kunhomdima	—	0.62 ± 0.05	1.09 ± 0.05	—	—	—
Gonggong [*]	0.94 ± 0.11	0.65 ± 0.02	1.33 ± 0.14	2.18 ± 0.06	2.5 ± 0.1	2.5 ± 0.1
Haumea	0.65 ± 0.04	0.34 ± 0.06	0.68 ± 0.04	1.05 ± 0.02	1.01 ± 0.04	0.94 ± 0.05
Huya	0.95 ± 0.05	0.57 ± 0.09	1.19 ± 0.06	1.95 ± 0.02	2.27 ± 0.05	2.37 ± 0.06
Lempo	0.99 ± 0.13	0.69 ± 0.03	1.30 ± 0.13	2.32 ± 0.01	2.7 ± 0.03	2.7 ± 0.02
Makemake [♣]	0.82 ± 0.05	0.49 ± 0.02	0.81 ± 0.05	0.98 ± 0.09	0.85 ± 0.1	0.57 ± 0.26
Orcus	0.62 ± 0.08	0.38 ± 0.04	0.75 ± 0.10	1.08 ± 0.04	1.21 ± 0.04	1.25 ± 0.04
Quaoar [♣]	0.94 ± 0.11	0.65 ± 0.02	1.33 ± 0.14	2.18 ± 0.06	2.5 ± 0.1	2.5 ± 0.1
Salacia ^{†*}	0.66 ± 0.06	0.4 ± 0.04	0.87 ± 0.01	1.22 ± 0.23	1.27 ± 0.49	1.33 ± 0.6
Sedna	1.17 ± 0.12	0.73 ± 0.12	1.39 ± 0.15	2.32 ± 0.06	2.61 ± 0.06	2.66 ± 0.07
Sila-Nunam	1.08 ± 0.07	0.67 ± 0.05	1.27 ± 0.07	2.06 ± 0.03	2.44 ± 0.08	2.48 ± 0.09
Varda	—	0.58 ± 0.11	1.00 ± 0.17	1.86 ± 0.06	2.21 ± 0.09	2.31 ± 0.09
Varuna	0.93 ± 0.13	0.60 ± 0.04	1.23 ± 0.13	1.99 ± 0.01	2.55 ± 0.07	2.52 ± 0.08

[†] Tegler et al. (2016)

[‡] Peixinho et al. (2015) & Belskaya et al. (2015)

[§] Fulchignoni et al. (2008)

[¶] Perna et al. (2013)

[♣] From its spectrum

Table 8. Visible and near-infrared colors compilation for our sample. Abbreviations are defined as follows: albedo at wavelengths: B , R , I , J , H and K (p_B , p_R , p_I , p_J , p_H and p_K , respectively). Albedo in V -band is shown in table 6 together with the physical properties of each object.

Designation	p_B	p_R	p_I	p_J	p_H	p_B
1993 SC	0.08 ± 0.02	0.15 ± 0.03	0.22 ± 0.05	0.40 ± 0.06	0.42 ± 0.20	0.38 ± 0.18
1995 SM ₅₅	0.59 ± 0.04	0.59 ± 0.07	0.59 ± 0.07	0.60 ± 0.07	0.29 ± 0.04	0.25 ± 0.03
1995 TL ₈	0.17 ± 0.06	0.29 ± 0.06	0.35 ± 0.17	0.83 ± 0.10	0.89 ± 0.18	0.82 ± 0.17
1996 GQ ₂₁	0.09 ± 0.01	0.17 ± 0.02	0.25 ± 0.04	0.44 ± 0.04	0.52 ± 0.05	0.56 ± 0.10
1996 TK ₆₆	0.08 ± 0.01	0.15 ± 0.02	0.19 ± 0.06	0.34 ± 0.14	0.36 ± 0.18	0.34 ± 0.20
1996 TO ₆₆	0.57 ± 0.09	0.60 ± 0.21	0.61 ± 0.10	0.56 ± 0.13	0.34 ± 0.16	0.68 ± 0.28
1996 TP ₆₆	0.05 ± 0.01	0.10 ± 0.02	0.13 ± 0.03	0.23 ± 0.04	0.20 ± 0.05	0.19 ± 0.05
1998 SM ₁₆₅	0.06 ± 0.01	0.11 ± 0.02	0.15 ± 0.02	0.28 ± 0.01	0.35 ± 0.02	0.34 ± 0.06
1998 SN ₁₆₅	0.06 ± 0.01	0.06 ± 0.01	0.08 ± 0.03	0.07 ± 0.01	0.06 ± 0.06	0.06 ± 0.08
1998 VG ₄₄	0.05 ± 0.01	0.08 ± 0.01	0.10 ± 0.02	0.13 ± 0.00	0.14 ± 0.00	0.13 ± 0.00

Table 8 *continued*

Table 8 (*continued*)

Designation	p_B	p_R	p_I	p_J	p_H	p_B
1999 CD ₁₅₈	0.09 ± 0.02	0.13 ± 0.03	0.16 ± 0.03	0.24 ± 0.04	0.26 ± 0.04	0.25 ± 0.05
1999 DE ₉	0.13 ± 0.03	0.20 ± 0.02	0.25 ± 0.07	0.34 ± 0.03	0.34 ± 0.04	0.33 ± 0.04
1999 OJ ₄	0.08 ± 0.02	0.15 ± 0.02	0.18 ± 0.04	0.34 ± 0.14	0.36 ± 0.18	0.34 ± 0.20
2000 CN ₁₀₅	0.11 ± 0.02	0.19 ± 0.04	0.28 ± 0.07	0.28 ± 0.08	0.31 ± 0.08	0.34 ± 0.09
2000 GN ₁₇₁	0.16 ± 0.02	0.27 ± 0.02	0.33 ± 0.13	0.45 ± 0.08	0.47 ± 0.15	0.52 ± 0.17
2000 GP ₁₈₃	0.10 ± 0.01	0.12 ± 0.01	0.13 ± 0.02	0.13 ± 0.07	0.10 ± 0.11	0.10 ± 0.14
2000 OK ₆₇	0.15 ± 0.04	0.21 ± 0.03	0.26 ± 0.05	0.61 ± 0.11	0.69 ± 0.17	0.67 ± 0.19
2000 PE ₃₀	0.10 ± 0.02	0.11 ± 0.02	0.12 ± 0.02	0.19 ± 0.04	0.22 ± 0.04	0.25 ± 0.06
2000 QL ₂₅₁	0.09 ± 0.01	0.12 ± 0.01	0.14 ± 0.03	0.20 ± 0.06	0.22 ± 0.06	0.25 ± 0.06
2000 YW ₁₃₄	0.09 ± 0.01	0.12 ± 0.02	0.16 ± 0.03	0.20 ± 0.06	0.20 ± 0.07	0.22 ± 0.08
2001 CZ _{31t}	0.12 ± 0.04	0.13 ± 0.03	0.12 ± 0.04	0.17 ± 0.04	0.21 ± 0.07	0.23 ± 0.08
2001 QC ₂₉₈	0.06 ± 0.01	0.06 ± 0.01	0.07 ± 0.02	0.11 ± 0.03	0.12 ± 0.03	0.14 ± 0.03
2001 QF ₂₉₈	0.07 ± 0.01	0.07 ± 0.01	0.09 ± 0.04	0.09 ± 0.02	0.08 ± 0.03	0.09 ± 0.03
2001 QS ₃₂₂	—	—	—	—	—	—
2001 QT ₃₂₂	0.08 ± 0.01	0.10 ± 0.03	—	—	—	—
2001 RZ ₁₄₃	0.13 ± 0.04	0.22 ± 0.07	0.25 ± 0.09	—	—	—
2001 UR ₁₆₃	0.12 ± 0.03	0.33 ± 0.05	0.44 ± 0.12	0.72 ± 0.10	0.83 ± 0.15	0.65 ± 0.38
2001 XD ₂₅₅	—	—	—	—	—	—
2001 YH ₁₄₀	0.06 ± 0.01	0.10 ± 0.02	0.11 ± 0.02	0.17 ± 0.02	0.17 ± 0.04	0.18 ± 0.04
2002 AW ₁₉₇	0.09 ± 0.03	0.14 ± 0.01	0.18 ± 0.07	0.23 ± 0.03	0.23 ± 0.04	0.27 ± 0.06
2002 CY ₂₂₄	0.07 ± 0.02	0.15 ± 0.01	0.20 ± 0.03	0.34 ± 0.14	0.36 ± 0.18	0.34 ± 0.20
2002 GV ₃₁	—	—	—	—	—	—
2002 KX ₁₄	0.07 ± 0.00	0.12 ± 0.01	0.16 ± 0.06	—	—	—
2002 TC ₃₀₂	0.08 ± 0.01	0.15 ± 0.01	0.20 ± 0.03	0.36 ± 0.15	0.38 ± 0.19	0.36 ± 0.21
2002 TX ₃₀₀	0.74 ± 0.15	0.76 ± 0.04	0.75 ± 0.21	0.74 ± 1.02	0.41 ± 0.67	0.39 ± 0.63
2002 UX ₂₅	0.08 ± 0.02	0.13 ± 0.01	0.15 ± 0.05	0.22 ± 0.05	0.24 ± 0.05	0.22 ± 0.06
2002 VE ₉₅	0.10 ± 0.03	0.21 ± 0.02	0.28 ± 0.10	0.46 ± 0.19	0.49 ± 0.25	0.47 ± 0.27
2002 VR ₁₂₈	0.04 ± 0.00	0.06 ± 0.00	—	—	—	—
2002 VT ₁₃₀	0.05 ± 0.02	0.12 ± 0.03	0.15 ± 0.05	—	—	—
2002 WC ₁₉	0.11 ± 0.01	0.22 ± 0.01	0.29 ± 0.03	0.52 ± 0.21	0.55 ± 0.28	0.52 ± 0.30
2002 XV ₉₃	0.04 ± 0.00	0.04 ± 0.00	—	—	—	—
2003 AZ ₈₄	0.11 ± 0.01	0.11 ± 0.01	0.12 ± 0.03	0.16 ± 0.04	0.12 ± 0.04	0.10 ± 0.04
2003 FE ₁₂₈	—	—	—	—	—	—
2003 FY ₁₂₈	0.06 ± 0.00	0.10 ± 0.01	0.12 ± 0.02	0.14 ± 0.02	—	—
2003 OP ₃₂	0.53 ± 0.06	0.56 ± 0.08	0.58 ± 0.08	—	—	—
2003 QA ₉₂	0.08 ± 0.01	0.14 ± 0.01	—	—	—	—
2003 QR ₉₁	—	—	—	—	—	—
2003 QW ₉₀	0.06 ± 0.01	0.11 ± 0.02	0.15 ± 0.03	0.20 ± 0.07	0.28 ± 0.14	0.26 ± 0.15
2003 UT ₂₉₂	—	—	—	—	—	—
2003 UY ₁₁₇	0.10 ± 0.00	0.15 ± 0.00	0.19 ± 0.01	0.27 ± 0.04	0.28 ± 0.06	0.29 ± 0.06
2003 UZ ₄₁₃	—	0.08 ± 0.01	0.08 ± 0.01	—	—	—

Table 8 *continued*

Table 8 (*continued*)

Designation	p_B	p_R	p_I	p_J	p_H	p_B
2003 VS ₂	0.12 ± 0.01	0.18 ± 0.01	—	—	—	—
2004 EW ₉₅	0.04 ± 0.00	0.04 ± 0.00	—	0.05 ± 0.03	0.04 ± 0.05	0.04 ± 0.06
2004 GV ₉	0.06 ± 0.01	0.09 ± 0.01	0.12 ± 0.01	0.15 ± 0.05	0.16 ± 0.05	0.17 ± 0.06
2004 NT ₃₃	0.12 ± 0.03	0.13 ± 0.02	0.14 ± 0.03	0.18 ± 0.11	0.17 ± 0.20	0.18 ± 0.25
2004 PF ₁₁₅	—	—	—	—	—	—
2004 PG ₁₁₅	—	—	—	—	—	—
2004 PT ₁₀₇	—	—	—	—	—	—
2004 TY ₃₆₄	0.09 ± 0.04	0.13 ± 0.02	0.15 ± 0.06	0.21 ± 0.07	0.23 ± 0.07	0.24 ± 0.08
2004 UX ₁₀	0.11 ± 0.01	0.17 ± 0.02	—	0.28 ± 0.09	0.30 ± 0.10	0.32 ± 0.10
2004 VT ₇₅	—	—	—	—	—	—
2004 XA ₁₉₂	—	—	—	—	—	—
2005 CA ₇₉	0.07 ± 0.01	0.14 ± 0.01	0.17 ± 0.02	0.28 ± 0.12	0.29 ± 0.15	0.29 ± 0.17
2005 GE ₁₈₇	0.08 ± 0.02	0.16 ± 0.04	0.19 ± 0.06	—	—	—
2005 RM ₄₃	0.12 ± 0.01	0.11 ± 0.01	0.11 ± 0.01	0.13 ± 0.07	0.10 ± 0.11	0.10 ± 0.14
2005 RN ₄₃	0.09 ± 0.01	0.13 ± 0.01	0.16 ± 0.03	0.23 ± 0.03	0.23 ± 0.05	0.24 ± 0.05
2005 RR ₄₃	0.39 ± 0.07	0.46 ± 0.05	0.44 ± 0.08	0.52 ± 0.28	0.41 ± 0.46	0.41 ± 0.56
2005 RS ₄₃	0.09 ± 0.01	0.13 ± 0.01	0.14 ± 0.02	0.20 ± 0.06	0.22 ± 0.06	0.25 ± 0.06
2005 TB ₁₉₀	0.11 ± 0.01	0.18 ± 0.01	0.22 ± 0.02	0.32 ± 0.04	0.32 ± 0.07	0.34 ± 0.07
2005 UQ ₅₁₃	—	—	—	—	—	—
2006 QJ ₁₈₁	0.09 ± 0.02	0.13 ± 0.02	0.15 ± 0.03	0.34 ± 0.14	0.36 ± 0.18	0.34 ± 0.20
2007 JF ₄₃	—	—	—	—	—	—
2007 JH ₄₃	—	—	—	—	—	—
2007 JJ ₄₃	0.08 ± 0.01	0.14 ± 0.01	0.16 ± 0.01	0.24 ± 0.03	0.24 ± 0.05	0.25 ± 0.05
2007 OC ₁₀	0.10 ± 0.00	0.15 ± 0.00	0.17 ± 0.00	0.27 ± 0.04	0.28 ± 0.06	0.29 ± 0.06
2007 XV ₅₀	—	—	—	—	—	—
2008 NW ₄	—	—	—	—	—	—
2008 OG ₁₉	0.09 ± 0.00	0.13 ± 0.00	0.16 ± 0.01	0.28 ± 0.12	0.29 ± 0.15	0.29 ± 0.17
2009 YG ₁₉	0.08 ± 0.01	0.14 ± 0.01	—	—	—	—
2010 ER ₆₅	—	—	—	—	—	—
2010 ET ₆₅	—	—	—	—	—	—
2010 FD ₄₉	—	—	—	—	—	—
2010 JC ₈₀	—	—	—	—	—	—
Borasisi	0.20 ± 0.04	0.33 ± 0.04	0.41 ± 0.07	0.58 ± 0.09	0.67 ± 0.17	0.69 ± 0.14
Chaos	0.04 ± 0.00	0.06 ± 0.01	0.08 ± 0.01	0.11 ± 0.01	0.12 ± 0.01	0.11 ± 0.01
Dziewanna	—	—	—	—	—	—
Eris	0.90 ± 0.12	0.99 ± 0.11	1.03 ± 0.14	0.94 ± 0.04	0.53 ± 0.05	0.35 ± 0.04
G!kunhomdima	—	0.21 ± 0.02	0.24 ± 0.03	—	—	—
Gonggong	0.10 ± 0.03	0.17 ± 0.01	0.23 ± 0.08	0.37 ± 0.05	0.37 ± 0.09	0.35 ± 0.08
Haumea	0.82 ± 0.08	0.79 ± 0.11	0.80 ± 0.07	0.82 ± 0.04	0.58 ± 0.05	0.52 ± 0.06
Huya	0.06 ± 0.01	0.10 ± 0.02	0.13 ± 0.02	0.19 ± 0.01	0.19 ± 0.02	0.20 ± 0.03
Lempo	0.06 ± 0.02	0.11 ± 0.01	0.14 ± 0.04	0.26 ± 0.01	0.27 ± 0.02	0.26 ± 0.01

Table 8 *continued*

Table 8 (*continued*)

Designation	p_B	p_R	p_I	p_J	p_H	p_B
Makemake	0.67 ± 0.08	0.87 ± 0.04	0.86 ± 0.10	0.74 ± 0.15	0.48 ± 0.11	0.35 ± 0.21
Orcus	0.24 ± 0.04	0.24 ± 0.02	0.24 ± 0.06	0.24 ± 0.02	0.20 ± 0.02	0.20 ± 0.02
Quaoar	0.10 ± 0.03	0.17 ± 0.01	0.23 ± 0.07	0.37 ± 0.05	0.36 ± 0.08	0.34 ± 0.08
Salacia	0.04 ± 0.01	0.05 ± 0.00	0.05 ± 0.00	0.05 ± 0.03	0.04 ± 0.05	0.04 ± 0.06
Sedna	0.26 ± 0.07	0.58 ± 0.16	0.78 ± 0.27	1.35 ± 0.19	1.30 ± 0.18	1.28 ± 0.21
Sila-Nunam	0.06 ± 0.01	0.12 ± 0.01	0.15 ± 0.02	0.23 ± 0.02	0.24 ± 0.04	0.24 ± 0.05
Varda	—	0.12 ± 0.03	0.14 ± 0.05	0.22 ± 0.03	0.22 ± 0.05	0.23 ± 0.05
Varuna	0.10 ± 0.03	0.16 ± 0.01	0.21 ± 0.06	0.31 ± 0.01	0.38 ± 0.06	0.35 ± 0.06

Table 9. Colors used in this work for the different diagrams.

Designation	$V - 3.6 \mu\text{m}$	$J - 3.6 \mu\text{m}$	$K - 3.6 \mu\text{m}$	$3.6 \mu\text{m} - 4.5 \mu\text{m}$
	(mag)	(mag)	(mag)	(mag)
1993 SC	< 0.54	< -0.85	< -0.82	< 0.64
1995 SM ₅₅	-1.05 ± 0.42	-1.09 ± 0.26	-0.12 ± 0.26	—
1995 TL ₈	-0.04 ± 0.92	-1.43 ± 0.25	-1.42 ± 0.32	—
1996 GQ ₂₁	0.19 ± 0.41	-1.17 ± 0.22	-1.42 ± 0.28	< -0.71
1996 TK ₆₆	< 2.23	< 1.00	< 0.99	—
1996 TO ₆₆	< -0.61	< -0.58	< -0.79	< 0.93
1996 TP ₆₆	< 0.36	< -0.87	< -0.66	< 0.21
1998 SM ₁₆₅	0.13 ± 0.25	-1.20 ± 0.19	-1.41 ± 0.22	—
1998 SN ₁₆₅	0.67 ± 0.29	0.43 ± 0.19	0.76 ± 1.07	0.20 ± 0.23
1998 VG ₄₄	-0.04 ± 0.71	-0.82 ± 0.55	-0.85 ± 0.55	—
1999 CD ₁₅₈	0.32 ± 0.93	-0.51 ± 0.33	-0.59 ± 0.35	—
1999 DE ₉	0.07 ± 0.25	-0.74 ± 0.17	-0.70 ± 0.18	1.09 ± 0.28
1999 OJ ₄	-0.84 ± 1.87	-2.07 ± 1.79	-2.08 ± 1.82	—
2000 CN ₁₀₅	< 1.11	< 0.45	< 0.24	< -0.43
2000 GN ₁₇₁	-0.09 ± 0.39	-0.90 ± 0.24	-1.05 ± 0.32	0.29 ± 0.33
2000 GP ₁₈₃	0.54 ± 0.66	0.35 ± 0.45	0.63 ± 1.08	—
2000 OK ₆₇	< 1.05	< -0.34	< -0.45	< -0.07
2000 PE ₃₀	0.35 ± 0.66	-0.27 ± 0.25	-0.55 ± 0.28	0.38 ± 0.31
2000 QL ₂₅₁	1.11 ± 0.69	0.45 ± 0.37	0.24 ± 0.35	—
2000 YW ₁₃₄	0.50 ± 0.64	-0.15 ± 0.25	-0.26 ± 0.31	—
2001 CZ ₃₁	0.74 ± 0.65	0.24 ± 0.25	-0.08 ± 0.31	—
2001 QC ₂₉₈	0.49 ± 0.41	-0.17 ± 0.37	-0.38 ± 0.36	—
2001 QF ₂₉₈	0.19 ± 0.51	-0.08 ± 0.47	-0.08 ± 0.55	—
2001 QS ₃₂₂	0.20 ± 4.35	—	—	< 1.51
2001 QT ₃₂₂	< 2.04	—	—	< -0.47
2001 RZ ₁₄₃	0.53 ± 0.68	—	—	—
2001 UR ₁₆₃	0.84 ± 0.32	-0.50 ± 0.16	-0.40 ± 0.46	0.32 ± 0.21

Table 9 *continued*

Table 9 (*continued*)

Designation	$V - 3.6 \mu\text{m}$	$J - 3.6 \mu\text{m}$	$K - 3.6 \mu\text{m}$	$3.6 \mu\text{m} - 4.5 \mu\text{m}$
	(mag)	(mag)	(mag)	(mag)
2001 XD ₂₅₅	0.32 ± 0.66	—	—	—
2001 YH ₁₄₀	0.01 ± 0.52	-0.82 ± 0.23	-0.88 ± 0.26	—
2002 AW ₁₉₇	0.39 ± 0.12	-0.40 ± 0.14	-0.57 ± 0.20	0.18 ± 0.19
2002 CY ₂₂₄	1.42 ± 0.66	0.19 ± 0.38	0.18 ± 0.49	—
2002 GV ₃₁	< 0.29	—	—	< -0.55
2002 KX ₁₄	0.28 ± 0.19	—	—	0.06 ± 0.33
2002 TC ₃₀₂	-0.04 ± 0.34	-1.27 ± 0.34	-1.28 ± 0.46	0.31 ± 0.18
2002 TX ₃₀₀	-1.75 ± 0.48	-1.72 ± 1.07	-1.03 ± 1.25	0.07 ± 0.37
2002 UX ₂₅	-0.01 ± 0.11	-0.80 ± 0.19	-0.81 ± 0.22	0.22 ± 0.18
2002 VE ₉₅	-0.32 ± 0.15	-1.55 ± 0.34	-1.56 ± 0.46	0.57 ± 0.20
2002 VR ₁₂₈	0.58 ± 0.42	—	—	—
2002 VT ₁₃₀	< -0.51	—	—	—
2002 WC ₁₉	0.12 ± 0.28	-1.11 ± 0.35	-1.12 ± 0.46	—
2002 XV ₉₃	0.82 ± 0.41	—	—	—
2003 AZ ₈₄	-0.32 ± 0.20	-0.75 ± 0.21	-0.29 ± 0.30	-0.03 ± 0.17
2003 FE ₁₂₈	0.63 ± 0.90	—	—	—
2003 FY ₁₂₈	0.33 ± 0.17	-0.28 ± 0.18	—	0.25 ± 0.19
2003 OP ₃₂	-1.71 ± 0.44	—	—	< 0.92
2003 QA ₉₂	0.95 ± 1.00	—	—	—
2003 QR ₉₁	1.91 ± 0.52	—	—	—
2003 QW ₉₀	0.13 ± 0.34	-0.82 ± 0.37	-1.11 ± 0.50	—
2003 UT ₂₉₂	0.20 ± 0.81	—	—	—
2003 UY ₁₁₇	0.15 ± 0.28	-0.68 ± 0.19	-0.74 ± 0.22	—
2003 UZ ₄₁₃	0.24 ± 0.27	—	—	—
2003 VS ₂	0.05 ± 0.35	—	—	0.09 ± 0.16
2004 EW ₉₅	0.58 ± 0.41	0.39 ± 0.44	0.67 ± 1.08	—
2004 GV ₉	0.42 ± 0.17	-0.32 ± 0.29	-0.46 ± 0.29	0.40 ± 0.22
2004 NT ₃₃	0.54 ± 0.45	0.12 ± 0.48	0.15 ± 1.09	-0.26 ± 0.21
2004 PF ₁₁₅	-0.04 ± 0.32	—	—	—
2004 PG ₁₁₅	-0.36 ± 0.48	—	—	< -0.72
2004 PT ₁₀₇	1.03 ± 0.31	—	—	—
2004 TY ₃₆₄	0.09 ± 0.21	-0.65 ± 0.29	-0.79 ± 0.29	0.31 ± 0.21
2004 UX ₁₀	0.08 ± 0.29	-0.66 ± 0.30	-0.80 ± 0.30	—
2004 VT ₇₅	-0.21 ± 0.69	—	—	—
2004 XA ₁₉₂	0.16 ± 1.03	—	—	0.39 ± 0.31
2005 CA ₇₉	-0.33 ± 0.66	-1.36 ± 0.38	-1.39 ± 0.49	—
2005 GE ₁₈₇	1.52 ± 0.52	—	—	—
2005 RM ₄₃	-0.07 ± 0.65	-0.26 ± 0.44	0.02 ± 1.07	-0.73 ± 0.27
2005 RN ₄₃	0.21 ± 0.23	-0.62 ± 0.15	-0.68 ± 0.19	0.22 ± 0.14
2005 RR ₄₃	< -1.18	< -1.37	< -1.09	< 0.11

Table 9 *continued*